A Poroelastic Model of Spinal Cord Cavities

The Mechanical Role of Oedema in Syringomyelia

Jenny Venton

School of Computing, Engineering & Mathematics
University of Brighton

A thesis submitted in partial fulfilment of the
requirements of the University of Brighton
for the degree of Doctor of Philosophy

January 2018

University of Brighton

The Leverhulme Trust

Abstract

Syringomyelia is a rare spinal cord condition characterised by the formation of large, fluid-filled cavities in the spinal cord. Despite extensive research, the exact pathophysiology of cavity formation remains elusive and from a clinical perspective syringomyelia remains a complicated condition to treat. The majority of current research agrees that the processes involved are at least partially mechanical, as cerebrospinal fluid (CSF) disturbances are a common factor amongst many of the diseases and injuries that precede syringomyelia. Whilst CSF disturbances have attracted considerable attention in the literature a detailed mechanical examination of the spinal cord is lacking, particularly in relation to syrinx initiation.

To examine processes in the cord prior to syrinx formation a plane strain poroelastic finite element model has been built. Poroelasticity is beneficial in the study of syringomyelia as both extracellular fluid pressures and tissue stresses are calculated. Any mathematical model of a biological system is dependent on the quality of the input parameters and poroelastic parameters for the spinal cord are scarce. A technique for deriving spinal cord porosity and permeability from human diffusion MRI data is presented along with preliminary parameter values.

Anatomical features such as nerve roots, denticulate ligaments and a stiffer grey matter region are included in the model to evaluate how they affect stress and pressure in the cord. Nerve roots and denticulate ligaments are seen to reduce stress in the inner regions of the cord, suggesting that for future models they should not be neglected.

Excess fluid in the spinal cord tissue (oedema) is often associated with the conditions and injuries that precede syringomyelia and oedema has been noted alongside clinical and experimentally induced syringomyelia. A simulated region of oedema has revealed that the presence of oedema increases stress in the spinal cord when it is affected by external CSF pressure. This reinforces the link between syringomyelia and oedema and provides new evidence for its mechanical contribution to syrinx formation.

This thesis presents evidence for a potential mechanism of how a syrinx begins to form in the spinal cord and has provided a modelling foundation. As oedema increases tissue stress the likelihood of tissue damage, and therefore syrinx formation, is increased. In terms of treating syringomyelia this supports the notion that the severity of oedema is a useful indicator of whether a syrinx is likely to form and that treating presyrinx oedema may be a way of preventing cavity formation.

Contents

List of Figures

List of Tables

List of abbreviations

AQP4	aquaporin-4
CC	central canal
CFD	computational fluid dynamics
CM	Chiari malformation
CNS	central nervous system
CSF	cerebrospinal fluid
DMRI	diffusion magnetic resonance imaging
DW-MRI	diffusion weighted magnetic resonance imaging
ECF	extracellular fluid
ECS	extracellular space
FE	finite element
FMD	foramen magnum decompression
FSI	fluid structure interaction
IMPPT	intramedullary pulse pressure theory
NODDI	neurite orientation and dispersion density imaging
NRDL	nerve roots and denticulate ligaments
PDE	partial differential equation
PR	Poisson's ratio
PVS	perivascular space
SAS	subarachnoid space

SCI	spinal cord injury
YM	Young's modulus

Nomenclature

A	DMRI signal decays
a_{gm}	Grey matter fibre radius
a_{wm}	White matter fibre radius
$\boldsymbol{B}$	Strain-displacement matrix
b	b-value
$\boldsymbol{D}$	Elasticity matrix
D	Diffusion coefficient
E	Young's modulus
$\boldsymbol{F}_f$	Pore pressure boundary condition
$\boldsymbol{F}_s$	Solid skeleton boundary condition
$\boldsymbol{f}_s$	Solid skeleton surface force
G	Shear modulus
H	Permeability matrix
K	Stiffness matrix
K_s	Solid bulk modulus
k	Hydraulic conductivity
M	Mass matrix
M_b	Biot modulus
$\boldsymbol{N}$	Shape functions
$\textsc{odi}$	Orientation dispersion index
P	Preconditioner matrix
p	Pore fluid pressure
p_b	Surface pressure
Q	Coupling matrix
$\boldsymbol{q}$	Fluid flux
S	Fluid compressibility matrix

S	Full signal
S_A	Signal attenuation
S_0	Non-diffusion weighted signal
S_{en}	Extracellular signal
S_{iso}	Isotropic signal
S_{in}	Intracellular signal
$\boldsymbol{u}$	Solid displacement

α	Biot-Willis coefficient
β	Skempton coefficient
γ	Surface tension
ε	Strain
κ	Intrinsic permeability
κ_{GM}	Grey matter permeability
κ_{WMpa}	White matter parallel permeability
κ_{WMpe}	White matter perpendicular permeability
$\boldsymbol{\mu}$	Mean orientation vector
μ	Dynamic viscosity
ν	Poisson's ratio
ν_{en}	Volume fraction (extracellular space)
ν_{in}	Volume fraction (tissue fibres)
ν_{iso}	Volume fraction (free CSF)
ρ	Overall density
ρ_f	Fluid density
ρ_s	Solid density
$\boldsymbol{\sigma}$	Effective stress tensor
$\boldsymbol{\sigma}_s$	Solid stress tensor

$\boldsymbol{\sigma}_f$	Fluid stress tensor
ϕ	Porosity
$\phi_{\min}$	Minimum porosity
ζ	Fluid content

Acknowledgements

Firstly I would like to thank my supervisors Dr Paul Harris and Dr Gary Phillips for their insight, advice and encouragement throughout the duration of this thesis.

I thank Dr Francesco Grussu and Professor Claudia Wheeler-Kingshott from the UCL Institute of Neurology and Professor Mara Cercignani at the Clinical Imaging Sciences Centre (CISC), Brighton and Sussex Medical School for permissions to use the data presented in Chapter 4. I would like to extend my thanks to Dr Samira Bouyagoub at CISC for undertaking the NODDI analysis and for her guidance.

I thank Mr Carl Hardwidge at Hurstwood Park Neurosciences Centre for his clinical perspectives of syringomyelia and for providing images in Chapter 1.

I gratefully acknowledge financial support from the Leverhulme Trust, Research Project Grant number RPG-2013-178.

Last, but most certainly not least, I would like to thank: my family for their tireless support and patience, my friends without whom this process would have been much harder and not nearly half as fun, and my partner for his unwavering belief, understanding and for always being there.

`GNU Terry Pratchett`

Declaration

I declare that the research contained in this thesis, unless otherwise formally indicated within the text, is the original work of the author. The thesis has not been previously submitted to this or any other university for a degree, and does not incorporate any material already submitted for a degree.

Signed ....

Dated ....

Chapter 1

Introduction

1.1 Background

1.1.1 Syringomyelia

Syringomyelia is a rare condition characterised by the formation of large, fluid-filled cavities (known as syrinxes) in the spinal cord (see Figure 1.1). Prevalence figures in the general population are between 2–13 per 100 000 (Bogdanov, 2014) although this figure is increased in certain patient populations (Kahn et al., 2015).

A syrinx can form as a result of disease or traumatic spinal cord injury although in some cases the cause is not apparent; it takes months or years to form and can occur at any age although symptomatic cavities normally become apparent around the ages of 28 to 40 (Bogdanov, 2014). Symptoms include pain, loss of sensation and eventual paralysis and although some symptoms may lessen or disappear when the syrinx is treated, damage to the spinal cord is often irreversible.

Figure 1.1: A large syrinx in the cervical spinal cord (Hardwidge, 2014).

Current explanations of syrinx development focus on the mechanical interaction of spinal cord tissue with the cerebrospinal fluid (CSF) that surrounds it. Due to the long time scales involved in syrinx formation it is impractical to monitor a worsening cavity *in vivo*. Furthermore it is unethical to monitor a patient with worsening symptoms rather than providing treatment. As such, mathematical models that simulate the environment in which a syrinx can form and grow have become a popular method for revealing the mechanisms underlying syringomyelia.

1.1.2 Spinal anatomy

The spinal cord is contained within the spinal canal of the vertebral column and is surrounded by CSF, which serves to protect the cord and provides nutrients (Tortora and Derrickson, 2014). The spinal cord connects the brain to the peripheral nervous system via nerve rootlets, which emerge at even intervals along the length of the cord. Together the brain and spinal cord comprise the central nervous system (CNS). A butterfly shaped cross section of grey matter surrounded by white matter runs the length of the spinal cord, the shape of which differs slightly across the cervical, thoracic, lumbar and sacral spinal regions (see Figure 1.2).

1.1.2.1 Grey and white matter

Grey and white matter have different structures. White matter consists largely of bundles of myelinated axons of neurons that run the length of the cord (Figure 1.3(a)) and carry nerve impulses between the brain and the peripheral nervous system (Tortora and Derrickson, 2014). Myelin is a tough sheath that forms around axons and plays a dual role of insulating the axon and increasing the speed of nerve impulses. Grey matter is composed of neuron cell bodies, unmyelinated axons, dendrites and glial cells (Tortora and Derrickson, 2014) and has a more disordered structure than white matter (Figure 1.3(b)). Cells in both grey and

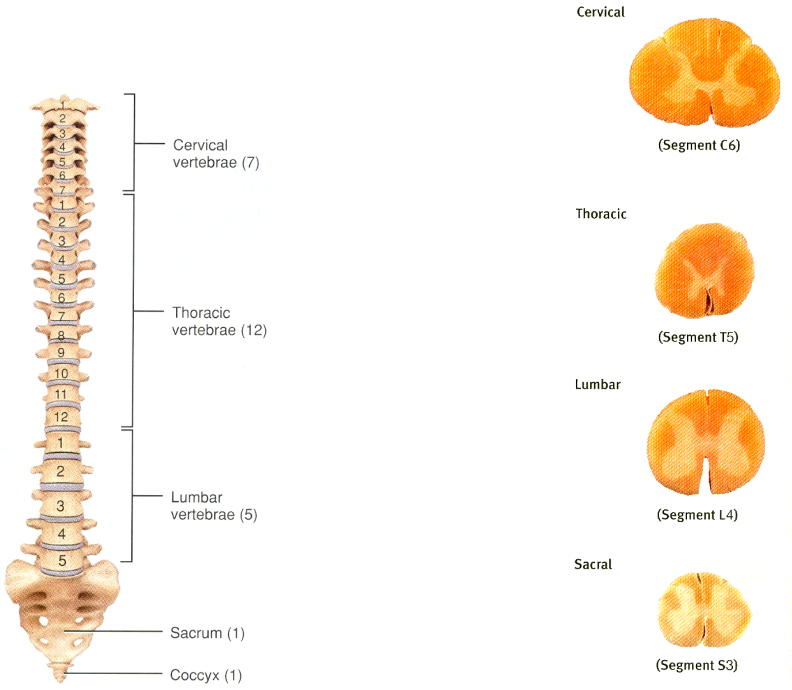

(a) (b)

Figure 1.2: Location of spinal cord regions and the corresponding shapes of grey and white matter in the cord cross section (Tortora and Derrickson, 2014).

white matter are surrounded by extracellular fluid (ECF), a fluid that is likely to be similar in composition to CSF (Brinker et al., 2014). Due to their differing structures, ECF movement differs slightly in grey and white matter (Nicholson and Syková, 1998), for example fluid within white matter preferentially moves parallel to the axons (Syková and Nicholson, 2008).

1.1.2.2 Meningeal layers and subarachnoid space

Three protective layers known as the pia mater, arachnoid mater and dura mater continuously surround the brain and spinal cord (see Figure 1.4). The dura mater is composed of tough connective tissue (Tortora and Derrickson, 2014) and along with the surrounding epidural fat and bone of the spinal canal helps to protect the spinal cord. Closely attached to the dura is a fine layer called the arachnoid mater

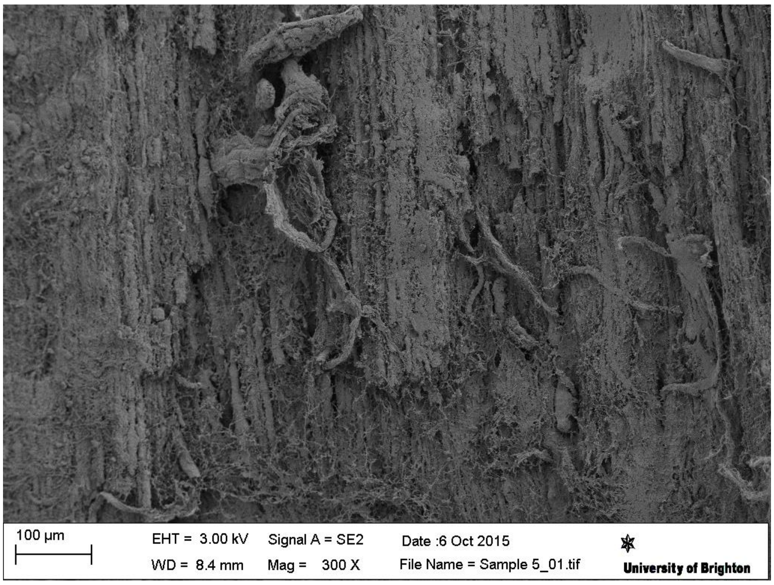

(a) White matter.

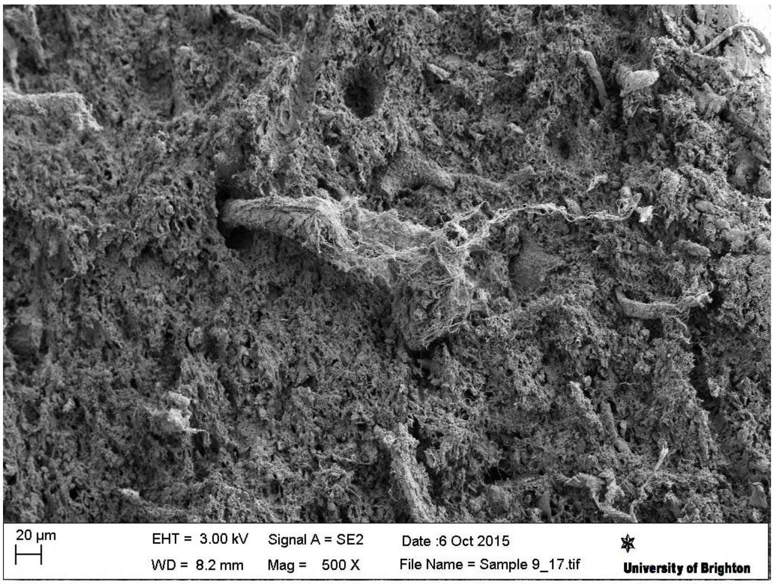

(b) Grey matter.

Figure 1.3: Representative scanning electron micrographs of grey and white matter structures from a sheep spinal cord. 1.3(a) shows the white matter axons that run the length of the cord. 1.3(b) shows grey matter which has a more disordered structure, a blood vessel can be seen in the centre.

from which thin strands known as arachnoid trebeculae (not pictured) spread out, adhering to the pia mater. The pia mater is a thin membrane adhered to the surfaces of the brain and spinal cord and encloses many of the blood vessels supplying them (Tortora and Derrickson, 2014). The pia mater is stiffer than spinal cord grey and white matter and its contribution to the mechanical strength of the cord has been noted (Ozawa et al., 2004; Tunturi, 1978). Together, the pia and arachnoid maters provide the boundaries of the CSF filled region surrounding the cord, known as the subarachnoid space (SAS).

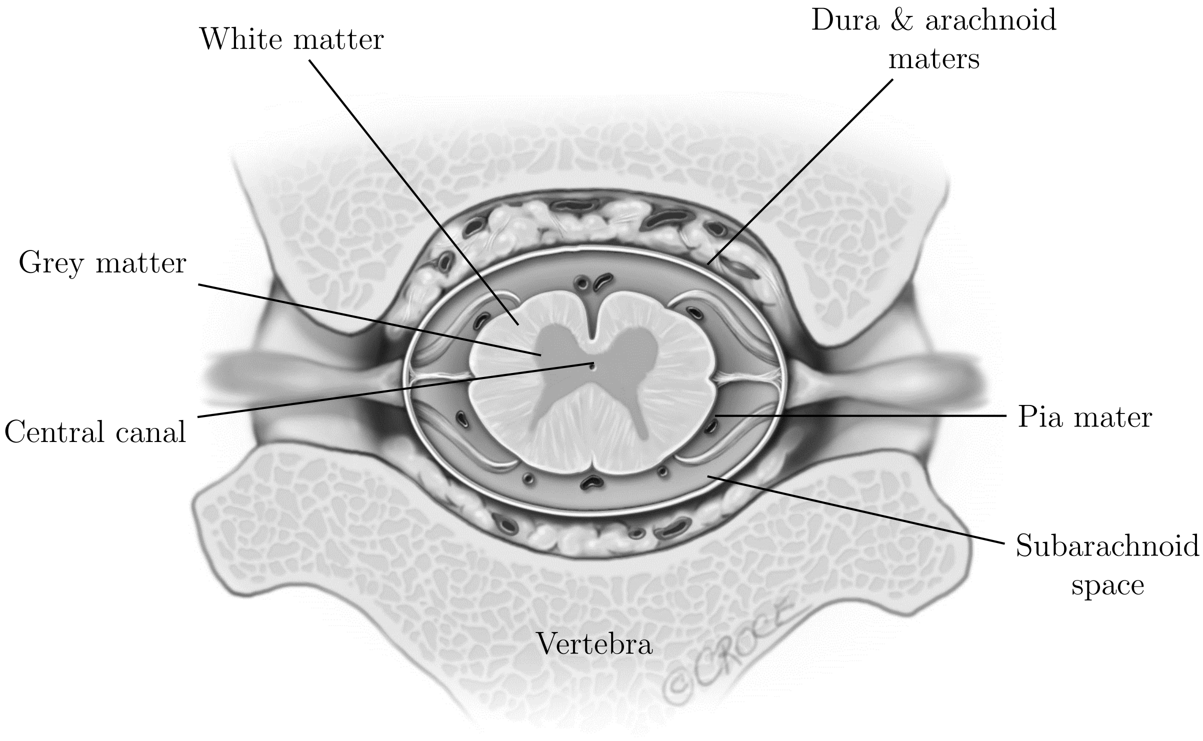

Figure 1.4: A cross section through the spine showing the anatomical features potentially involved in syrinx formation (©2017 Beth Croce) (Elliott et al., 2013). *Image reproduced with permission of the Journal of Fluids and Structures.*

1.1.2.3 Nerve rootlets and denticulate ligaments

Denticulate ligaments are fine, fin-like extensions of the pia mater that fuse with the arachnoid mater along the length of the cord (Figure 1.5). They tether the cord in approximately the centre of the spinal canal and are thought to apply slight tension to it (Tunturi, 1978). Denticulate ligaments cross the subarachnoid space along with nerve rootlets, which connect the central and peripheral nervous systems. A more detailed view of the location of nerve rootlets and denticulate ligaments (NRDL) with respect to the spinal cord and SAS can be see in Figure 1.5. As NRDL cross the SAS they will affect CSF flow, although computational studies have shown this effect to be minimal (Pahlavian et al., 2014).

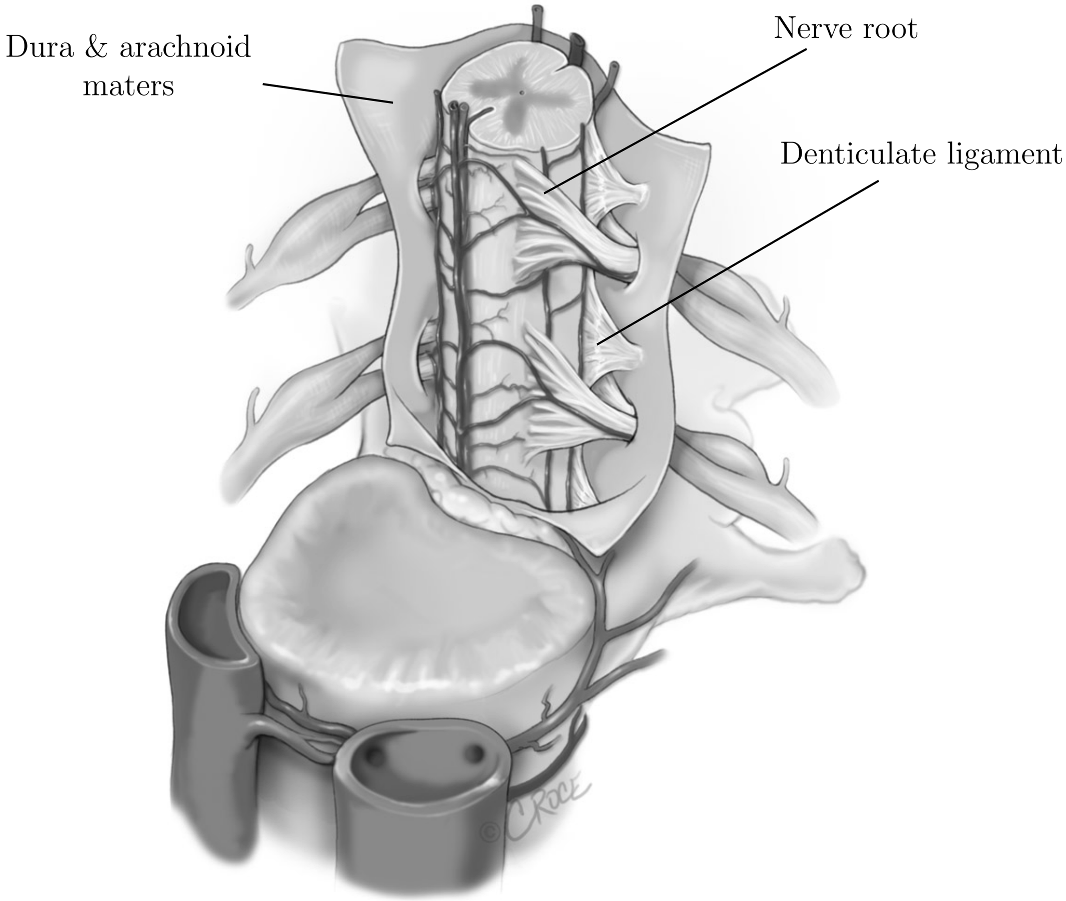

Figure 1.5: A view of the spinal cord with the dura mater opened, showing the location of the NRDL as they cross the SAS between the pia mater and dura mater (©2017 Beth Croce) (Elliott et al., 2013). *Image reproduced with permission of the Journal of Fluids and Structures.*

1.1.2.4 Cerebrospinal and extracellular fluid

Cerebrospinal fluid (CSF) fills the SAS and acts as a shock absorber for the central nervous system (CNS) alongside other roles such as homeostasis of the CNS (Sakka et al., 2011). It is a clear fluid consisting mainly of water but contains small amounts of oxygen, glucose, proteins and cells (Tortora and Derrickson, 2014). Traditionally the bulk of CSF is thought to be produced in the ventricles of the brain then circulates around the brain and spinal cord due to posture, pulse and respiration (Dreha-Kulaczewski et al., 2015; Sakka et al., 2011). Absorption and formation rates are similar and as a consequence CSF volume in a healthy person is generally constant (Tortora and Derrickson, 2014). The extracellular spaces (ECSs) surrounding cells in both grey and white matter are filled with ECF. More recently CSF circulation is thought to be more complicated, with movement across the blood-brain barrier and between CSF and ECF spaces (Brinker et al., 2014). Consequently ECF and CSF are likely to be similar in composition.

1.1.2.5 Central canal

The central canal (see Figure 1.4) runs the length of the spinal cord and is thought to originate from when the neural tube closes during embryonic development (Catala, 1998). A fully open central canal connects to the fourth ventricle of the brain and is rare in adults (Milhorat et al., 1994), although remnant segments of open central canal have been observed (Petit-Lacour et al., 2000).

1.1.2.6 Perivascular spaces

Blood vessels supplying the spinal cord are sheathed by extensions of the pia mater known as perivascular spaces (PVSs) (Figure 1.6). These are sometimes referred to as Virchow-Robin spaces. CSF-like fluid surrounds the blood vessels in the PVS and they have been observed and modelled as a fluid pathway between the SAS and spinal cord ECS (Bilston et al., 2003; Brinker et al., 2014; Wang and Olbricht, 2011). The shape, size and layout of cerebral PVS have been examined and although studies of brain PVS are more common than spinal cord PVS, they are thought to be largely similar (Melissano et al., 2015; Zhang et al., 1990).

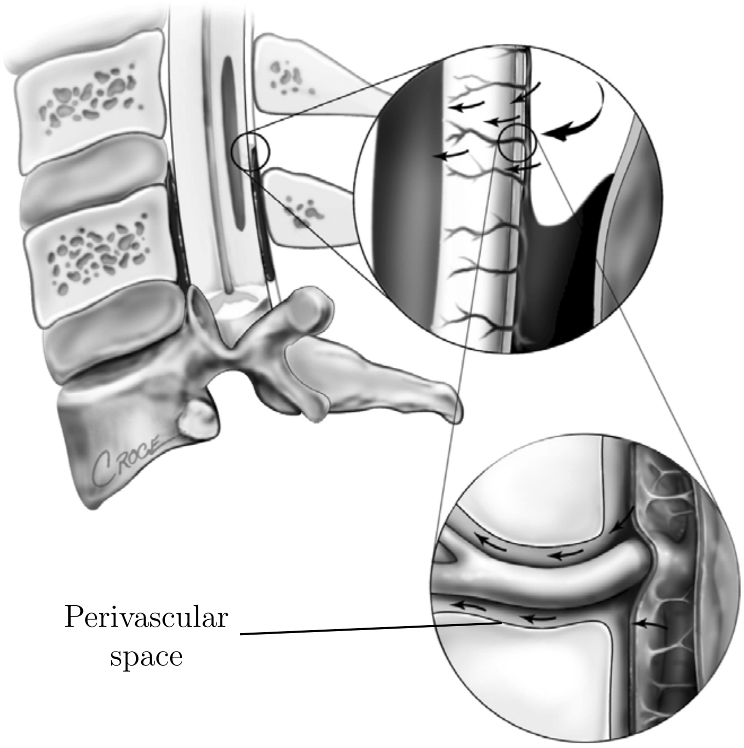

Figure 1.6: PVS surrounding arteries and veins in the spinal cord (©2017 Beth Croce) (Bilston et al., 2010). *Image reproduced with permission of The Journal of Neurosurgery.*

1.1.3 Causes of syringomyelia

Numerous circumstances such as congenital conditions, spinal cord disease and traumatic spinal cord injury (SCI) can be a precursor to syringomyelia cavity formation. One common factor is an obstruction of the SAS that results in a disturbance of the CSF flow surrounding the cord (Elliott et al., 2013; Flint and Rusbridge, 2014; Greitz, 2006; Heiss et al., 2012). In healthy conditions the cord is free to move under CSF movements and physical movements (Cai et al., 2007; Figley and Stroman, 2007). However, in pathological states the cord can be subjected to exaggerated CSF movements and pressures (Cheng et al., 2012; Clarke et al., 2013). Pressure exerted by disturbed CSF is thought to be at least partially responsible for syrinx development and CSF flow and pressure have been seen to return to normal after treatment (Enzmann et al., 1987).

CSF flow disruption is caused by obstructions in the SAS due to Chiari malformation, injury or arachnoiditis each of which is described below. First the different categories of syrinx are described. Then the most common conditions preceding syringomyelia, and how they obstruct CSF flow, are explained in more detail.

1.1.3.1 Classification of syringomyelia cavities

Different types of syrinx can form in spinal cord tissue and syringomyelia is sometimes used as a general term to describe other cavities that can form. Syringomyelia reviews have narrowed the classification of syringomyelia cavities (Klekamp, 2002). For clarity, the syrinxes addressed in this project have the following characteristics:

- Are a dilation of a segment of the central canal (canalicular), a cavity within the cord tissue outside the central canal (extracanalicular) or a combination of the two.

- Contain fluid that is similar or identical to CSF or ECF.
- Do not directly connect to the SAS fluid, which is much rarer.
- Do not directly connect to the brain ventricles via an open central canal (also known as hydromyelia or communicating syringomyelia).
- Is not myelomalacia (softening of the spinal cord tissue sometimes referred to as syringomyelia).

Canalicular syrinxes are most commonly found alongside conditions such as Chiari I malformation whereas extracanalicular syrinxes are most commonly found as a consequence of traumatic SCI (Brodbelt and Stoodley, 2003; Wong et al., 2012). Historically, cavities that had no direct connection to the brain ventricles were attributed to tumour, ischemia or haemotoma (Williams, 1980) but current research treats these cavities in the spinal cord separately to syringomyelia syrinxes.

1.1.3.2 Chiari malformation

The Chiari I malformation (hereafter Chiari malformation (CM)) is the most common precursor to symptomatic syringomyelia (Bogdanov, 2014), with approximately 65–80 % of CM patients going on to develop syringomyelia (Speer et al., 2003). Chiari malformation is diagnosed when at least 5 mm of the lower brain tonsils protrude through the opening in the base of the skull (foramen magnum), as in Figure 1.7. The protruding brain tonsils restrict the opening through which CSF can circulate between the SASs of the brain and spinal cord. This results in an exaggerated pressure difference between brain and spinal cord SAS fluid, an effect thought to be worsened by exertion, increased heart rate and coughing (Linge et al., 2013).

Disturbed CSF flow as a result of CM has been studied *in vivo* (Pinna et al., 2000;

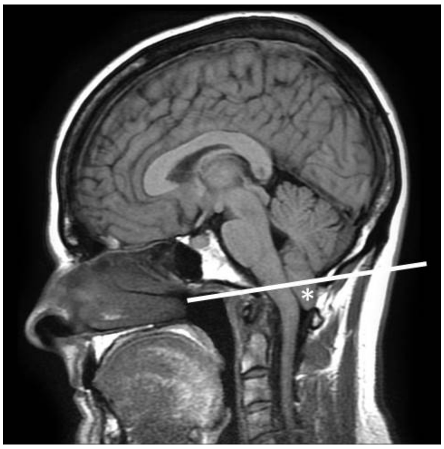

Figure 1.7: An MRI of the brain showing the brain tonsils (white *) protruding out of the skull through the foramen magnum (white line) (Gaillard, 2008).

Williams, 1976) and with computational models (Clarke et al., 2013; Støverud et al., 2016b). Frequently the CSF pressure has been shown to increase alongside CM and a stronger pressure dissociation between the brain and spinal cord SAS has been observed (Williams, 1976). Observed pressure imbalances and increases due to CM have contributed to the development of mechanical hypotheses for syringomyelia in association with CM (Williams, 1980).

Syringomyelia cavities associated with CM are most often found in the cervical spinal cord region, presumably where the pressure disturbances are more prominent. However, newer evidence shows that the severity of CM tonsil protrusion does not always correlate with syringomyelia cavity development (Koyanagi and Houkin, 2010) and that other factors such as insufficient space in the lower skull (posterior fossa) or the shape of the cervical spinal canal (Thompson, 2016; Zhu et al., 2014) can play an important role. This may explain the lack of pressure dissociation observed in some patients with CM and syringomyelia. That, however, would imply an alternate theory to pressure dissociation is responsible for causing syringomyelia in these cases.

Yan et al. (2016) carried out a large (~100 subjects) study looking at differences between CM patients with and without syringomyelia. They found a steeper clivus angle (part of the lower skull) increased the likelihood of a syrinx forming. This finding supports mechanical hypotheses of syrinx formation, as the steeper clivus angle forced fluid around a sharper angle between the brain and spinal cord, increasing CSF flow disturbance.

1.1.3.3 Traumatic spinal cord injury

Syrinx formation is one complication of traumatic SCI, sometimes occurring decades after the original injury. It is thought that ~25 % of SCI patients will go on to develop syringomyelia, where ~10 % are symptomatic (Brodbelt and Stoodley, 2003).

SCI often results in arachnoiditis which is the inflammation and eventual scarring of the arachnoid mater. This inflammation and scarring reduces the size of the SAS and in some cases the arachnoid mater can adhere to the surface of the cord. The resultant narrowing or blockage of the SAS disrupts the healthy flow of CSF around the cord and contributes to cavity growth (Bilston et al., 2006; Cheng et al., 2012).

1.1.3.4 Arachnoiditis

Whilst arachnoiditis is commonly associated with SCI, it can also be induced by diseases such as meningitis or occasionally results from surgery on the cord itself (Klekamp et al., 1997). For example following treatments for neurological conditions such as Chiari malformation (CM) (Vergani et al., 2011). Interestingly, it has been suggested that arachnoid adhesions occasionally occur in the upper spinal cord alongside CMs (Klekamp et al., 2001) and may, in these cases, contribute to syrinx formation.

1.1.3.5 Idiopathic syringomyelia

Up to 16 % of syringomyelia cases are idiopathic and the underlying cause is not apparent (Elliott et al., 2013). For example, one case study described the seemingly spontaneous development and resolution of a symptomatic syrinx in a patient (Ozisik et al., 2006), highlighting how little is known about the formation, growth and resolution of syrinxes. Small anatomical differences such as the shape of the spinal canal may be the trigger for idiopathic syringomyelia (Struck et al., 2016). Furthermore, previously unidentified trauma or illness could play a role in apparently idiopathic syringomyelia. As idiopathic syringomyelia has not been studied extensively it is difficult to speculate on whether mechanical or biological processes are responsible in these cases, or indeed a combination of the two.

1.1.4 Treatments

The ultimate goal of syringomyelia research is to improve outcomes for patients. New and improved understanding of the pathophysiology of syringomyelia can be used by clinicians to assist in the decision making of how best to treat individual cases. Treatment choices are largely driven by the cause of syringomyelia and at present almost all treatments focus on either correcting the CSF flow disruption or directly draining the cavity via a shunt. Whilst there are a range of treatment options, clinical outcomes can be unpredictable and unsatisfactory (Brodbelt and Stoodley, 2003).

Foramen magnum decompression (FMD) is the most common treatment for syringomyelia and other complications associated with CM (Klekamp, 2014). FMD treats the blockage caused by a CM by removing a small part of the skull, effectively widening the hole at the base of the skull through which CSF can move. This is thought to reduce the extreme pressure dissociation between the brain and spinal cord SAS and consequently reduce the syrinx (Batzdorf, 2014), although it is not effective in all cases (Schuster et al., 2013). In rare cases symptoms have worsened following FMD due to developing oedema and additional fluid gathering in the cord (Nurboja and Choi, 2009), although the reasons for this were unclear.

Syringomyelia following traumatic SCI is more complicated to treat, with patients often requiring more than one surgery. In these cases, both blockage of the SAS and curvature of the spine are thought to contribute to cavity formation (Karam et al., 2014). Treatments for arachnoiditis aim to untether the cord and restore free fluid movement (Brodbelt and Stoodley, 2003) however, due to the nature of scar tissue, invasive treatments can often worsen arachnoiditis (Klekamp et al., 1997).

Shunting drains fluid directly from the syrinx to another part of the body, but is susceptible to failure and blockage (Batzdorf et al., 1998). A shunt treats the cavity but not the underlying cause and as such is used when other methods have failed or if it carries a lower risk than other options, for example arachnoid scarring treatments. Shunting failure rates of up to 50 % have been recorded for syringomyelia following SCI (Brodbelt and Stoodley, 2003). Whether a shunt is used to treat a syrinx caused by SCI or Chiari malformation, several studies have noted that the SAS blockage must be removed for a truly beneficial outcome (Brodbelt and Stoodley, 2003; Klekamp et al., 1997) reinforcing the common hypothesis that disturbed CSF flow is a key factor in syrinx formation.

This outline demonstrates that there is still a high element of unpredictability amongst syringomyelia treatments. Furthermore the lack of a suitable method for determining whether an existing syrinx and symptoms will worsen means it can be difficult to decide whether or not to carry out high risk surgical intervention (Flint, 2014). As such, gaining more insight into how disturbed CSF flow can cause damage to the cord and whether there are any markers of this damage, will be beneficial for clinicians when determining treatment options.

1.2 Mechanisms of syringomyelia development and growth

The sheer volume of syringomyelia theories is a testament to both the wide array of causes and how little is truly understood about the pathophysiology of this condition. Whilst syringomyelia research has traditionally focussed on CSF flow and pressure disturbances, the focus of current research is shifting to behaviour inside the cord. Here an outline is given of the various mechanisms thought to contribute to syrinx formation, ranging from bulk CSF movement to ECF fluid movement within the cord tissue.

1.2.1 CSF disturbances

Early clinical researchers such as Williams (1976, 1980) and Gardner and Angel (1958) developed theories of how disturbed CSF pressure could cause a syringomyelia cavity to grow. Following *in vivo* SAS pressure measurements in CM patients, Williams (1976) hypothesised that either pressure differences between the brain and spinal cord SAS caused fluid to be sucked into the syrinx via the central canal, or fluid in an existing syrinx 'sloshed' up and down to worsen a cavity (Williams, 1980). Gardner and Angel (1958) suggested that the force of fluid being driven down the central canal by pulse waves was enough to worsen an existing cavity.

One computational study has recently shown that as a syrinx grows radially, the damaging effects of vigorous fluid movement are diminished (Elliott et al., 2017). This suggests that the growth of a syrinx reduces stress in the spinal cord caused by disturbed CSF flow. However, there is still debate around whether fluid movement and pressure within the syrinx would be strong enough to worsen the syrinx. Whilst potential damaging effects have been observed in a physical model of the cord (Martin et al., 2010), computational models have shown that syrinx fluid motion is unlikely to worsen a cavity (Bertram, 2009). Furthermore the central canal does not always remain fully open into adulthood (Milhorat et al., 1994), thus the fluid pathway suggested by Williams and Gardner is not often present beyond childhood, yet adults and adolescents may still develop syringomyelia. Despite this the fundamental idea that disturbed CSF flow and pressure provides the mechanical means for syrinx development has persisted and these studies provide the groundwork for the majority of present day mechanical syringomyelia models. For a more complete picture of earlier theories see Elliott et al. (2013).

The CSF disturbances studied by Williams and Gardner were the consequence of an SAS blockage. This blockage was caused by CM, just one of the categories of SAS blockage that can precede syringomyelia. Higher pressures in the SAS have been measured above regions of arachnoiditis in models of syringomyelia (Bilston et al., 2006) and there is clinical evidence that cavities also tend to form above arachnoid scarring (Klekamp et al., 1997), strengthening the link between SAS blockages, pressure and cavity formation.

Another explanation of how CSF disturbance could damage the cord is given by the intramedullary pulse pressure theory (IMPPT) (Greitz, 2006) which describes how decreased pressure near an SAS blockage might contribute to syrinx formation. When fluid moving through an enclosed space (such as the SAS) encounters a narrowing, the pressure drops. This effect is known as the Venturi effect (Figure 1.8). With the IMPPT, Greitz (2006) hypothesized that this pressure drop occurs near a blockage with each heartbeat causing the cord to distend and eventually become damaged.

Figure 1.8: Fast moving CSF flow (black arrows) creates a Venturi effect near an obstruction, causing a pressure drop and cord distension (Greitz, 2006). *Image reproduced with permission of Neurosurgical Review.*

Although the intramedullary pulse pressure theory (IMPPT) is convenient in describing cavity formation alongside a wide array of conditions and injuries (Greitz, 2006), whether any Venturi effect produced in the SAS would be strong enough to damage the cord is uncertain. A physical model of the cord and SAS found that no significant Venturi effect occurred (Martin and Loth, 2009). However, the solid material used to represent the cord was not porous and was significantly stiffer than spinal cord tissue so this can not wholly rule out the IMPPT. It has since been suggested that the invisicid inertial fluid model used in the IMPPT does not wholly represent conditions *in vivo* and as such predictions may be unreliable (Støverud et al., 2013). Including inertial effects and modelling the fluid as viscous would be more appropriate.

Due to the complexities of *in vivo* SAS fluid pressure measurement the IMPPT cannot, at present, be directly proven. However, *in vivo* MRI has revealed that the spinal cord moves with heartbeat in healthy conditions (Figley and Stroman, 2007). In diseased conditions with abnormal CSF flow, these repeated exaggerated movements could have a potentially detrimental effect on the tissue.

The fluid compartments in the CNS (CSF, ECF and blood) are understood to remain in dynamic equilibrium with one another, an effect known as the Monro-Kellie hypothesis (Mokri, 2001). Imbalances in this relationship have been attributed to fluid gathering in the cord (Levine, 2004; Nurboja and Choi, 2009). Altered blood flow has been found in association with arachnoiditis and cord tethering (Klekamp et al., 2001), supporting the potential role of cardiac pulse in cavity formation.

A further contributing mechanical factor is the slight tension applied to the cord by NRDL (Tunturi, 1978). This normal tension applied to the cord could cause an existing syrinx or remnant section of central canal to grow, when the cord is subjected to exaggerated CSF pulsation, increased flow velocity and altered pressure.

1.2.2 Syrinx anatomy

The reason why one large syrinx forms rather than several smaller ones is still uncertain. Anecdotally syrinx fluid has been observed to spurt when opened during surgery, suggesting that fluid pressure within a syrinx is higher than at least atmospheric pressure. An interesting inference from this is that there must be some fluid trapping mechanism, at least in the short term, that prevents fluid draining from the syrinx back into the cord tissue.

When induced by arachnoiditis, syringomyelia is often found above the SAS blockage (Klekamp et al., 1997). Higher SAS pressures have also been calculated above an arachnoid SAS blockage (Bilston et al., 2006) which seems contradictory as higher pressure in the SAS would also close any existing cavity. A PVS pumping mechanism was proposed by Bilston et al. (2003), where the PVS could continue to 'feed' a syrinx against a pressure gradient. Alternatively, if a syrinx has any fluid trapping effects, raised SAS pressure would not be able to squeeze fluid from the cavity via a clear pathway and could instead tear the cord tissue.

Potential fluid trapping mechanisms are the lining of ependymal cells found lining the central canal (Milhorat et al., 1994) or simply that the surrounding spinal cord tissue has a very low permeability and does not permit fast bulk flow of fluid. Theories such as the IMPPT (Greitz, 2006) also require a fluid trapping mechanism for the fluid accumulated by cord distension.

1.2.3 Oedema and extracellular fluid behaviour

Syrinx fluid is similar in composition to CSF, although whether it originates in the SAS or the cord itself is uncertain. Regardless of the origins of syrinx fluid, it almost certainly has some interaction with fluid in the ECS and PVS. As such, it is important to understand how fluid behaves within the spinal cord tissue to understand syrinx development.

One demonstrated fluid pathway between the SAS and spinal cord are the perivascular spaces (PVS) (Stoodley et al., 2000) (see Figure 1.9). PVS have been implicated in syringomyelia development (Bilston et al., 2003; Elliott et al., 2011; Kumari et al., 1998), with enlarged PVS being found near a syrinx (Chakrabortty et al., 1994) and enhanced PVS fluid flow near a syrinx being observed (Wong et al., 2012).

In healthy conditions, fluid moves along the PVS yet it is unclear how disturbed CSF could cause this natural fluid movement to contribute to syrinx formation (Brodbelt and Stoodley, 2003), although a perivascular pumping mechanism has been proposed (Bilston et al., 2003). This idea states that when pulsations in the fluid surrounding a blood vessel in a PVS become out of synch with pulsations of the blood vessel itself, this can cause fluid to be 'pumped' into the cord. This

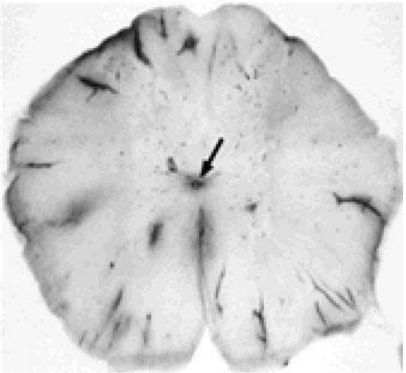

Figure 1.9: Rat spinal cord ten minutes after dye injection into the SAS. Dye has entered the PVS around the edges, the central canal (arrow) and has dispersed within the tissue (Stoodley et al., 2000). *Image reproduced with permission of Neurosurgical Focus.*

could explain how fluid can enter a syrinx seemingly against a pressure gradient.

Enlarged PVS have been observed following arachnoiditis (Klekamp et al., 2001) and a combination of disturbed CSF and enlarged PVS could contribute to cavity formation, an idea which has been supported with computational models (Elliott, 2012). The role that PVS play in the spinal cord are relevant to syringomyelia modelling, however it remains uncertain how increased fluid transport via the PVS contributes to damage and cavity formation within the cord.

Tissue oedema and increased fluid volume in the spinal cord have been observed near a syringomyelia cavity (Chakrabortty et al., 1994; Klekamp et al., 2001) and in concurrence with SAS blockages (Jinkins et al., 1998). These regions of tissue oedema with increased fluid content have been termed the presyrinx state (Fischbein et al., 2000). There are several types of tissue oedema that can occur in the spinal cord, but the most common type preceding syringomyelia is extracellular oedema where the extracellular space surrounding cells becomes distended (Weller, 2014). Fluid within the spinal cord has also been reported as a complication following FMD treatment for CM (Nurboja and Choi, 2009; Vergani et al., 2011), possibly as a result of continued SAS obstruction. Oedema has also been noted as an inflammatory response following traumatic SCI (Brodbelt and Stoodley, 2003).

Clinical evidence of presyrinx oedema has been reported (Wehner et al., 2005). Earlier clinical studies such as Enzmann et al. (1987) have noted areas of high signal intensity in diseased spinal cord; with current knowledge these findings may have been a presyrinx state. Establishing the biological cause of oedema following diseases or conditions that precede syringomyelia is outside the scope of this study. However, determining the extent to which existing oedema could increase the likelihood of cavity formation would improve knowledge of how syringomyelia cavities form and grow.

Whether smaller regions of fluid coalesce to form a cavity or excess oedema fluid moves through the tissue towards a syrinx, a model that examines ECS fluid movement and oedema would enhance understanding of how oedema contributes to cavity formation. For example, once there is an excess of fluid in the cord it would be beneficial to know how this affects the cord tissue in terms of mechanical stress and pressure. To do this, an understanding of how fluid moves through the tissue needs to be obtained. ECS fluid movement has been observed *in vivo* (Sarntinoranont et al., 2006; Stoodley et al., 1996) and is thought to be affected by pulse, disease and physical movement (Klekamp, 2002) although there is little quantitative data regarding this.

Non-mechanical contributors to syringomyelia have recently begun to be explored. The water transport protein aquaporin-4 (AQP4) has been found alongside experimentally induced syringomyelia (Hemley et al., 2012, 2013) and supports the contribution of non-mechanical processes of cavity formation. At present it is uncertain whether the presence of AQP4 is a cause or consequence of syringomyelia.

Although the role of AQP4 is still being explored, this biochemical factor could explain how fluid gathers when the cord is subjected to repeated distension (IMPPT) or high SAS pressures. Oedema and increased AQP4 levels have been found following SCI (Nesic et al., 2006), which could partly explain why fluid appears to accumulate in the cord faster than pressure gradients would suggest. Although mechanical stress in the spinal cord due to disturbed CSF flow is significantly lower than stresses induced by traumatic SCI, the effects on AQP4 production may be similar in producing regions of increased fluid content.

Regardless of where syrinx fluid originates, fluid in the surrounding ECS will affect it whether as a fluid source or as a source of mechanical stress. The role of ECF is becoming an important topic in syringomyelia research (Bertram and Heil, 2017; Drøsdal, 2011; Harris and Hardwidge, 2010; Heil and Bertram, 2016; Støverud et al., 2011, 2016a). However, building a model of the spinal cord and ECF is complicated by the lack of information regarding ECF movement in the spinal cord. A model that includes ECF fluid transport within the cord would deepen understanding of syringomyelia pathophysiology and allow theories such as the presyrinx state to be evaluated in more detail.

1.3 Models of syringomyelia

Besides *in vivo* models, syringomyelia has been modelled using a variety of different methods. These range from physical models using materials with similar properties to biological tissues, computational models of the whole spinal cord and SAS fluid system, to more detailed models of fluid in the perivascular spaces. Here the various syringomyelia modelling techniques are outlined, highlighting the need for more detailed models of the spinal cord tissue and extracellular fluid when examining hypotheses of syrinx formation.

1.3.1 Cerebrospinal fluid models

The link between disturbed CSF flow and syringomyelia is well established (Flint and Rusbridge, 2014), yet the exact mechanisms involved are still unknown. Several computational fluid dynamics (CFD) models of fluid in the SAS have examined how CSF pressure and velocity are affected by injury, arachnoiditis and CM. More recently fluid structure interaction (FSI) models have combined CFD with spinal cord tissue models to reveal how disturbed CSF might affect the cord. Drøsdal et al. (2013) created a two dimensional model of the spinal cord and surrounding fluid, albeit with spatially fixed boundaries, which demonstrated that the presence of a modelled central canal does not alter CSF movement but does increase radial pressure gradients within the spinal cord.

Clarke et al. (2013) found that CM produces higher SAS pressure in a computational fluid dynamics (CFD) model. Interestingly when a syrinx was introduced to the CM model, pressures in the SAS were similar to a healthy SAS model, a result which has been noted in other studies (Elliott et al., 2011; Støverud et al., 2016b). This syrinx related SAS pressure reduction further supports the link between syringomyelia and CSF disturbance. Furthermore, it suggests that in the presence of abnormal CSF movement, the spinal cord tissue cannot withstand the stresses it is subjected to and a syrinx may form as a kind of equaliser for disturbed SAS pressure.

CFD models have calculated increased pressure gradients above and below a partial obstruction of the SAS (Bertram, 2010; Støverud et al., 2013) and increased pressures have been calculated above complete (albeit permeable) blockages of the SAS due to arachnoiditis (Bilston et al., 2006). Tonsillar herniation due to CM blocks the SAS between the brain and spinal cord and CFD models around a Chiari blockage have demonstrated increased pressure gradients (Linge et al., 2013).

Although CFD models provide useful insight into CSF dynamics and wave propagation (Elliott et al., 2014), an investigation of internal tissue behaviour is required to understand the mechanisms underlying syrinx formation. The spinal cord and surrounding CSF interact dynamically, therefore a cord only model without a CFD model of the surrounding SAS fluid may reduce accuracy of the results. This effect has been investigated computationally and is thought to be minimal, although it should be noted that this study modelled the cord as a very stiff material (~700 kPa as opposed to ~5 kPa for cord tissue) which may have affected this result (Cheng et al., 2014).

1.3.2 Physical models

Physical models of the spinal cord and subarachnoid space are comparatively rare (Martin and Loth, 2009; Martin et al., 2010). They allow pressure measurements within the cord and SAS to be taken whilst inherently obeying natural laws that would be otherwise simplified or neglected in computational models. The main challenge is finding materials that appropriately represent biological tissues, however physical models provide useful data to compare with computational and *in vivo* models.

Martin and Loth (2009) measured pressure in and around the spinal cord following a simulated cough (Figure 1.10). Results showed that the presence of a syrinx and an SAS blockage increased pressure gradients in the SAS, seemingly contradicting findings from CFD studies that showed reduced pressure gradients in the presence of a syrinx. However, this could have been a result of the elastic polymer material used to represent the cord, as it was much stiffer than spinal cord tissue is thought to be (~500 kPa as opposed to ~5 kPa). Following the simulated cough pulse it was found that pressure in the SAS was alleviated by the presence of a syrinx.

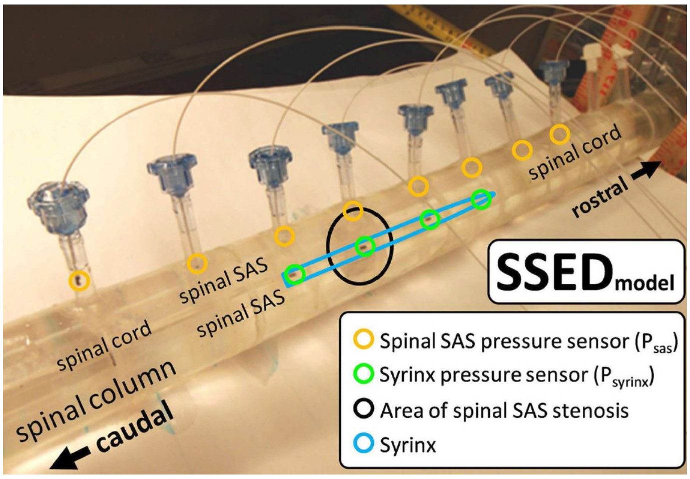

Figure 1.10: Physical model representing the spinal cord with a syrinx, inside a flexible spinal column containing a partial (~90%) blockage (referred to in the image as stenosis). Pressure is measured via the catheters along the top (Martin and Loth, 2009).

1.3.3 Lumped parameter models

Lumped parameter models have been used to examine how various fluid compartments such as the SAS, central canal, brain ventricles and fluid cisterns in the skull interact with the brain (Linninger et al., 2009) and less frequently the spinal cord. These models provide insight into overall CNS behaviour and can evaluate how this contributes to cavity formation.

Chang and Nakagawa (2003) found that pressure waves propagated along the spinal central canal were increased when the cisterna magna was reduced (Figure 1.11). They hypothesised that a reduced cisterna magna could be responsible for syrinx formation alongside CM, as it explains why syringomyelia does not always correlate with tonsillar herniation and why FMD can resolve CM symptoms. However this hypothesis is dependent on an open central canal which does not always occur in adults (Milhorat et al., 1994).

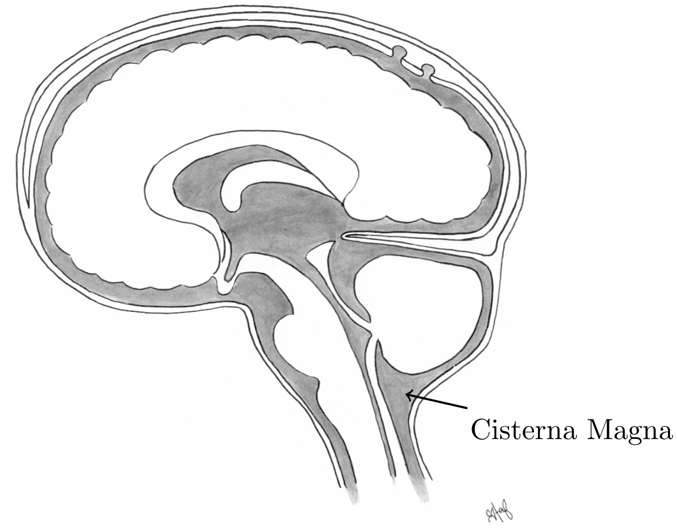

Figure 1.11: Location of CSF pathways in the brain and spinal cord (©2018 Stephen Carder).

Another lumped parameter model by Elliott et al. (2011) included the PVS as a means for fluid to enter the cord. They showed that when PVS and SAS fluid pressures are out of phase there will be an influx of fluid into the cord. Furthermore their model also demonstrated that pressure across the cord was reduced in the presence of a syrinx, again suggesting that syrinx growth helps to alleviate abnormal pressure in the SAS.

1.3.4 Cord stress models

The previous Sections have described models that have concentrated either on CSF movement or on the mechanical behaviour of the CNS as a whole. Another set of models focusses on stresses and pressures within the spinal cord tissue itself when the cord is subjected to CSF pressures that have been disturbed by injuries and conditions that commonly precede syringomyelia. These are computational models using finite element or other numerical methods to calculate stress in the cord. The cord is often modelled as a linear or viscoelastic material, although poroelastic models that include the ECF component of tissue have been explored.

Bertram et al. (2008) modelled the cord as a viscoelastic material subjected to loading and revealed that tensile radial stresses were insufficient to damage the tissue. However, when the cord is subjected to repeated small stresses as a result of breathing, pulse or movement combined with SAS blockage, this could have a cumulative effect. The relevance of ECF movement to the pathogenesis of syringomyelia was outlined in Section 1.2.3 and a model that captures the mechanical behaviour of spinal cord tissue alongside ECF movement would give insight into this potential syringomyelia factor.

Poroelasticity has long been used to represent many biological tissues such as bone, heart, cartilage, brain and spinal cord (Turan and Arbenz, 2014; Chapelle et al., 2010; Korhonen et al., 2003; Eisenträger, 2012; Vardakis et al., 2016; Bertram and Heil, 2015; Harris and Hardwidge, 2010; Sarntinoranont et al., 2003; Støverud et al., 2016a) as it captures behaviour of both the solid and fluid parts of these tissues. It is thought to provide a reasonable representation of biological material behaviour (Moeendarbary et al., 2013). CFD models have included a poroelastic spinal cord to evaluate how this affects CSF flow (Støverud et al., 2011) however, only a few models have used a poroelastic model to determine whether internal tissue stress could be high enough to damage the cord.

An axisymmetric poroelastic model of the spinal cord by Harris and Hardwidge (2010) found higher stresses near an existing cavity, implying that once a cavity is formed it is likely to worsen. Another poroelastic axisymmetric model of the cord and SAS by Bertram and Heil (2017) revealed that a syrinx is more likely to form caudal to (below) an SAS blockage. Bertram and Heil (2017) also proposed the ECS as a potential fluid pathway between the cord tissue and SAS. The role of fluid movement through the ECS can be explored further using poroelastic modelling. Furthermore levels of tissue stress and ECF pressure can be calculated to give insight into how the spinal cord might sustain damage and form a syrinx when subjected to disturbed CSF flow.

Poroelastic models of the brain are more common than spinal cord and have been used to study drug infusion (Chen and Sarntinoranont, 2007; Eisenträger, 2012; Raghavan and Brady, 2011) and diseases such as hydrocephalus. Two hydrocephalus models by Vardakis et al. (2016) and Wirth and Sobey (2006) are noteworthy as they evaluated levels of oedema in the brain based on simulated fluid content. A similar approach would benefit syringomyelia research by providing insight into fluid gathering in the cord and the presyrinx state described in Section 1.2.3.

A comprehensive poroelastic model by Støverud et al. (2016a) determined the effect of various anatomical features on pressure distribution in the cord. Amongst other factors they found that a stiff pia mater caused faster pressure waves in the cord as did a central canal, a result noted in an earlier study (Drøsdal, 2011). Other poroelastic spinal cord models have been used to study drug delivery (Sarntinoranont et al., 2003, 2006) although these are rare, largely due to the lack of accurate data regarding mechanical properties of spinal cord tissue.

1.4 Contributions of the thesis

In light of the current state of syringomyelia research and the existing methods for investigating syrinx formation, there is a need to examine ECF pressure and tissue stress within the cord in relation to cavity formation. An outline of the stages of syringomyelia can be seen in Figure 1.12. Section 1.2.1 described existing research that has examined how SCI and congenital conditions lead to the disturbed CSF pressure thought to cause syringomyelia. Within syringomyelia research the focus has extended to the mechanical behaviour of spinal cord tissue and ECF within the cord (Section 1.2.3). Poroelasticity has been successfully utilised to model the spinal cord in the context of syringomyelia (Section 1.3.4), however a detailed examination of stresses inside the cord that could potentially lead to syrinx formation has not been undertaken. The aim of this work is to provide insight into how ECF pressure changes and spinal cord tissue stresses contribute to the pathophysiology of syringomyelia.

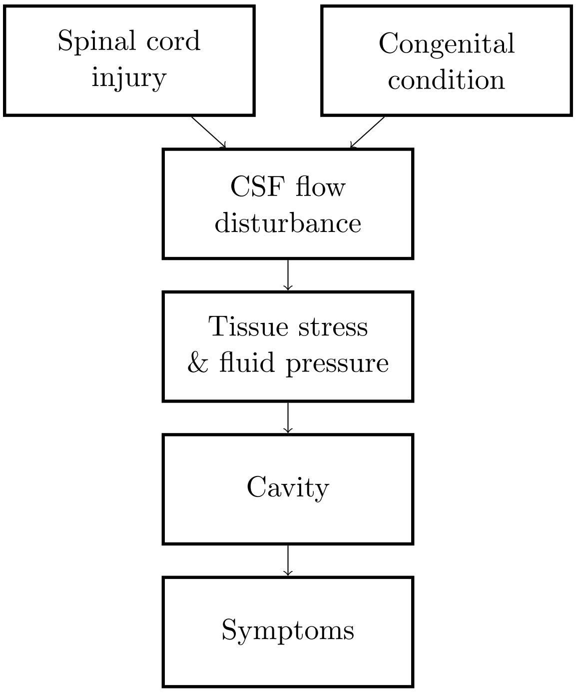

Figure 1.12: Stages of syringomyelia. This thesis focusses on how stress and pressure in the cord tissue could lead to cavity formation.

A two dimensional poroelastic finite element model of the cord cross section has been developed to reveal stresses within the spinal cord. Mechanical stress indicates a potential source of tissue damage and of the few existing poroelastic models of syringomyelia, none have examined stresses across the cord cross section in detail. Unlike some other poroelastic models of the cord, the present model includes inertial effects and fully two-way coupled poroelasticity. As the focus of this thesis is on mechanical behaviour within the spinal cord tissue, the model has not been coupled to a CFD model of the surrounding CSF as in other studies. The effects of excluding FSI are thought to be minimal (Cheng et al., 2014). The function of cord tissue as signal processor or carrier is also excluded as the focus is on the morphology and mechanical interactions of spinal anatomy.

Several theories of syrinx formation have been presented and the relationship between syringomyelia and spinal cord tissue oedema has been explored with *in vivo* models (Klekamp et al., 2001). Despite the fact that oedema has been noted experimentally and clinically alongside syringomyelia (Akiyama et al., 2008; Itoh et al., 2002), there have been no quantitative computational studies to evaluate how regions of oedema could contribute to cavity formation and growth from a mechanical perspective. The present poroelastic model is the first detailed evaluation of stresses in the spinal cord cross section in circumstances associated with syringomyelia such as oedema and increased CSF pressure.

To improve the poroelastic spinal cord model, parameters that describe cord tissue as accurately as possible are required. Whilst work has been undertaken to characterise the elastic properties of CNS tissues such as the spinal cord, little is known regarding suitable porosity and permeability values. A technique for deriving spinal cord porosity and permeability values from diffusion weighted magnetic resonance imaging (DW-MRI) data is presented. Although still in development, the non-invasive nature of the presented technique makes its applicability more widespread. A review of spinal cord elastic properties in the literature has been presented and the poroelastic model has been improved with both these and the experimentally derived tissue properties.

Chapter 2 describes the poroelastic equations used, along with the boundary conditions applied and the finite element solution. Poroelastic parameters such as permeability and porosity are notoriously difficult to measure, particularly in a complex ever-changing biological material. A technique to derive these parameters using DW-MRI data is presented in Chapter 4. A review of existing elastic and poroelastic tissue parameters is given in Chapter 3.

Chapter 5 presents the results of the simulations, where the spinal cord model has been used to calculate stress and pressure in the cord in circumstances preceding syringomyelia cavity formation. The results of including regions of oedema and a disturbed CSF boundary condition are presented along with a sensitivity analysis of various parameters included in the model. Implications of these findings for the understanding of syringomyelia pathophysiology is given in Chapter 6.

Syringomyelia remains a somewhat enigmatic condition and consequently it can be difficult for clinicians to choose the most suitable treatment option for a patient. It is hoped that the present model of cavity formation will give some insight into this process and in the long term assist clinicians making decisions on how best to treat syringomyelia and its associated causes.

Chapter 2

Poroelastic spinal cord model

Introduction

To investigate how SAS pressure changes could cause damage to spinal cord tissue, a plane strain poroelastic model of the radial cord cross section has been built. Pressures that are representative of those induced by disturbed CSF flow have been applied to the poroelastic spinal cord model which is solved using the finite element method. Whilst three dimensional modelling will be beneficial in future versions, a two dimensional model of the cord cross section gives insight into the impact of the cord shape as well as grey matter region shape and incorporates tethering due to nerve roots and denticulate ligaments (NRDL).

A plane strain model represents behaviour of a long cord with uniform cross section and longitudinally uniform loading along its length. Axisymmetric models of the spinal cord exist (Bertram and Heil, 2017; Harris and Hardwidge, 2010; Heil and Bertram, 2016) however the spinal cord is not uniformly cylindrical and furthermore an axisymmetric model does not allow for localised tethering at the cord edge.

Due to the long axon tracts that run the length of the spinal cord, white matter elasticity is more anisotropic than other tissues of the spine (Koser et al., 2015) and permeability properties are thought to be similarly anisotropic (Sarntinoranont et al., 2003). This anisotropy is neglected in a two dimensional model, however neglecting white matter anisotropy is thought to have a minimal effect on pressure waves in the cord (Støverud et al., 2016a). Other tissues of the spine such as grey matter and the pia mater are deemed to be adequately represented as an isotropic material (Bertram and Heil, 2017; Koser et al., 2015). Hence a two dimensional plane strain model of the cord cross section, whilst a simplification, provides an indication of tissue stresses and ECF pressures occurring in the spinal cord prior to syringomyelia cavity formation.

Whilst mathematical models of syringomyelia are becoming more common, the use of poroelasticity to model the cord is rarer (as described in Chapter 1, Section 1.3) and provides a means to characterise tissue stress and ECF pressure when the spinal cord is exposed to disturbed CSF flow. The finite element method is well suited to problems with unusual geometry such as the spinal cord and allows tissue features such as the butterfly shaped grey matter cross section to be included. Inclusion of separate tissue components such as grey matter, white matter and the pia mater is rare; the only apparent model that has included these effects (Støverud et al., 2016a) used a quasi-static poroelastic model unlike the fully dynamic model presented here. Inclusion of inertial effects is necessary to fully capture behaviour of spinal cord tissue being compressed by the surrounding CSF, an effect included in some poroelastic models (Bertram and Heil, 2017; Harris and Hardwidge, 2010; Heil and Bertram, 2016). These models used an axisymmetric geometry that did not represent separate tissue components.

NRDL have not been accounted for in any existing poroelastic syringomyelia model to measure the impact that NRDL tethering has on the distribution of stress and pressure in the cord. Similarly, to the author's best knowledge, no model of syringomyelia has evaluated the impact that a region of oedema has on stress and pressure in the cord. Revealing the mechanical role of presyrinx oedema in syringomyelia cavity formation will provide greater understanding into the pathophysiology of this condition. Sections 2.1 and 2.2 describe the poroelastic material model and finite element solution techniques used in the computational simulations. Boundary conditions and features of spinal anatomy represented in the model are explained in Section 2.3, along with how the external CSF loading is applied.

2.1 Poroelastic tissue model

Chapter 1 described how poroelasticity is seen as an increasingly useful tool for modelling central nervous system tissue, particularly in the context of medical conditions in which tissue mechanics and pressures play a role. Poroelastic models of the brain and spinal cord have been built to evaluate CSF dynamics in the SAS (Støverud et al., 2011), drug delivery (Sarntinoranont et al., 2003), the progression of hydrocephalus (Eisenträger, 2012; Mehrabian and Abousleiman, 2011; Sobey and Wirth, 2006) and syringomyelia (Bertram and Heil, 2017; Harris and Hardwidge, 2010; Heil and Bertram, 2016; Støverud et al., 2016b).

Some preliminary work to determine how appropriate poroelasticity is for modelling CNS tissue has provided mixed results. Spinal cord tissue stress is known to be dependent on the rate of loading (Bilston, 2016) and Miller (2000) suggests that a biphasic[1] finite element (FE) model inadequately represents this behaviour. However, this was based on the assumption that fluid pressure in the spinal cord is zero (Armstrong et al., 1984) which is not the case *in vivo*. Moeendarbary et al. (2013) showed that the mechanical response of individual living cells is well represented by poroelasticity. Although these were not CNS cells, it is beneficial that poroelasticity has been shown to model biological material well. Some of the viscoelastic responses of CNS tissue are due to fluid movement in the ECS (Bilston, 2016), further justifying the use of a model that can represent ECS fluid movement and pressure.

A poroelastic model is particularly appropriate in the context of syringomyelia, as fluid pressure in the ECS can be simulated alongside cord tissue stresses. In a fully coupled poroelastic model, the effects of ECS fluid pressure on tissue stress and vice versa are included. The aims of the present poroelastic model

---

[1] Similar to poroelasticity, see Simon (1992).

are to evaluate which regions of the cord cross section are more susceptible to damage and to evaluate the effect of NRDL tethering and oedema when the cord is subjected to external CSF pressures. This contributes to the understanding of the mechanical aspect of syringomyelia cavity formation.

2.1.1 Definition

A poroelastic material is defined as a solid material containing many small interconnected fluid filled spaces. The solid part of a poroelastic material is known as the solid skeleton and the fluid filled spaces are called pores. In a poroelastic model of the spinal cord, definitions of the solid skeleton and pores in relation to spinal cord tissue anatomy are important. In the present work (as in Venton et al. (2017)), the spinal cord solid skeleton is assumed to consist of large tissue components such as axons, dendrites and cell bodies and the pore fluid region is assumed to consist predominantly of ECF. Poroelastic theory was initially developed by Biot (1941) and the content of Section 2.1 draws extensively from this work and others that have built upon it (Biot, 1956; Coussy, 2004; Detournay and Cheng, 1993).

2.1.2 Solid skeleton

The solid skeleton is assumed to be a linear elastic material, that is the stress (force per unit area) is directly proportional to the strain (amount of deformation) (Bower, 2010). The assumption of small strains

$$\|\nabla \boldsymbol{u}\| \ll 1 \, ,$$

where $\boldsymbol{u}$ is the material displacement vector with regards to an initial reference point, indicates that the linearised strain tensor can be used

$$\boldsymbol{\varepsilon} = \frac{1}{2}(\nabla \boldsymbol{u} + (\nabla \boldsymbol{u})^T) \, . \tag{2.1}$$

Both elastic stress within the solid skeleton $\boldsymbol{\sigma}_s$ and stress within the pore fluid $\boldsymbol{\sigma}_f$ contribute to the effective stress tensor (Coussy, 2004)

$$\boldsymbol{\sigma} = (1 - \phi)\boldsymbol{\sigma}_s + \phi \boldsymbol{\sigma}_f \, .$$

Here the Eulerian porosity ϕ denotes the fraction of the poroelastic material occupied by pore fluid. In the Biot poroelastic model, shear stresses in the fluid are disregarded (Biot, 1941) (fluid viscosity effects are considered in the pore fluid model, Section 2.1.3) and the fluid stress term $\boldsymbol{\sigma}_f$ can be written in terms of pressure p and the identity tensor $\boldsymbol{I}$ resulting in the solid skeleton constitutive equation

$$\boldsymbol{\sigma} = (1 - \phi)\boldsymbol{\sigma}_s - \phi p \boldsymbol{I} \, . \tag{2.2}$$

2.1.3 Pore fluid

Fluid transport through the pores is modelled using Darcy's law (Detournay and Cheng, 1993)

$$\boldsymbol{q} = -\frac{\kappa}{\mu}\nabla p \tag{2.3}$$

where $\boldsymbol{q}$ is the volume of pore fluid moving through a unit area per second, κ is the intrinsic permeability and μ is the dynamic viscosity of the pore fluid. This is assuming isotropic permeability where the permeability tensor can be written $\boldsymbol{\kappa} = \kappa\boldsymbol{I}$. Darcy's law relates fluid flux $\boldsymbol{q}$ through a representative area of material to force, in this case the normal force from fluid pressure. Fluid inertial terms have been disregarded. Darcy's law assumes laminar flow through the pore spaces (Coussy, 2004). It is uncertain whether fluid in the spinal cord ECS is subject to turbulence, so at present the assumption of laminar flow is deemed to be reasonable.

The volume of pore fluid in a representative volume of material varies depending on the pore fluid pressure and the deformation of the poroelastic material. Variation of fluid content ζ in a representative volume of the poroelastic material is given by (Biot, 1941; Detournay and Cheng, 1993)

$$\zeta = \alpha\boldsymbol{\varepsilon}_{ii} + \frac{1}{M_b}p\,. \tag{2.4}$$

where $\boldsymbol{\varepsilon}_{ii}$ is the volumetric strain of the solid skeleton. The Biot-Willis coefficient α and Biot modulus M_b indicate the change in pore fluid volume when the pressure is held constant and when the pore pressure changes respectively. A more detailed description of the physical implications of these parameters is given in Chapter 3.

2.1.4 Governing equations

The equilibrium equation for the solid skeleton (Biot, 1956; Coussy, 2004) is given by

$$-\rho\frac{\partial^2\boldsymbol{u}}{\partial t^2}+\nabla\cdot\boldsymbol{\sigma}+\boldsymbol{f}_s=0\,, \tag{2.5}$$

where $\nabla\cdot$ is the usual divergence operator and $\boldsymbol{f}_s$ is a known surface force. The density ρ has contributions from both the solid skeleton density ρ_s and fluid density ρ_f in the form $\rho=\rho_s(1-\phi)+\rho_f\phi$; the contribution of each is determined by the porosity ϕ. Body force due to gravity has been neglected as it is assumed the spinal cord is initially in equilibrium under its own weight (Cheng, 2016). Substituting the partial stress vector (2.2) into Equation (2.5) gives the full solid equation of motion for a poroelastic material

$$-\big[\rho_s(1-\phi)+\rho_f\phi\big]\frac{\partial^2\boldsymbol{u}}{\partial t^2}+\nabla\cdot\big[(1-\phi)\boldsymbol{\sigma}_s-\phi p\boldsymbol{I}\big]+\boldsymbol{f}_s=0\,. \tag{2.6}$$

Under the assumption of an incompressible pore fluid, the change in variation of fluid content ζ in a unit of the poroelastic material must be equal to the fluid leaving or entering it (Biot, 1941). This yields the fluid continuity equation

$$\frac{\partial\zeta}{\partial t}=-\nabla\cdot\boldsymbol{q}\,. \tag{2.7}$$

Substituting Darcy's law (Equation (2.3)) and Equation (2.4) into (2.7) gives the full fluid continuity equation for a poroelastic material

$$\frac{\partial}{\partial t}(\alpha\boldsymbol{\varepsilon}_{ii}+\frac{1}{M_b}p)=\frac{\kappa}{\mu}\nabla^2 p$$

which can be written (Coussy, 2004)

$$\alpha \frac{\partial \varepsilon_{ii}}{\partial t} + \frac{1}{M_b} \frac{\partial p}{\partial t} = \frac{\kappa}{\mu} \nabla^2 p \,. \tag{2.8}$$

Equations (2.6) and (2.8) are a coupled system of equations that describe the behaviour of the linear poroelastic material used to model the spinal cord. The unknown variables obtained by solving the system are solid skeleton displacement $\boldsymbol{u}$ and fluid pressure p. Certain fluid properties such as density ρ_f and viscosity μ are known constants. Elastic properties of spinal cord tissue such as density ρ_s, Young's modulus E and Poisson's ratio ν (the latter two describe the relationship between the solid skeleton stress and strain) are less well known. There is little information regarding the poroelastic constants of spinal cord tissue, as such these are based on the information available. Poroelastic constants include permeability κ, porosity ϕ, Biot's modulus M_b and the Biot-Willis coefficient α.

2.2 Finite element solution

The poroelastic equations described are used to simulate spinal cord tissue displacements and pressures when the cord is compressed or distended by external CSF pressure. The FE method is one of the standard solution techniques for partial differential equations (PDEs) and is particularly useful for solving equations over irregular shapes such as the spinal cord cross section. The purpose-built finite element program was written in Fortran 95 with the GFortran compiler, using the Code::Blocks IDE, version 1.30.0. External libraries were used for finite element mesh generation and the iterative solver (Geuzaine and Remacle, 2009; HSL (2013)). An outline of the finite element program is shown in Appendix A.

2.2.1 Spatial discretisation

The PDEs are spatially discretised using quadratic (6-node) triangular elements. Linear elements were considered, but the mesh refinement required to obtain the same level of accuracy as quadratic elements meant it was more effective to use quadratic elements. As the focus is on pressure and stress across the spinal cord section, the domain is a simplified cross section of the cervical spinal cord, see Figure 2.1(a). Geometry of the cross section domain is based on a high resolution image of the cervical spinal cord, details are given in Section 2.2.4. A mesh of the spinal cord cross section was generated using Gmsh version 3.0.5 (Geuzaine and Remacle, 2009) (see Figure 2.1(b)).

In a plane strain poroelastic model there are three unknowns at each node in the domain; solid skeleton displacement in the x and y directions and pore fluid pressure. For each 6-node triangular element these displacements and pressures take the form

$$\boldsymbol{u}^e_{1-6} = \begin{bmatrix} u_1 & u_2 & u_3 & u_4 & u_5 & u_6 \\ v_1 & v_2 & v_3 & v_4 & v_5 & v_6 \end{bmatrix}^T$$

and

$$p^e_{1-6} = \begin{bmatrix} p_1 & p_2 & p_3 & p_4 & p_5 & p_6 \end{bmatrix}^T$$

respectively, where superscript e denotes element nodal displacements or pressures and u_{1-6} and v_{1-6} are displacements in the x and y directions respectively. The shape functions for each 6-noded quadratic triangular element of the mesh are represented by the vector (Zienkiewicz and Taylor, 1989)

$$\boldsymbol{N} = \begin{bmatrix} N_1 & N_2 & N_3 & N_4 & N_5 & N_6 \end{bmatrix}$$

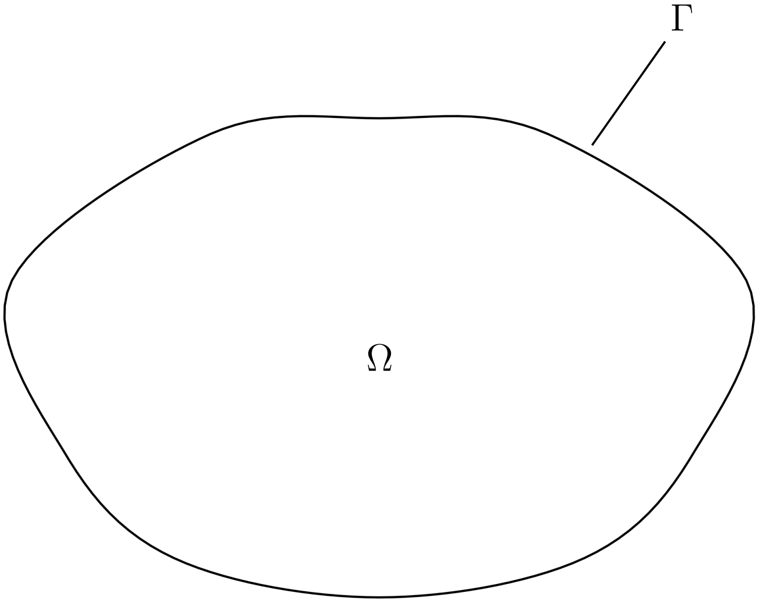

(a) Domain and boundary.

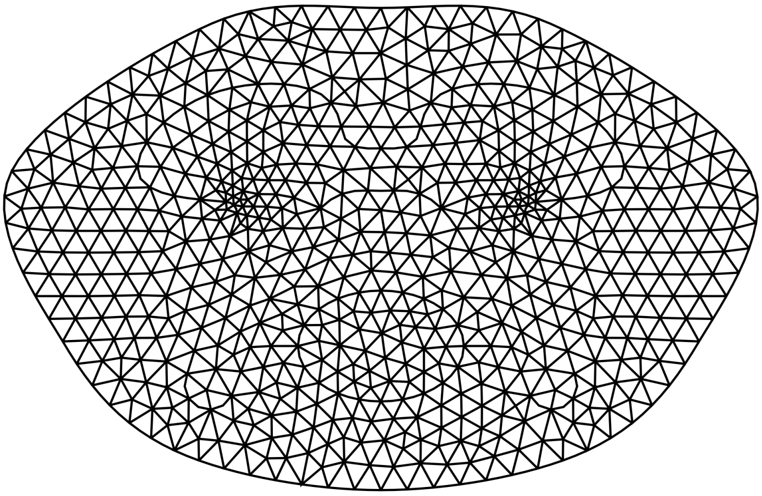

(b) Finite element mesh.

Figure 2.1: Geometry of the spinal cord cross section, indicating the 2.1(a) domain and boundary for solution of the poroelastic equations and 2.1(b) the mesh generated for the finite element solution.

where

$$
\begin{aligned}
N_1 &= (1-s-t)(1-2s-2t) \\
N_2 &= 4s(1-s-t) \\
N_3 &= s(2s-1) \\
N_4 &= 4st \\
N_5 &= t(2t-1) \\
N_6 &= 4t(1-s-t)
\end{aligned}
\tag{2.9}
$$

and s and t are the natural coordinates for the reference element (see Figure 2.2). These shape functions are defined everywhere on the mesh and the global shape functions for the entire domain are given by

$$
\begin{aligned}
\tilde{\boldsymbol{u}} &= \sum_{j=1}^{k} \phi_j \boldsymbol{u}_j \\
\tilde{p} &= \sum_{j=1}^{k} \phi_j p_j \,.
\end{aligned}
\tag{2.10}
$$

Here $\tilde{\boldsymbol{u}}$ and $\tilde{p}$ are global and k is the total number of nodes in the domain. The global shape functions ϕ in Equation (2.10) have the property

$$
\phi_j(u_i, v_i) = \begin{cases} 1 & \text{if } i = j \\ 0 & \text{if } i \neq j \,. \end{cases} \tag{2.11}
$$

This means that the global shape functions are only non-zero at the node j being addressed. In addition, the global shape functions are chosen to be zero everywhere in any element not containing node j. Therefore in any given element, the six non-zero global basis functions associated with the six nodes of the element are identical to the element shape functions in Equation (2.9). That is, in any given element $\tilde{\boldsymbol{u}} = \bar{\boldsymbol{u}}$ and $\tilde{p} = \bar{p}$ where $\bar{\boldsymbol{u}}$ and $\bar{p}$ are approximate solutions for one element. Due to this property we can now consider each element in turn and treat them identically.

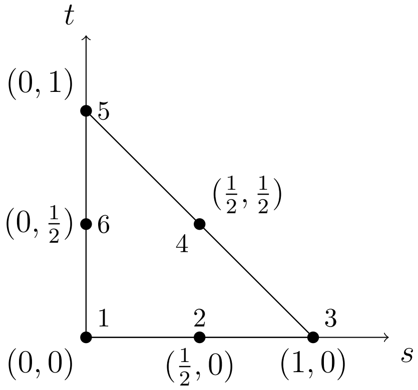

Figure 2.2: Natural (s, t) coordinates of the quadratic triangular reference element. Node labels refer to the shape functions in Equation (2.9).

With these definitions the displacement or pressure anywhere in an element can be approximated using the element shape functions $\boldsymbol{N}$ by (Zienkiewicz and Taylor, 1989; Smith and Griffiths, 2004)

$$\begin{aligned} \boldsymbol{u} \approx \bar{\boldsymbol{u}} &= \sum_{i=1}^{6} N_i \boldsymbol{u}_i^e \\ p \approx \bar{p} &= \sum_{i=1}^{6} N_i p_i^e \,. \end{aligned} \tag{2.12}$$

Here $\boldsymbol{u}_i^e$ and p_i^e are the displacement and pressure values of the six nodes in each element and N_i are the shape functions. The variables $\bar{\boldsymbol{u}}$ and $\bar{p}$ are the approximate solutions for displacement and pressure for each element.

2.2.2 Discretised poroelastic equations

In matrix notation the discretised definition of strain from Equation (2.1) can be written (Zienkiewicz and Taylor, 1989)

$$\boldsymbol{\varepsilon} = \boldsymbol{B}\boldsymbol{u}^e$$

where $\boldsymbol{B}$ is the strain-displacement matrix defined by

$$\boldsymbol{B} = \begin{bmatrix} \frac{\partial N_i}{\partial x} & 0 \\ 0 & \frac{\partial N_i}{\partial y} \\ \frac{\partial N_i}{\partial y} & \frac{\partial N_i}{\partial x} \end{bmatrix} .$$

The stress tensor $\boldsymbol{\sigma_s}$ can be similarly defined

$$\boldsymbol{\sigma_s} = \boldsymbol{D}\boldsymbol{B}\boldsymbol{u}^e \qquad (2.13)$$

where $\boldsymbol{D}$ is the plane strain elasticity matrix

$$\boldsymbol{D} = \frac{E(1-\nu)}{(1+\nu)(1-2\nu)} \begin{bmatrix} 1 & \frac{\nu}{1-\nu} & 0 \\ \frac{\nu}{1-\nu} & 1 & 0 \\ 0 & 0 & \frac{1-2\nu}{2(1-\nu)} \end{bmatrix} . \qquad (2.14)$$

In the elasticity matrix E and ν denote the elastic parameters Young's modulus and Poisson's ratio respectively.

To apply the finite element method to the poroelastic solid skeleton, multiply Equation (2.6) by a test function and integrate over the domain Ω. Using Galerkin approximation the test functions N_j are equal to the shape functions N_i (Zienkiewicz and Taylor, 1989). With definitions (2.13) and (2.14) the discretised solid skeleton equation of motion becomes

$$\rho\frac{\partial^2}{\partial t^2}\left(\int_\Omega \boldsymbol{N}^T\boldsymbol{N}d\Omega\right)\boldsymbol{u} + (1-\phi)\left(\int_\Omega \boldsymbol{B}^T\boldsymbol{D}\boldsymbol{B}d\Omega\right)\boldsymbol{u} - \phi\left(\int_\Omega \boldsymbol{B}^T\boldsymbol{m}\boldsymbol{N}d\Omega\right)\boldsymbol{p} = (1-\phi)\int_\Gamma \boldsymbol{\sigma_s}\cdot\boldsymbol{n}d\Gamma \quad (2.15)$$

where ρ is defined as before, $\boldsymbol{m} = [1 \quad 1 \quad 0]^{\mathrm{T}}$.

The surface integral on the right hand side indicates known normal tractions on the boundary Γ. As the external fluid applying the pressure to the spinal cord is assumed to be inviscid, the shear components of σ_s are zero and the normal stress components are equivalent to $-p_b$. The right hand of Equation (2.15) can be written in terms of pressure as

$$\boldsymbol{F}_s = -(1-\phi)\int_\Gamma p_b\boldsymbol{n}d\Gamma \quad (2.16)$$

where p_b is known pressure on the boundary and $\boldsymbol{n}$ is the unit normal at the surface. Equation (2.15) can be written in the familiar finite element form

$$\rho M\ddot{\boldsymbol{u}} + (1-\phi)K\boldsymbol{u} - \phi Q\boldsymbol{p} = \boldsymbol{F}_s \quad (2.17)$$

where an overdot denotes partial differentiation with respect to time. The coupling matrix Q describes how pore fluid pressure affects stress in the poroelastic material. The mass matrix M describes the mass of the combined fluid and solid and the stiffness matrix K relates to the elasticity of the solid skeleton.

Treating the pore fluid governing equation (Equation (2.8)) in the same way yields

$$\alpha\frac{\partial^2}{\partial t}\left(\int_\Omega \boldsymbol{N}^{\mathrm{T}}\boldsymbol{m}^{\mathrm{T}}\boldsymbol{B}d\Omega\right)\boldsymbol{u} + \frac{1}{M_b}\frac{\partial}{\partial t}\left(\int_\Omega \boldsymbol{N}^T\boldsymbol{N}d\Omega\right)\boldsymbol{p} + \frac{\kappa}{\mu}\left(\int_\Omega \boldsymbol{T}^T\boldsymbol{T}d\Omega\right)\boldsymbol{p} = \boldsymbol{F}_f \quad (2.18)$$

where

$$\boldsymbol{T} = \begin{bmatrix} \frac{\partial N_i}{\partial x} \\ \frac{\partial N_i}{\partial y} \end{bmatrix}$$

and can also be simplified to

$$\alpha Q^T \dot{\boldsymbol{u}} + \frac{1}{M_b} S \dot{\boldsymbol{p}} + \frac{\kappa}{\mu} H \boldsymbol{p} = \boldsymbol{F}_f \tag{2.19}$$

where S is the fluid compressibility matrix, H is the fluid permeability matrix and $\boldsymbol{F}_f$ represents the fluid pressure on the boundary.

Hereafter the constant material parameters ρ, ϕ, α, M_b, κ and μ are assumed to be included in the definitions of the finite element matrices as follows

$$\begin{aligned}
M &= \rho \int_\Omega \boldsymbol{N}^T \boldsymbol{N} d\Omega \\
K &= (1-\phi) \int_\Omega \boldsymbol{B}^T \boldsymbol{D} \boldsymbol{B} d\Omega \\
Q &= \phi \int_\Omega \boldsymbol{B}^T \boldsymbol{m} \boldsymbol{N} d\Omega \\
Q^T &= \alpha \int_\Omega \boldsymbol{N}^{\mathrm{T}} \boldsymbol{m}^{\mathrm{T}} \boldsymbol{B} d\Omega \\
S &= \frac{1}{M_b} \int_\Omega \boldsymbol{N}^T \boldsymbol{N} d\Omega \\
H &= \frac{\kappa}{\mu} \int_\Omega \boldsymbol{T}^T \boldsymbol{T} d\Omega
\end{aligned} \tag{2.20}$$

and the system of poroelastic equations can be written

$$\begin{aligned} &M\ddot{\boldsymbol{u}} + K\boldsymbol{u} - Q\boldsymbol{p} = \boldsymbol{F}_s \\ &Q^T\dot{\boldsymbol{u}} + S\dot{\boldsymbol{p}} + H\boldsymbol{p} = \boldsymbol{F}_f\,. \end{aligned} \tag{2.21}$$

All integrals are evaluated using a 5 point Gauss rule.

2.2.3 Time discretisation

Summing the matrix contributions from Equation (2.2.2) over every element results in the global finite element matrices. Hereafter all finite element matrices and vectors refer to the global matrices and vectors. The global system of poroelastic finite element equations (Equation (2.21)) is a second order system

$$\begin{pmatrix} M & 0 \\ 0 & 0 \end{pmatrix} \begin{bmatrix} \ddot{\boldsymbol{u}} \\ \ddot{\boldsymbol{p}} \end{bmatrix} + \begin{pmatrix} 0 & 0 \\ Q^T & S \end{pmatrix} \begin{bmatrix} \dot{\boldsymbol{u}} \\ \dot{\boldsymbol{p}} \end{bmatrix} + \begin{pmatrix} K & -Q \\ 0 & H \end{pmatrix} \begin{bmatrix} \boldsymbol{u} \\ \boldsymbol{p} \end{bmatrix} = \begin{bmatrix} \boldsymbol{F_s} \\ \boldsymbol{F}_f \end{bmatrix} \tag{2.22}$$

which can be written in the form

$$A_0\ddot{\boldsymbol{x}} + A_1\dot{\boldsymbol{x}} + A_2\boldsymbol{x} = \boldsymbol{F} \tag{2.23}$$

where

$$A_0 = \begin{pmatrix} M & 0 \\ 0 & 0 \end{pmatrix}\,, \quad A_1 = \begin{pmatrix} 0 & 0 \\ Q^T & S \end{pmatrix}\,, \quad A_2 = \begin{pmatrix} K & -Q \\ 0 & H \end{pmatrix}\,,$$

$$\boldsymbol{x} = \begin{bmatrix} \boldsymbol{u} \\ \boldsymbol{p} \end{bmatrix}\,, \quad \boldsymbol{F} = \begin{bmatrix} \boldsymbol{F_s} \\ \boldsymbol{F}_f \end{bmatrix}\,.$$

Equation (2.23) can be solved dynamically using a semi-implicit Crank-Nicholson scheme, which is unconditionally stable (Kwon and Bang, 2000). To discretise the $\ddot{\boldsymbol{x}}$ term, the substitution

$$\boldsymbol{v} = \dot{\boldsymbol{x}} \tag{2.24}$$

is made. Using a time step of size h the solution at time $t + \frac{h}{2}$ is approximated using

$$\begin{aligned}
\dot{\boldsymbol{x}}_{t+\frac{h}{2}} &\approx \frac{\boldsymbol{x}_{t+h} - \boldsymbol{x}_t}{h} \\
\boldsymbol{x}_{t+\frac{h}{2}} &\approx \frac{\boldsymbol{x}_{t+h} + \boldsymbol{x}_t}{2} \\
\dot{\boldsymbol{v}}_{t+\frac{h}{2}} &\approx \frac{\boldsymbol{v}_{t+h} - \boldsymbol{v}_t}{h} \\
\boldsymbol{v}_{t+\frac{h}{2}} &\approx \frac{\boldsymbol{v}_{t+h} + \boldsymbol{v}_t}{2} \, .
\end{aligned} \tag{2.25}$$

Substituting (2.25) into Equation (2.24) yields the expression for calculating $\boldsymbol{x}$ at the next time step

$$\boldsymbol{x}_{t+h} = \boldsymbol{x}_t + \frac{1}{2}h(\boldsymbol{v}_{t+h} + \boldsymbol{v}_t) \, . \tag{2.26}$$

To obtain the expression for calculating $\boldsymbol{v}$ at the next time step, substitute (2.25) then (2.26) into Equation (2.23). Making these substitutions and rearranging we obtain the fully discretised system of equations

$$(4A_0 + 2hA_1 + h^2A_2)\boldsymbol{v}_{t+h} = (4A_0 - 2hA_1 - h^2A_2)\boldsymbol{v}_t - 4hA_2\boldsymbol{x}_t + 4h\boldsymbol{F} \tag{2.27}$$

which, along with Equation (2.26), is solved at each time step.

As $(4A_0 + 2hA_1 + h^2A_2)$ is not symmetric, a suitable iterative solver is used to solve the system at each time step. The BiCGStab (BiConjugate Gradient Stabilized) method is a suitable iterative solver for nonsymmetric problems and is particularly suitable for poroelastic models (Alpak and Wheeler, 2012). A BiCGStab solver from the Harwell Subroutine library is used (HSL (2013)), with a Jacobi preconditioner P^{-1} to improve the speed of the iterations where

$$P = diag((4A_0 + 2hA_1 + h^2A_2))$$

and $diag$ is the diagonal of the matrix $(4A_0 + 2hA_1 + h^2A_2)$.

2.2.4 Mesh generation

Finite element meshes are generated using Gmsh version 3.0.5 (Geuzaine and Remacle, 2009). Three geometries are created, a circle and an annulus mesh for checking the model and an anatomically accurate mesh for the simulations (Figure 2.3). The anatomical mesh is based on a high resolution axial MRI image of the cervical spinal cord (Massire et al., 2016). This gives a good indication of the geometry of the anatomical features required for the model. For example the grey/white matter boundary, the overall shape of the spinal cord cross section and the location of nerve rootlets and denticulate ligaments on the cord boundary (Figure 2.4). Dimensions of the cord mesh are based on human spinal cord measurements, the width and height of the cross section are ~1.3 cm and ~0.8 cm respectively (Ko et al., 2004).

Oedema

Tissue oedema occurs alongside syringomyelia (Fischbein et al., 2000) yet its role in syrinx formation is little understood. The simulated oedema region is meshed in the lower part of the spinal cord white matter (see Figure 2.5). There is little evidence regarding where oedema is likely to form in connection with sy-

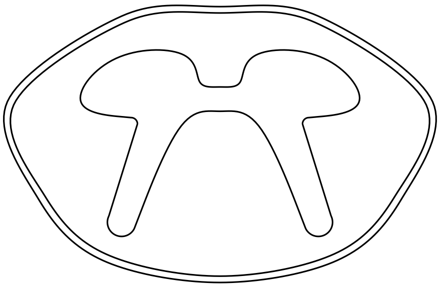

Figure 2.3: Geometry outline of the spinal cord finite element mesh.

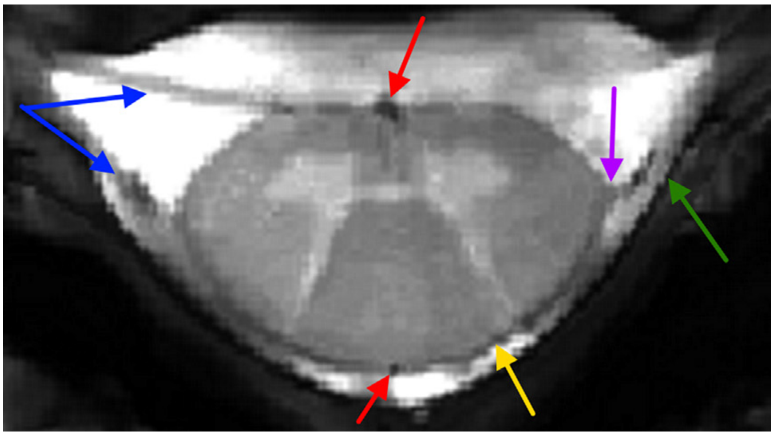

Figure 2.4: Axial MRI image of the cervical spinal cord at the C3 cervical level. The butterfly shaped grey matter region is visible. Several anatomical features are visible (nerve roots: blue, denticulate ligaments: purple, blood vessels: red, dura mater: green, pia mater: yellow) (Massire et al., 2016). *Reproduced with permission.*

ringomyelia. However, cases of experimentally induced syringomyelia have found extracellular oedema in the white matter (Naruse et al., 2000) and in both grey and white matter regions (Klekamp et al., 2001) so a modelled region of oedema in the white matter is not unreasonable.

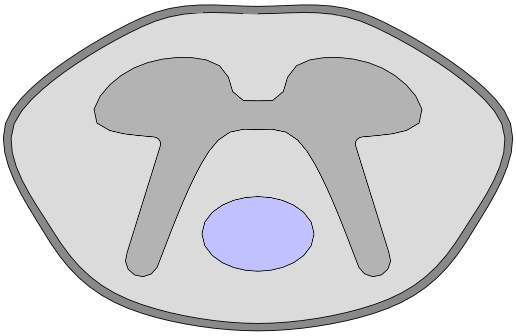

Figure 2.5: Spinal cord mesh geometry, the oedema region is shown in blue, the grey matter and pia mater regions are dark grey.

Pia mater

The pia mater is a very thin membrane (approximately 15 µm (Reina et al., 2004)) closely attached to the entire surface of the brain and spinal cord. It is significantly stiffer (Mazuchowski and Thibault, 2003) than grey and white matter and although its porosity and permeability have not been directly measured, it is thought to be less permeable (Elliott, 2012). As a consequence, the pia mater is thought to influence pressure inside the spinal cord tissue (Harwell et al., 2016). The pia mater has been included in some existing models of the cord (Støverud et al., 2016a).

Grey and white matter

Grey and white matter are thought to have different Young's moduli, Poisson's ratios, porosities and permeabilities and these differences have been included in existing computational models (Czyz et al., 2008; Sparrey et al., 2009; Sarntinoranont et al., 2006; Støverud et al., 2016a). In the present model mesh elements in the grey and white matter regions (Figure 2.5) are assigned different tissue properties.

2.3 Boundary conditions

To obtain a unique solution to the poroelastic equations, boundary conditions must be imposed. A graphic representation of boundaries included in the model mesh can be seen in Figure 2.6.

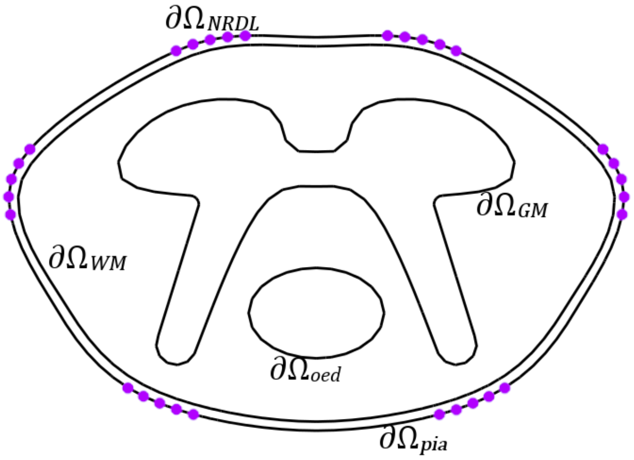

Figure 2.6: Boundaries between tissue regions in the finite element model. The regions tethered by nerve roots and denticulate ligaments are indicated by purple dots.

2.3.1 Nerve roots and denticulate ligaments

The spinal cord is tethered in approximately the centre of the spinal canal by NRDL. These are thought to apply a slight tension to the cord (Tunturi, 1978) and prevent the cord from moving more than ~0.5 mm in the radial direction (Cai et al., 2007). NRDL are represented in the model as solid skeleton displacement restraints

$$\boldsymbol{u} = 0 \text{ on } \Gamma_{NRDL}$$

which serve the dual purpose of simulating NRDL tethering and preventing rigid body motion of the dynamic cord model.

2.3.2 Cerebrospinal fluid pressure changes

The link between syringomyelia and CSF flow obstructions is well established (Flint and Rusbridge, 2014), although how this flow obstruction internally affects the spinal cord tissue in the context of syrinx formation is not completely clear. The effect of disturbed CSF flow on the cord is simulated by applying normal traction and pressure boundary conditions to the edge of the spinal cord model.

The external boundary Γ is split into two parts such that

$$\Gamma = \Gamma_{NRDL} \cup \Gamma_{pia}$$

where Γ_{NRDL} represents the location of NRDL on the cord boundary and Γ_{pia} represents non-restrained areas of the cord pia mater that are directly exposed to CSF pressure changes.

The solid skeleton boundary condition is a normal traction applied to Γ_{pia} and the pore fluid boundary condition is a known pressure on the cord boundary Γ.

The boundary conditions are

$$\begin{aligned} \boldsymbol{\sigma}_s &= \boldsymbol{F}_s \text{ on } \Gamma_{pia} \\ p &= p_b \text{ on } \Gamma \end{aligned} \tag{2.28}$$

where $\boldsymbol{F}_s$ is that of Equation (2.16) and p_b is again the known pressure on the boundary of the cord. The known pressure on the boundary of the cord is the pressure in the CSF surrounding the cord.

As there is little available data regarding *in vivo* CSF pressure values, several spinal cord models have approximated this with a sine wave (Bertram and Heil, 2017; Linge et al., 2013; Støverud et al., 2013). Here the applied CSF pressure is approximated using

$$p_b = A(\tfrac{1}{2} - \tfrac{1}{2}\cos(2\pi t)) \tag{2.29}$$

as both the function and its first derivative are zero at $t = 0$. Here A is the amplitude of pressure applied to the spinal cord by the surrounding CSF and t is time in seconds and (2.29) simulates the effect of CSF pressure changes due to pulse (Figure 2.7). An evaluation of measured CSF pressure values in the SAS is given in Chapter 3.

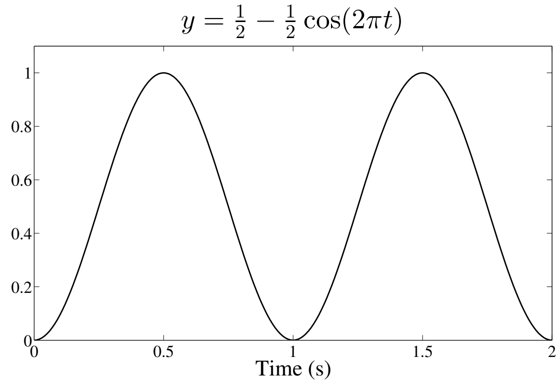

Figure 2.7: CSF changes due to pulse are approximated by $y = \frac{1}{2} - \frac{1}{2}\cos(2\pi t)$.

2.3.3 Tissue boundaries

Several interfaces between tissue types with different material properties are included in the model (Figure 2.6). These are the boundaries between white matter and the pia mater (Γ_{WM}), grey matter and white matter (Γ_{GM}) and tissue oedema and white matter (Γ_{oed}). Due to the finite element discretisation, displacements and pressures are continuous across these tissue boundaries and the boundary conditions are natural.

2.4 Summary

A plane strain poroelastic model of the spinal cord tissue and its finite element solution has been presented. The relationship between syringomyelia cavity formation and CSF disturbances is a prominent part of syringomyelia research and a poroelastic model is able to explore this relationship further. Poroelasticity provides a means to better understand the processes underlying cavity formation through examining tissue stress and fluid pressure within the cord.

Inertial effects have been included and whilst the geometry has been simplified to two dimensions, several anatomical features of the cord cross section have been included. The inclusion of separate grey and white matter regions and NRDL restraints allows the effects of these anatomical features on stress and pressure within the cord tissue to be evaluated. A region of oedema has been modelled and the mechanical effect of oedema on the spinal cord tissue can be investigated, which to date has not been addressed. For this model, as with any numerical model of a biological system, values that represent tissue properties as accurately as possible are required.

Chapter 3

Properties of spinal tissues

Introduction

In any computational model of a biological system, the accuracy of the final output is dependent on the quality of the input parameters. Mathematical models of the spinal cord have become increasingly common and as a result more work has been undertaken to characterise the mechanical properties of spinal cord tissue (Clarke et al., 2009; Fiford and Bilston, 2005; Ozawa et al., 2004; Sparrey and Keaveny, 2011). Spinal cord grey and white matter are comprised of several complex components such as neurons, glial cells, extracellular fluid (ECF), blood vessels and axons and each of these components has its own set of material properties (Koser et al., 2015; Lu et al., 2006; Shreiber et al., 2009). Similarly, anatomical features such as the pia mater have unique properties (Mazuchowski and Thibault, 2003).

In Section 3.1 the material parameters required for the present poroelastic model will be outlined, along with a definition of what they describe in spinal cord tissue. Next, a review of the current state of spinal cord tissue characterisation is given in Section 3.2. Sections 3.3 to 3.6 review what is currently known about the properties of ECF, pia mater, oedema and CSF. The wide range of measured properties in the literature demonstrates the challenges faced by researchers attempting to characterise CNS tissues. At present an appreciable volume of work has been carried out to measure the elastic parameters of spinal cord tissue (Cheng et al., 2008), whereas porosity and permeability studies are less common. A comparison of existing parameters from the literature is given in Section 3.2.6; results from brain tissue experiments have been included where spinal cord tissue results are scarce.

3.1 Poroelastic parameters

The equations of linear poroelasticity describe a two compartment material, defined by the solid skeleton and the pore fluid that can move within it. A summary of the material parameters required to fully describe a linear poroelastic material can be seen in Table 3.1.

Table 3.1: Parameter summary.

Symbol	**Parameter**	**Unit**
κ	Permeability	m^2
E	Young's modulus	Pa
ν	Poisson's ratio	-
ϕ	Porosity	-
μ	Dynamic viscosity	Pa s
ρ_f	Fluid density	$\mathrm{kg\,m^{-3}}$
ρ_s	Solid density	$\mathrm{kg\,m^{-3}}$
α	Biot-Willis coefficient	-
M_b	Biot modulus	-

Spinal cord tissue is vastly more complex than a simple two compartment material. In summary, grey and white matter consist of many parts such as neuron cell bodies, astrocytes, glial cells and axons all of which are surrounded by ECF (Tortora and Derrickson, 2014). In the poroelastic model, the cellular components and ECF are designated as the solid skeleton and pore fluid respectively. Both grey and white matter have their own set of elastic properties, furthermore the elasticity of individual cells may differ (Lu et al., 2006). The impact of several subcellular components of CNS cells on overall elastic properties has been studied (Ouyang et al., 2013), however the inclusion of this subcellular detail is beyond the scope of the present work. Due to the complex nature of grey and white matter, before poroelastic material parameters for the spinal cord can be determined the regions of tissue that they describe must be defined.

For the present model, the solid skeleton of white matter is defined as the myelinated axons that run the length of the cord. The solid skeleton of grey matter is defined as neuron cell bodies, shorter unmyelinated axons and glial cells. The ECF that surrounds the grey and white matter cells occupies the region described by porosity ϕ, that is the ECS. Figure 1.3 in Chapter 1 gives an indication of the structures of grey and white matter. Cells that make up the solid skeleton also have a high fluid content so cannot strictly be considered a solid. However, fluid movement across cell boundaries is assumed to be slower than fluid movement in the ECS and the cells that make up spinal cord tissue are assumed to be an impermeable solid skeleton for the purposes of this particular model.

3.1.1 Elasticity

3.1.1.1 Young's modulus

Young's modulus (YM) E defines the strain ε a material undergoes when a specified stress σ is applied. This relationship is given by

$$\sigma = E\varepsilon$$

In the linear poroelastic model described in Chapter 2, the value of E describes the elasticity of the solid skeleton, not the overall material.

It has been demonstrated that the YM of grey and white matter differ and furthermore that both tissues exhibit some anisotropic properties (Budday et al., 2015; Ichihara et al., 2001; Koser et al., 2015). For example, white matter consists of well ordered axons so YM is different depending on whether it was measured parallel to or perpendicular to these axons. Grey matter is more disordered than white matter and although some anisotropy has been noted (Koser et al., 2015) it is often treated as an isotropic material for modelling purposes (see for example (Cheng and Bilston, 2007; Heil and Bertram, 2016)).

Koser et al. (2015) confirmed the anisotropy of white matter and to a lesser extent grey matter, although they found that at lower strains (with a ratio of ~0.996 between the original and deformed state) grey matter behaved as a predominantly isotropic material. This study also found that at lower strains overall tissue elasticity is similar to the elasticity of individual neurons and glial cells suggesting that at low strains CNS tissue elasticity is dominated by the elasticity of the individual cells. However as the indenter used was small (spherical diameter 37 µm) only a few cells would have been in contact with the indenter, implying that it was the elasticity of the cells themselves that was being measured.

Component properties of grey and white matter give an indication of the overall tissue stiffness. Myelin and glial cells have been found to contribute significantly to CNS tissue stiffness (Shreiber et al., 2009; Weickenmeier et al., 2016), although elasticity measurements of individual glial cells has shown them to be softer than the surrounding neurons (Lu et al., 2006). A possible explanation for this is that the softer glial cells allow tissue samples to stretch before failure during testing. There is contradictory information regarding whether grey (Bilston, 2016; Ichihara et al., 2001; Koser et al., 2015) or white (Budday et al., 2015; Weickenmeier et al., 2016) matter is stiffer. There are numerous factors that influence the measured YM of CNS tissue; for example white matter axons straightening during testing may produce a stiffer elastic response (Bilston, 2016).

In addition to the inherent structural differences there are several other factors that are thought to, or have been shown to, affect the elastic qualities of CNS tissues. Both age and species may affect the mechanical properties of CNS tissues (Cheng et al., 2008; Clarke et al., 2009), with age this is possibly due to varying degrees of myelination (Weickenmeier et al., 2016). Fiford and Bilston

(2005) observed different reactions between spinal cord levels (cervical, thoracic and lumbar) during testing, however these differences have not been thoroughly investigated. The length of time *post mortem* may also affect measured YM values although these effects are thought to be minimal (Budday et al., 2015; Metz et al., 1970). Finally, the testing technique itself can often result in very different YM values. The influence of techniques such as tensile testing, compression, elastography and indentation on measured YM values will be described in Section 3.2.

3.1.1.2 Poisson's ratio

Poisson's ratio (PR) ν describes the ratio between axial and transverse strain, that is how much a material deforms in one direction when deformed due to a load applied in the other direction. Saturated poroelastic materials have a complicated PR, as when a material is deformed in the axial direction the transverse deformation can change as fluid within the material shifts or escapes (Wang, 2000). However, the PR required in the constitutive equation described in Chapter 2 describes the PR of the solid skeleton only.

3.1.1.3 Density

Density ρ is the mass per unit volume of a material. There are no apparent studies of the density of spinal cord tissue specifically although other biological tissues such as brain have been tested (Barber et al., 1970). The density value for the linear poroelastic spinal cord model, $\rho = (1-\phi)\rho_s + \phi\rho_f$, requires the density of both the pore fluid and the solid skeleton. Although the solid skeleton excludes ECS regions, the water content of the cells themselves is high so a density value near that of water is not unreasonable.

3.1.2 Fluid transport

3.1.2.1 Porosity

Porosity ϕ is a dimensionless parameter that indicates what fraction of a poroelastic material contains the fluid filled pores. The structures of grey and white matter are different, as such the regions defined by ϕ will be different. White matter mainly consists of myelinated axons of neurons, ordered in tracts along the length of the spinal cord along with the glial cells surrounding them. Grey matter is composed of neuron cell bodies, shorter unmyelinated axons, dendrites and glial cells and is structurally more complicated. In both grey and white matter the fluid filled ECS surrounding these cells is assumed to be the region described by porosity ϕ.

Fluid within cells is not included in the porosity value, as on the timescales being modelled the movement of fluid through the cell wall boundary is assumed to be slower than movement through the ECS. Furthermore, for the present poroelastic model, blood vessels are not included in the porosity value but are included in the solid skeleton as the ECF and blood compartments do not communicate with one another under normal circumstances. Multi-compartmental poroelastic models of the brain have included the blood to learn more about the dynamic equilibrium these compartments maintain with one another (Eisenträger, 2012; Wirth and Sobey, 2009; Sobey and Wirth, 2006).

In reality the ECS does not have one fixed porosity value and is likely to be affected by pore fluid pressure, solid skeleton strain and even biochemical factors. Variable porosity is not included in the present model although different tissue regions such as pia mater, grey matter and white matter have been allocated different porosities.

3.1.2.2 Permeability

Intrinsic permeability κ is a measure of pore size and interconnectivity and in the present model it refers to the ease with which ECF can move through the spinal cord ECS. Occasionally 'permeability' is used to mean hydraulic conductivity k which takes into account properties of the fluid passing through the material and is defined by

$$k = \frac{\kappa \rho_f}{\mu}$$

where ρ_f and μ are fluid density and dynamic viscosity respectively (Jaeger et al., 2007).

The value of permeability used in the present model refers to the movement of ECF through the region defined by ϕ. White matter consists primarily of bundles of myelinated axons of neurons and as such the permeability is likely to be anisotropic, as fluid moves more easily in the direction of the axons than across them (Sarntinoranont et al., 2003). Grey matter permeability is often assumed to be isotropic (Bertram and Heil, 2017; Sarntinoranont et al., 2003; Støverud et al., 2016a). Furthermore the permeabilities of grey and white matter are thought to differ (Nicholson, 2001) and including these differences in the poroelastic model may explain some of the cord fluid behaviour that occurs prior to cavity formation.

There is uncertainty as to whether healthy fluid transport within brain and spinal cord ECS is governed by bulk flow or diffusive movement (Klekamp et al., 2001; Syková and Nicholson, 2008). It has been suggested that diffusive movement dominates in CNS tissue and that only in exceptional circumstances, such as tissue oedema, can bulk flow be permitted to occur (Syková and Nicholson, 2008). However, there is evidence to suggest that bulk flow can occur in these tissues, particularly along white matter pathways (Abbott, 2004).

In relation to syringomyelia, pressure gradients between the spinal cord and SAS have been observed near experimentally induced syringomyelia implying that bulk flow, if permitted, could occur (Klekamp et al., 2001). Wong et al. (2012) demonstrated that when dye is injected directly into a syrinx, the resultant fluid movement from the syrinx to the surrounding tissue is largely governed by bulk flow. As tissue oedema is implicated in syrinx development, the increased porosity (fluid volume) found with oedema could explain why evidence for bulk flow in the spinal cord has been observed in these cases.

The poroelastic model described in Chapter 2 uses Darcy's Law to model fluid movement, which is essentially approximating bulk flow with diffusive movement. Values for permeability κ used in other models are often taken from the literature, where either a diffusion coefficient, hydraulic conductivity or intrinsic permeability value is given (Bertram and Heil, 2017; Harris and Hardwidge, 2010; Heil and Bertram, 2016; Sarntinoranont et al., 2003; Støverud et al., 2016a). Permeability is notoriously difficult to measure, even in homogeneous materials (Jaeger et al., 2007); consequently the range of permeability values used in existing poroelastic spinal cord models varies widely.

3.1.2.3 Biot-Willis coefficient

The Biot-Willis coefficient α, also known as the Biot coefficient or effective stress coefficient, is the ratio of pore fluid volume change to overall material volume change when the pore pressure remains constant (Detournay and Cheng, 1993; Coussy, 2004). Biot-Willis coefficients for CNS tissues are not well known (Eisenträger, 2012).

3.1.2.4 Biot modulus

The Biot modulus M_b, also called the inverse storage coefficient, is the increase in fluid content when the pressure is increased but the solid skeleton strain is held constant (Coussy, 2004; Detournay and Cheng, 1993). Like the Biot-Willis coefficient, the Biot modulus of spinal cord tissue has not been studied extensively although values have been suggested and calculated (Eisenträger, 2012; Wirth and Sobey, 2009).

3.1.2.5 ECF and CSF pressure

ECF within the spinal cord and CSF in the SAS surrounding the cord have a non-zero pressure. The ECF pressure can be used as an initial pore pressure condition for the poroelastic spinal cord model, however for modelling purposes the initial pressure has been set to zero. As such, for the CSF pressure values used to load the model, it is the relative rather than absolute pressure values that are required. Values of CSF pressure in the spinal SAS have been acquired through both invasive methods (Heiss et al., 1999, 2012) and CFD simulations (Clarke et al., 2013; Rutkowska et al., 2012).

3.2 Spinal cord tissue

There are numerous experimental techniques for measuring spinal cord tissue properties and the resulting parameter values are influenced by several factors. For the solid skeleton parameters YM and PR the scale at which measurements are taken is particularly important, whether this is macro (large tissue sample) or micro (cellular). A large tissue sample has different tissue properties compared to its individual cellular components, for example the YM of an individual axon is different to a sample of white matter containing many of these axons.

The poroelastic model presented in this thesis does not represent individual cell-cell interactions, rather it simulates the overall behaviour of a representative volume of tissue. Despite this, micro scale experimental measurements are still beneficial. The poroelastic model is comprised of a solid skeleton (cells) containing many interconnected pores (ECS) and it is the mechanical properties of the solid skeleton, not the overall poroelastic material, that are required for YM and PR.

Similarly fluid transport in spinal cord tissue has been measured using several experimental techniques, each having its own advantages and limitations. Here an outline of elasticity and fluid transport properties of spinal cord tissue is presented. Experimental technique strongly influences the measured properties of spinal cord tissue and the effects of technique on measured parameters are described. In light of this, the parameters chosen for the poroelastic model are highlighted and their choice is justified.

3.2.1 Young's modulus

Reported spinal cord YM values span several orders of magnitude and are influenced by the technique used to measure it (Cheng et al., 2008). Cellular or grey/white matter only values required for a poroelastic model are less common and present the challenge of testing a tissue sample without the ECF or surrounding pia mater. Furthermore, both grey and white matter are complex tissues with several different cellular components each with differing properties (Lu et al., 2006).

Spinal cord YM values are often obtained using either tensile testing, compression testing or indentation. Tensile testing largely yields higher YM values than compression and indentation, as the sample length for compression and indentation is usually much smaller than for tensile testing (McKee et al., 2011). Where a similar YM has been measured with more than one experimental technique, the same size sample has been used, as in Koser et al. (2015). Spinal cord tissue has been shown to exhibit strain stiffening behaviour, that is higher strain rates and strains result in a higher YM value being reported; consequently the experimental strain rate and strain affect the measured YM (Cheng et al., 2008).

Spinal cord tissue YM has been measured using a wide range of strain rates (see Column 1, Table 3.2). Very high strain rates ($>5\,\mathrm{s}^{-1}$) do not correspond to realistic deformations that would happen *in vivo* but are more similar to traumatic spinal cord injury (SCI) conditions (Bilston, 1994). Lower strain rates (0.001–$0.3\mathrm{s}^{-1}$) are closer to the deformations that would happen to the spinal cord *in vivo*, for example from movement of the spine or from CSF pressure (Bilston and Thibault, 1996).

Values in the literature

Measured YM values can be seen in Table 3.2, along with corresponding tissue type, testing technique and strain rate. Values range from 70–1 400 000 Pa; this highlights the extent of strain stiffening behaviour in the spinal cord along with the influence of different testing techniques, the variation between grey matter, white matter and pia mater tissues and the effects that age or species may have on spinal cord elastic properties.

Tensile testing values in Table 3.2 are comparatively high although in reality spinal cord YM is likely to be much lower than the values measured using tensile testing. For spinal cord samples, the higher values are likely due to the fact that whole cord samples with the pia mater intact were used so the measurement was dominated by the much stiffer pia mater. This effect was demonstrated by

Mazuchowski and Thibault (2003) who revealed that YM of the spinal cord with and without the pia mater differs by a ratio of almost 15 : 1. The tensile test by Bilston et al. (2006) describes removing the dura mater but not the pia mater of a cord sample and they measured a YM of 1.37 MPa. This is in good agreement with the YM value found by Mazuchowski and Thibault (2003) with the pia mater intact, suggesting a possible value for the YM of pia mater tissue.

YM values have also been obtained by fitting compression and tensile test data to finite element models. Various material models have been used to represent spinal cord tissue in these finite element simulations such as linear elastic, viscoelastic, hyper-viscoelastic, poroelastic and poroviscoelastic (Cheng and Bilston, 2007; Franceschini et al., 2006; Miller et al., 2000; Nishida et al., 2013; Sparrey and Keaveny, 2011). Alongside providing information regarding spinal cord material properties, this has the additional benefit of indicating which material model is most appropriate for CNS tissue. Following a series of tests on human brain tissue Franceschini et al. (2006) found that poroelasticity captures the behaviour of brain tissue, particularly when a viscoelastic solid skeleton was incorporated.

For a poroelastic spinal cord model the YM value required is that of the solid skeleton. Here the solid skeleton is assumed to be the cells that make up grey and white matter; in this respect indentation tests, particularly microindentation, are more relevant for measuring elasticity values for a poroelastic finite element model. In the literature these tests generally produce lower values (~1000 Pa) such as in Weickenmeier et al. (2016). Another potential technique for measuring only the solid skeleton YM is the use of preloading. Cheng and Bilston (2007) implemented a preloading technique whereby the tissue was incrementally compressed in an attempt to eliminate ECF so only cells were being tested. This yielded a YM value of 350 Pa. Sparrey and Keaveny (2011) begun compression testing immediately after applying a small preload and found that the preload

Table 3.2: Measured Young's modulus E values. All Young's modulus and strain rate units are Pa and s^{-1} respectively unless otherwise stated. SC - spinal cord, GM - grey matter, WM - white matter, AFM - atomic force microscopy, Comp. - compression, Elast. - elastography, Neu. - neuron, Gl. - glia, FE - finite element. *Shear modulus G, where $E \approx 2G$.

Strain rate	**Young's Mod.**	**Technique**	**Species**	**Tissue type**	**Author**
0.001	1389	Indentation	Cow	Brain GM	Budday et al. (2015)
	1895			Brain WM	
-	2750*	Indentation	Rat	Brain cortex	Lee et al. (2014)
0.001	680	Indentation	Cow	Brain GM	Weickenmeier et al. (2016)
	1330			Brain WM	
0.0001	250–350	Comp.	Cow	Brain WM	Cheng and Bilston (2007)
0.001					
0.01					
30	19 kPa	Comp.	Pig	Brain	Rashid et al. (2012)
60	28.2 kPa				
90	37.9 kPa				
0.005	172*	Comp.	Pig	SC	Sparrey and Keaveny (2011)
0.05	332*				
0.5	569*				
5.0	710*				

Strain rate	Young's Mod.	Technique	Species	Tissue type	Author
0.068	1020 kPa	Tensile	Human	SC	Bilston and Thibault (1996)
0.14	1170 kPa				
0.21	1370 kPa				
0.05	988 kPa	Tensile	Cow	SC GM	Ichihara et al. (2001)
0.05	375 kPa			SC WM	
0.2,1,10	89 kPa	Tensile	Human	SC	Mazuchowski and Thibault (2003)
0.1,1,10	1400 kPa			SC & pia	
5.5	128.6 kPa	Tensile (FE)	Pig	Brainstem axon	Javid et al. (2014)
	4290			Brainstem ECM	
-	5000	Tensile	Pig	SC	Ozawa et al. (2004)
0.00625	742	Tensile	Pig	Brain	Chen et al. (2014)
0.02	130	AFM	Mouse	SC GM	Koser et al. (2015)
	70			SC WM	
20	480/300	AFM	Cow	Brain Neu./Gl.	Lu et al. (2006)
30	970/520				
-	7085	Elast.	Cat	Brain GM	Pattison et al. (2010)
	8322			Brain WM	

increased the effective stiffness of the tissue (again, this was ~1000 Pa), further demonstrating the strain stiffening effects present in CNS tissues.

Tissue sample considerations

The vast majority of spinal cord YM testing has been carried out on *ex vivo* samples which may impact the mechanical response of the tissue. For example dehydration affects the elastic properties of soft tissue (Nicolle and Palierne, 2010) although how long tissue samples were exposed to air and allowed to dehydrate is not always recorded. When the spinal cord is removed from the spinal canal it is no longer supported by the surrounding CSF. The density and YM of spinal cord tissue are low enough for it to lose its shape when removed from the CSF, this can be observed visually. Consequently, tests that are carried out will produce different effective elasticity results when the cord is removed from the CSF.

An interesting consideration is how the observed strain stiffening behaviour of *ex vivo* samples (Ichihara et al., 2001; Koser et al., 2015) affects the YM of spinal cord tissue *in vivo*. The cord is tethered in the spinal canal by nerve rootlets and denticulate ligaments which apply a slight tension to it (Tunturi, 1978). As strain stiffening behaviour has been observed in spinal cord tissue, the *in vivo* YM may be higher than the measured *ex vivo* YM as the cord is under constant tension *in vivo*. Changes in posture produce different strains in the spinal cord Harrison et al. (1999). Due to the strain stiffening properties of the spinal cord this implies that the YM of the cord could be altered in certain postures. Furthermore, tissue blood perfusion is also thought to contribute to tissue stiffness (Bilston, 2002), a factor missing in *ex vivo* samples. Consequently, it is not unreasonable to use slightly higher values in the model than values found using *ex vivo* samples.

Young's modulus values for the poroelastic model

There is no information available in the literature regarding strain rates applied to the spinal cord *in vivo*, although it has been suggested that strain rates in the region of 0.07–0.2 s^{-1} are typical for normal movement and physiological processes (Bilston and Thibault, 1996). Brain tissue indentation studies (see Table 3.2) at very low strain rates give YM of the order of 1-2kPa, which is lower than those thought to be found *in vivo.* Although tests on smaller regions of tissue (such as with indentation) are more appropriate for obtaining poroelastic solid skeleton YM values, selecting higher values for the model is not unreasonable. Several factors potentially increase the YM of grey and white matter *in vivo* such as the tension applied by denticulate ligaments (Tunturi, 1978), strain stiffening behaviour of the tissue (Cheng et al., 2008) and tissue blood perfusion (Bilston, 2002).

With this in mind a YM of $\sim$5000 Pa is an appropriate value to use in the model, in line with values used in other poroelastic cord models (Bertram, 2010; Bertram and Heil, 2017; Heil and Bertram, 2016; Støverud et al., 2016a). Ozawa et al. (2004) measured this value using compressive and tensile tests on whole cord samples, however the load was applied radially and the stiffening effects of the pia mater were taken into account. Radial YM measurements are beneficial in the present plane strain model that examines the cord cross section. There is still uncertainty as to whether grey or white matter is stiffer and it has been suggested that brain white matter is slightly softer than grey matter (Bilston, 2016). However, there are also brain studies that show the opposite (Budday et al., 2015; Pattison et al., 2010; Weickenmeier et al., 2016). Of the few studies comparing spinal cord grey and white matter, white matter has been reported as softer (Ichihara et al., 2001; Koser et al., 2015), by a factor of approximately 2. On this basis, the grey and white matter values used in the model will be

10 000 Pa and 5000 Pa respectively.

3.2.2 Poisson's ratio

For a poroelastic model, the required PR describes properties of the solid skeleton rather than the overall material (Coussy, 2004). The main compartments of spinal cord tissue, that is cells, ECF and blood, are effectively incompressible due to their water content (Elliott et al., 2017). Consequently, some poroelastic models of the spinal cord have used a near incompressible PR ($\nu \approx 0.5$) (Harris and Hardwidge, 2010; Støverud et al., 2016a), although others have used a lower value (Bertram and Heil, 2017; Heil and Bertram, 2016). There is a paucity of experimental data to validate these choices, although Ichihara et al. (2001) found the PR of both grey and white matter was approximately 0.4. This value is for large (20 mm) tissue samples containing numerous cells, however it still provides a useful indication of spinal cord tissue compressibility.

Throughout the cardiac cycle the alternating volumes of venous and arterial blood vessels, ECF, cells and external CSF are thought to maintain a dynamic equilibrium with each other, an effect known as the Monro-Kellie hypothesis (Mokri, 2001). As external CSF and blood vessels are not included in the present model, a small degree of modelled spinal cord compressibility would compensate for the volume exchange between the CSF and spinal cord despite the solid skeleton itself being largely incompressible. Porosity is static in the present model which is not the case *in vivo* as local changes may occur as the spinal cord is subjected to CSF loading. This further supports the use of a lower PR ($\nu = 0.4$) which can account for these changes in a cord only model.

3.2.3 Density

As biological tissue is largely water its density is often assumed to be between approximately 900 and 1100 $\mathrm{kg\,m^{-3}}$. Measurements of brain tissue density have found it to be around 1050 $\mathrm{kg\,m^{-3}}$ (Barber et al., 1970). Existing models of the cord have modelled the density as equal to (Bertram, 2010; Heil and Bertram, 2016) or slightly higher than (Harris and Hardwidge, 2010; Persson et al., 2011; Cheng et al., 2014) the density of water, that is 1000–1100 $\mathrm{kg\,m^{-3}}$. Based on the reported value for brain tissue, and in line with existing models, the density of spinal cord tissue is taken to be 1050 $\mathrm{kg\,m^{-3}}$.

3.2.4 Biot-Willis coefficient

For the case of incompressible constituents, the assumption that the Biot-Willis coefficient $\alpha = 1$ is sufficient. However, due to the complex volume relationships that occur in the CNS, values less than or even greater than one may be possible (Sobey and Wirth, 2006). Most poroelastic models that have addressed this parameter have assumed $\alpha = 1$ (Heil and Bertram, 2016; Bertram and Heil, 2017), arguing that the cord tissue and fluid represent a fully saturated incompressible system. Models of the cord that have accounted for the volume change of blood vessels in the cord have calculated a Biot-Willis coefficient of $\alpha \approx 0.9995$ (Wirth and Sobey, 2009). This value has been used for the present model, assuming a slightly compressible solid skeleton.

3.2.5 Biot modulus

The Biot modulus can be defined as (Wang, 2000)

$$M_b = \frac{\beta K_s}{\alpha(1 - \alpha\beta)} \tag{3.1}$$

where α is the Biot-Willis coefficient, β is the Skempton coefficient and K_s is the bulk modulus of the solid skeleton. Skempton's coefficient β has been previously approximated for CNS tissue as $\beta = 1$ (Wirth and Sobey, 2009). Substituting this into Equation (3.1) the Biot modulus definition can be written as

$$M_b = \frac{K_s}{\alpha(1 - \alpha)} \, . \tag{3.2}$$

The bulk modulus K_s is given in terms of Young's modulus E and Poisson's ratio ν by (Bower, 2010)

$$K_s = \frac{E}{3(1 - 2\nu)} \, .$$

It is uncertain whether the definition of the Biot modulus in Equation (3.1) holds for spinal cord tissue. In the model a value of $M_b = 10000$ is used, resulting in a storage coefficient of $\frac{1}{M_b} = 0.0001$, and different values of M_b are compared.

3.2.6 Fluid transport

Whilst there has been an appreciable volume of work carried out to characterise the elastic properties of spinal cord tissue there has been relatively little work to characterise its porosity and permeability. Porosity values in spinal cord tissue have been measured using tracers and are often in the region of 0.15-0.2 for healthy tissue (Nicholson, 2001). Three main techniques have been used to measure diffusion coefficients or to calculate permeability of spinal cord tissue. These are measuring tracers in the tissue (Nicholson and Syková, 1998; Syková and Nicholson, 2008), fitting compression test data to computational models (Cheng and Bilston, 2007) and using diffusion weighted magnetic resonance imaging (DW-MRI) to reveal tissue structure (Sarntinoranont et al., 2006; Shahim et al., 2010). In soil mechanics, intrinsic permeability is traditionally calculated using mechanical test data (Jaeger et al., 2007). However no apparent studies have applied this method to spinal cord tissue, likely due to the difficulties in applying and measuring a pressure gradient applied to the spinal cord and quantifying the resultant ECF movement.

Permeability values for CNS tissue can be seen in Table 3.3, where brain tissue experiments are included due to the scarcity of available spinal cord data. Existing poroelastic spinal cord models have used a range of permeability values for tissue, the order of which ranges from 1×10^{-12} to $1 \times 10^{-15}\,\mathrm{m}^2$ (Bertram and Heil, 2017; Heil and Bertram, 2016; Støverud et al., 2016a). These values are often taken from previous models that obtained these values from earlier works such as those shown in Table 3.3. Consequently there is a need to develop a technique for evaluating the porosity and permeability of spinal cord tissue. Non-invasive methods are particularly advantageous as they can be used *in vivo* and have the potential for clinical applications. Chapter 4 presents the development and preliminary findings of a DW-MRI based technique for deriving spinal cord porosity and permeability values. These porosity and permeability values have been used to improve the current poroelastic model.

3.3 Extracellular fluid

For a poroelastic model, properties of the pore fluid are also required. In a model of the spinal cord, the ECF is assumed to play the role of the pore fluid moving

Table 3.3: Tissue permeability values in the literature, all units are m^2. GM - grey matter, WM - white matter. Where hydraulic conductivity k values were given, these were converted to permeability κ using a viscosity of $\mu = 1\,\mathrm{mPa\,s}$ (Jaeger et al., 2007).

Tissue type	**Permeability**	**Author**
Brain WM	1.6×10^{-14}	Reulen et al. (1977) (cited in Kaczmarek et al. (1997))
Brain GM	1.6×10^{-16}	
Brain	2×10^{-15}	Morrison et al. (1994) (cited in Smith and Humphrey (2007))
Brain WM	1×10^{-13}	Shahim et al. (2010)
Brain GM	1×10^{-15}	
Brain WM	1×10^{-15}	Cheng and Bilston (2007)

through the ECS of the cord tissue. As ECF and CSF are able to communicate via the PVS (Brinker et al., 2014; Sakka et al., 2011) they are thought to be similar in composition and therefore have similar material properties such as density and dynamic viscosity. Dynamic viscosity μ is a measure of a fluid's internal resistance to flow; in a poroelastic model this affects how easily fluid can move through the pores. As the properties of CSF are more readily available, these have been used to describe ECF in the model.

CSF is a clear fluid consisting mainly of water but containing small amounts of oxygen, glucose, proteins and cells (Tortora and Derrickson, 2014). In certain circumstances (blood-brain barrier damage, trauma or infection) large particles such as blood cells and proteins could enter the CSF and potentially increase viscosity. However, viscosity measurements on artificial CSF with increased levels of large proteins did not show a significant viscosity increase (Bloomfield et al., 1998). As such it is a reasonable assumption to model CSF and therefore ECF with the properties of water at 37 °C (body temperature), that is dynamic viscosity $0.0007\,\mathrm{Pa\,s}$ and density $1000\,\mathrm{kg\,m^{-3}}$.

3.4 Pia mater

The pia mater provides structural support to the fragile spinal cord tissue (Elliott et al., 2013) and from a modelling perspective it has been shown to affect pressure gradients within the spinal cord (Støverud et al., 2016a). The pia mater is a thin (~15 µm) protective layer adhered to the entire surface of the brain and spinal cord (Reina et al., 2004).

Only one apparent study has tested YM of pia mater directly (Ozawa et al., 2004), yielding a value of 2300 kPa. Elasticity of whole cord sections including the pia mater have produced YM values ranging from 520 to 1880 kPa (Bilston and Thibault, 1996; Mazuchowski and Thibault, 2003) although the contribution of the pia mater is uncertain. PR of the pia mater has not been measured and in existing poroelastic models a value of 0.35 (Bertram and Heil, 2017; Heil and Bertram, 2016) or 0.479 (Støverud et al., 2016a) has been assigned.

Porosity and permeability of the pia mater has not been directly measured and values used in existing models range from $1 \times 10^{-15}\,\mathrm{m}^2$ to $3 \times 10^{-13}\,\mathrm{m}^2$ (Bertram and Heil, 2017; Heil and Bertram, 2016; Støverud et al., 2016a). Elliott (2012) calculated pia mater permeability by averaging the number of PVS in a particular region, as this is one verified fluid pathway across the pia mater (Stoodley et al., 1996), and found it to be $3.1 \times 10^{-15}\,\mathrm{m}^2$.

3.5 Oedema

Tissue oedema is often associated with syringomyelia (Fischbein et al., 2000). Despite this, no work has been undertaken to quantify the mechanical contribution of oedema to syringomyelia cavity formation. In the present model, the elastic parameters of the oedema region solid skeleton are the same as the surrounding white matter tissue. There are several kinds of CNS oedema although one kind, known as interstitial oedema, is most commonly found alongside syringomyelia (Weller, 2014). Spinal cord interstitial oedema is characterised by increased fluid content in the ECS of the cord (Naruse et al., 2000); for modelling purposes the increased fluid content results in an increased porosity and permeability of the oedematous tissue.

Porosity values for healthy CNS tissue are ∼0.2 (Nicholson and Syková, 1998); although porosity measurements of oedematous tissue are uncommon, the increased porosity is thought to be in the region of 0.3 to 0.35 (Sarntinoranont et al., 2003; Sykova et al., 1994). In the simulations oedema porosity is assumed to be $\phi = 0.3$. The permeability of oedema is a function of its porosity, the equations used to calculate oedema permeability are described in Chapter 4.

3.6 Cerebrospinal fluid pressure

The forces applied to the poroelastic spinal cord model described in Chapter 2, Section 2.3 originate from pressure changes in the CSF surrounding the spinal cord. CSF pressures are not calculated in the present model therefore an indication of both healthy and abnormal CSF pressure values are required to accurately load the model.

The main driving force behind CSF pressure changes are normal processes such as cardiac pulse, breathing, coughing, physical activity or posture (Dreha-Kulaczewski et al., 2015; Sakka et al., 2011; Williams, 1976). CSF pressure changes in the spinal SAS have been measured invasively using pressure probes and have been calculated using CFD models. An indication of the measured and calculated pressures can be seen in Table 3.4, where there is a clear distinction between healthy and patient values. Here the mean baseline CSF pressure is given along with the amplitude of cardiac and cough pressures.

In the present poroelastic model, the CSF pressure applied to the outside of the cord is approximated using a sinusoidal wave. A zero initial condition is assumed, therefore the mean baseline pressures (Column 1, Table 3.4) can be disregarded and only the cough or pulse amplitudes are needed. Pressure values from invasive pressure measurements rather than calculated CFD values were chosen to load the model as these measurements were made *in vivo*. Due to the zero initial condition the chosen pulse amplitudes for healthy (~200 Pa) and disturbed (~350 Pa) CSF flow are used in the poroelastic model as relative rather than absolute pressures.

Table 3.4: CSF pressure in the human cervical spinal SAS, all units are Pa. The mean baseline pressure is given, pulse and cough amplitude (amp.) are relative to the mean pressures. CM - Chiari malformation, SM - syringomyelia, CFD - computational fluid dynamics study, INV - invasive pressure measurement.

Mean pressure	**Pulse amp.**	**Cough amp.**	**Subject**	**Type**	**Reference**
~1200	~700	-	healthy, CM	CFD	Rutkowska et al. (2012)
-	26	-	healthy	CFD	Clarke et al. (2013)
-	56.6	-	CM no SM		
1500	213	~5300	healthy	INV	Heiss et al. (1999)
2070	310	~5300	CM, SM		
1500	213	~5900	healthy	INV	Heiss et al. (2012)
~1600	360	3640	SM		

3.7 Summary

In this Chapter the parameters required for the poroelastic model have been described, with a focus on how they relate to spinal cord tissue. Where available, a review of spinal cord tissue properties in the literature has been given and parameter choices for the model have been made and justified. These tissue property choices will be used to improve the spinal cord model described in Chapter 2.

Compared to elastic properties such as Young's modulus, spinal cord porosity and permeability data is much less common. Existing techniques that have been used to obtain porosity and permeability values suitable for use in a poroelastic model of the cord have been outlined, but there is still an apparent scarcity of suitable measurement techniques and therefore values. There are two main reasons for this. Firstly, there are the inherent difficulties surrounding the mechanical testing of *in vivo* tissue. Secondly, many of the methods traditionally used to measure or calculate porosity and permeability were designed around stiffer materials such as rocks or soils. As poroelastic models of CNS tissue are becoming a more popular method of studying diseases such as hydrocephalus and syringomyelia there is a need for suitable techniques to obtain brain and spinal cord porosity and permeability.

Chapter 4

Porosity and permeability derivation

Introduction

Information regarding spinal cord porosity and permeability is scarce. Although diffusion coefficients have been obtained for spinal cord tissue, there is evidence that in pathological conditions, such as oedema, bulk flow can occur and a pressure difference between healthy and oedemous tissue has been observed (Reulen, 2010). Consequently there is a need to obtain spinal cord bulk flow parameters (such as permeability) for the study of conditions such as syringomyelia, which is thought to be preceded by oedema (Fischbein et al., 2000).

Diffusion tensor imaging (DTI) is a DW-MRI technique and has been used to detect how spinal cord fibre orientation affects permeability anisotropy (Sarntinoranont et al., 2006); however, the magnitude of spinal cord permeability in this study was taken from the literature. The magnitude of brain tissue permeability has been addressed by Shahim et al. (2010).

Neurite orientation and dispersion density imaging (NODDI) is another DW-MRI technique that gives more detailed microstructural information regarding CNS tissues and has been used to image the spinal cord (Grussu et al., 2015; Zhang et al., 2012). The following Chapter presents a technique for deriving spinal cord porosity and permeability values using the microstructural information revealed by NODDI analysis. Section 4.1 provides background on DW-MRI. Details of the DW-MRI data acquisition along with the calculations used to derive porosity and permeability values are given in Sections 4.2 and 4.3. Finally the preliminary findings and an evaluation of the proposed technique are given in Sections 4.4 and 4.5.

The premise of the proposed technique is to calculate spinal cord permeability and porosity based on the microstructural information revealed by neurite orientation and dispersion density imaging (NODDI). The aim is to provide practical permeability tensors and porosity values for the model being built and to provide the foundation of a technique for non-invasive characterisation of spinal cord porosity and permeability. Whilst not a direct measurement technique, the non-invasive nature of the presented method is advantageous as *in vivo* human spinal cord porosity and permeability can be acquired. This work is an expansion of ideas presented in Venton et al. (2017).

4.1 Diffusion MRI

Magnetic resonance imaging (MRI) uses a strong magnetic field to align protons found in water molecules. Water molecules contain hydrogen nuclei (protons) which have a property named spin. The application of a magnetic field causes the proton spins to align; once in this state they can be manipulated using radiofrequency (RF) energy causing them to release energy (Roth, 2012). It is this released energy signal that is detected by the MRI scanner to generate images of the body. MRI scan sequences must balance the application of magnetic field gradients with RF pulses to obtain good images.

Biological tissues have a large water content and random molecular motion (also known as Brownian motion) transports water molecules within tissues; this process is known as diffusion. In the timescales of a typical MRI scanner, free water molecules can diffuse a distance of $\sim 10\,\mu\text{m}$ (Le Bihan, 2011). With the ability to detect diffusion on these distances the microstructure of tissue can be quantified (Le Bihan, 2011).

When MRI is designed to be sensitive to this diffusion, it is known as diffusion weighted magnetic resonance imaging (DW-MRI). Sensitivity to diffusion in tissue is acquired by applying consecutive RF pulses in opposite directions (known as spin echo), where the time between the pulses is where molecules are allowed to diffuse (Le Bihan, 2011). The signal detected by the scanner attenuates between the two RF pulses, depending on the amount of diffusion that occurs. In free water the difference between the images acquired at each RF pulse would be negligible, as diffusion is the same in all directions (Basser and Özarslan, 2014). However, the presence of tissue microstructural features such as cells obstructs free diffusion in tissue resulting in a diffusion attenuated signal (Basser and Özarslan, 2014). This difference is used to quantify diffusion and give an indication of tissue microstructure.

Application of a constant magnetic gradient in the presence of RF pulses impairs the image quality, to counteract this the magnetic gradient is also pulsed (Le Bihan, 2011). This technique is known as pulsed gradient spin echo (PGSE) and is commonly used for DW-MRI. DW-MRI is particularly susceptible to motion artifact due to patient movement in the scanner. Echo planar imaging (EPI) involves reducing the RF spin echo to a single acquisition period which reduces almost all motion artifact (Le Bihan, 2011). The amount of diffusion weighting in an image is affected by both magnetic gradient and RF pulses and is indicated by the b-value. For example a non diffusion weighted MRI has a b-value of $b = 0$.

Diffusion causes the signal to attenuate between RF pulses; this is affected by the amount of diffusion weighting in the scan sequence and is given by

$$S_A = \exp(-b\mathrm{D})$$

where S_A is the signal attenuation, b is the b-value and D is the diffusion coefficient. The diffusion coefficient describes the distance molecules can travel in a given time. Free water, cells and other tissue features will each have a different diffusion coefficient as the water contents and structures differ. Although diffusion is isotropic in free water, the presence of tissue microstructural features hinders diffusion when gradients are applied in different directions through the tissue (Le Bihan, 2011).

Acquired scan data can be interpreted using a number of different analysis techniques. DTI is an MRI technique that exploits the directional differences and reveals microstructural information as well as diffusion coefficients of tissue (Le Bihan, 2011). DTI is less reliable when high b-values are used and high angular-resolution imaging (HARDI) refers to a set of imaging and analysis techniques developed for high b-value imaging with multiple gradients (Basser and Özarslan, 2011; Jones, 2011).

For deriving permeability and porosity of spinal cord tissue, DW-MRI data analysed using a DW-MRI technique called neurite orientation dispersion and density imaging (NODDI) has been used. Details of NODDI analysis and permeability and porosity derivation are now described.

4.2 Data acquisition and NODDI analysis

DW-MRI data acquired from the cervical spinal cords of four healthy subjects were used where all subjects (median age 34) had provided informed written consent. The data was originally acquired for the study carried out by Grussu et al. (2015) and is used here with permission.

4.2.1 Neurite Orientation Dispersion and Density Imaging (NODDI)

NODDI is a popular DW-MRI technique developed by Zhang et al. (2011) to obtain information regarding the microstructure of CNS tissue. The technique is based on combining a three-compartment tissue model (see Figure 4.1), with a multi-shell HARDI protocol. The HARDI protocol takes images at several angles through the tissue, allowing different fibre orientations to be detected.

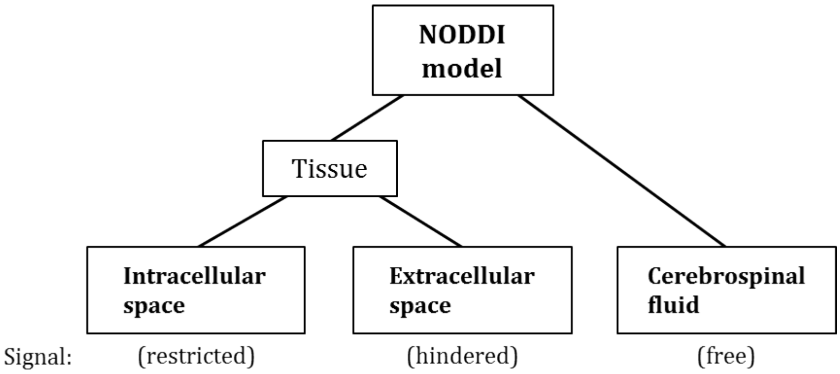

Figure 4.1: NODDI 3-compartment tissue model.

The NODDI model differentiates between different tissue compartments and calculates the volume fraction of each compartment in each three dimensional region (voxel) of the spinal cord scan data. The DW-MRI signal from the three compartments within each image voxel is modelled using the following equation (Zhang et al., 2012)

$$S = S_0\Big(\nu_{iso}S_{iso} + (1-\nu_{iso})\Big(\nu_{in}S_{in} + (1-\nu_{in})S_{en}\Big)\Big) . \tag{4.1}$$

Here S is the full normalised signal, S_0 is the non diffusion weighted signal, and S_{in}, S_{en}, and S_{iso} are the normalised signals for intracellular, extracellular and CSF compartments respectively. NODDI analysis estimates the intracellular ν_{in} and CSF volume fractions ν_{iso}.

Use of a HARDI protocol allows the mean orientation $\boldsymbol{\mu}$ of tissue fibres (largely axons and dendrites) to be calculated. NODDI also provides the orientation dispersion index $\textit{odi}$, which indicates the spread of fibres around $\boldsymbol{\mu}$. $\textit{odi}$ values range from 0 to 1 where 0 indicates strictly parallel fibres (no dispersion) and 1 indicates randomly ordered fibres (maximum dispersion) (Grussu et al., 2015).

This information is used in the permeability calculations.

4.2.2 Imaging and data analysis

NODDI diffusion data from the cervical spinal cords of four healthy subjects acquired for Grussu et al. (2015) were used. Full details of the imaging protocol and post processing are explained in Grussu et al. (2015). The scans were acquired using a 3T Philips Achieva scanner using a 16-channel neurovascular receive-only RF coil. Two HARDI shells were used, $b = 711$ and $2855\,\mathrm{s/mm^2}$ with 30 and 60 non-collinear directions, respectively. Three non-diffusion weighted images ($b = 0$) were acquired with each shell resulting in a total of 6 non-diffusion weighted images. Data were acquired with a voxel size of $5\,\mathrm{mm}^3$ ($1{\times}1{\times}5\,\mathrm{mm}$) and twelve image slices were collected for each subject (see Figure 4.2).

The images were analysed using the NODDI Matlab toolbox to generate parameter maps (of $\boldsymbol{\mu}$, ν and $\textsc{odi}$) for each subject. This microstructural information was used to determine tissue porosity and permeability.

4.3 Porosity and permeability calculations

In a poroelastic spinal cord tissue model, the poroelastic parameters porosity and permeability are required. As tissue is a complex material, the definitions of solid skeleton and pore fluid used in Section 3.1 have been used. Firstly, the solid skeleton is assumed to consist of large tissue components such as axons, dendrites and cell bodies. Secondly, the pore fluid region described by porosity is assumed to consist predominantly of ECF.

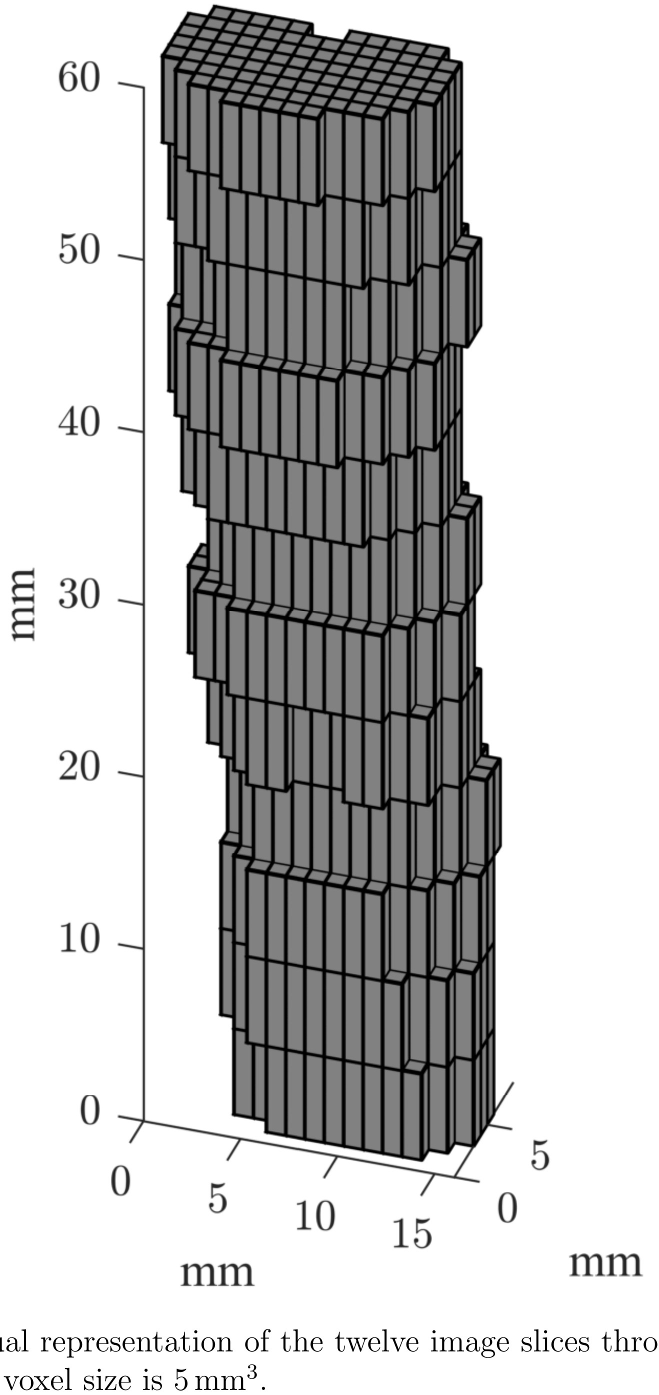

Figure 4.2: Visual representation of the twelve image slices through the cervical spinal cord, the voxel size is $5\,\mathrm{mm}^3$.

4.3.1 Deriving porosity

The NODDI volume fractions in Equation (4.1) represent the following tissue compartments (Grussu et al., 2015):

ν_{iso} -	free moving CSF such as that found in the central canal or subarachnoid space.
ν_{in} -	tissue fibres, such as axons or dendrites.
ν_{en} -	the remaining space, occupied by ECF, glial cells and neuron cell bodies

With the assumption that porosity ϕ in spinal cord tissue is the region containing ECF, the NODDI parameter ν_{en} is a reasonable approximation for ϕ, that is

$$\phi \approx \nu_{en} = 1 - \nu_{in} \tag{4.2}$$

Larger fluid regions described by ν_{iso} do not contribute to the poroelastic solid skeleton or porosity ϕ.

4.3.2 Deriving permeability

Intrinsic permeability κ has units of m^2 and is often presented as a tensor

$$\boldsymbol{\kappa} = \begin{pmatrix} \kappa_{xx} & \kappa_{xy} & \kappa_{xz} \\ \kappa_{yx} & \kappa_{yy} & \kappa_{yz} \\ \kappa_{zx} & \kappa_{zy} & \kappa_{zz} \end{pmatrix} . \tag{4.3}$$

Coefficients κ_{xx}, κ_{yy} and κ_{zz} represent the magnitude of permeability in the x, y and z directions respectively and $\kappa_{yx} = \kappa_{xy}$, $\kappa_{zx} = \kappa_{xz}$ and $\kappa_{zy} = \kappa_{yz}$ account for the dependence of flow on pressure gradients in orthogonal directions. For an isotropic material, where $\kappa_{xx} = \kappa_{yy} = \kappa_{zz} = \kappa$ and all remaining coefficients are zero, Equation (4.3) reduces to

$$\boldsymbol{\kappa} = \kappa \boldsymbol{I}$$

where $\boldsymbol{I}$ is the identity matrix. Directional information such as whether the material is isotropic or anisotropic, as well as values of the κ coefficients are needed to construct a permeability tensor for spinal cord tissue.

Permeability tensor coefficients

Both grey and white matter are often considered to be fibrous materials for modelling purposes. Each has a different fibre layout that is captured by the NODDI parameter $\textsc{odi}$ (Figure 4.3), which shows a marked difference between grey matter (red regions) and white matter (blue regions).

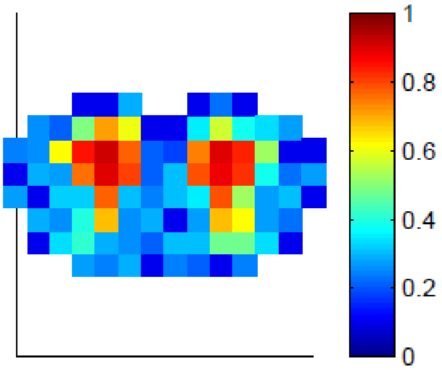

Figure 4.3: Orientation dispersion index ($\textsc{odi}$) values, $\textsc{odi}$ values near 1 indicate high dispersion.

To calculate values for the permeability tensors, a threshold $\textsc{odi}$ value of 0.3 is used to differentiate between grey and white matter regions. At present there is not a known $\textsc{odi}$ threshold between grey and white matter, as such the threshold $\textsc{odi} = 0.3$ was chosen manually as it showed the clearest separation of grey and white matter regions (Figure 4.5). An $\textsc{odi} \leq 0.3$ indicates low fibre dispersion, so the ordered axon tracts commonly found in white matter are treated as parallel fibres with anisotropic permeability. Grey matter regions have higher fibre dispersion ODI > 0.3 and as such grey matter is treated as a fibrous material with isotropic permeability.

For white matter, permeability perpendicular to parallel fibres is calculated using an analytical solution derived by Gebart (1992)

$$\kappa_{WMpe} = \frac{16}{9\pi\sqrt{6}}\left(\sqrt{\frac{1-\phi_{\min}}{1-\phi}}-1\right)^{5/2} a_{wm}^2 \tag{4.4}$$

where ϕ is the porosity (as calculated with Equation 4.2), ϕ_{min} is the minimum porosity required to permit fluid movement and a_{wm} is the white matter fibre radius. Assuming white matter axons are hexagonally packed ϕ_{min} is given by

$$\phi_{\min} = 1 - \pi/(2\sqrt{3}) \approx 0.0931\,.$$

Permeability along parallel fibres (Gebart, 1992) is calculated using

$$\kappa_{WMpa} = \frac{8a_{wm}^2}{53}\frac{(\phi)^3}{(1-\phi)^2}\,. \tag{4.5}$$

Grey matter isotropic permeability is calculated using an adapted version of Equation (4.4), adapted by Nabovati et al. (2009) for isotropic fibrous materials

$$\kappa_{GM} = C_1\left(\sqrt{\frac{1-\phi_{\min}}{1-\phi}}-1\right)^{C_2} a_{gm}^2 \tag{4.6}$$

where the constants $C_1 = 0.491$, $C_2 = 2.31$ and $\phi_{\min} = 0.0743$ were determined by fitting numerical results to Equation (4.6) and a_{gm} is the grey matter fibre radius.

Permeability tensor generation

The mean orientation vector $\boldsymbol{\mu} = (x, y, z)$ gives the mean direction of fibres in a voxel. In grey matter regions, the permeability tensor will be in the form

$$\boldsymbol{\kappa} = \kappa_{GM}\boldsymbol{I}$$

where κ_{GM} is given by equation (4.6). For white matter, the permeability tensor coefficients calculated using Equations (4.4) and (4.5) will be perpendicular and parallel to $\boldsymbol{\mu}$ respectively and the tensor will have the form

$$\boldsymbol{\kappa} = \begin{pmatrix} \kappa_{WMpe} & 0 & 0 \\ 0 & \kappa_{WMpe} & 0 \\ 0 & 0 & \kappa_{WMpa} \end{pmatrix}.$$

For the plane strain poroelastic model described in Chapter 2, the permeability tensor is two dimensional

$$\boldsymbol{\kappa} = \begin{pmatrix} \kappa_{WMpe} & 0 \\ 0 & \kappa_{WMpe} \end{pmatrix}.$$

To calculate permeability tensor coefficients, grey and white matter fibre radii a_{gm} and a_{wm} are required. White matter axons have a radius of $a_{wm} \approx 2\,\mu\text{m}$ (Duval et al., 2015), although values from 0.5–7.5 µm (Assaf et al., 2008; Duval et al., 2015; Komlosh et al., 2013; Xu et al., 2014; Zhang et al., 2011) have been reported. Grey matter fibre radius is less well recorded but as dendrite radius is thought to be in the region of 0.1–1.5 µm (Fiala et al., 2008), a nominal value of $a_{gm} \approx 0.8\,\mu\text{m}$ has been used here for grey matter permeability calculations.

Equations (4.4) and (4.6) both specify a minimum porosity below which no permeating flow will occur (0.0931 and 0.0743 respectively). Voxels with zero permeability were excluded from the analysis, as were voxels with $\nu_{in} = 0$. Only voxels with $\nu_{iso} < 0.05$ were included in the analysis. This is in agreement with the NODDI hypothesis that ν_{iso} should be small in regions with minimal CSF (Grussu et al., 2015) as high ν_{iso} values can indicate results in that particular voxel are less reliable.

4.4 Spinal cord porosity and permeability results

4.4.1 Porosity

The mean porosity of cervical spinal cord tissue across all subjects was 0.396 and 0.456 for white and grey matter respectively. A comparison of the mean porosities for each subject can be seen in Figure 4.4. Excluding voxels with high CSF contamination ($\nu_{iso} \geq 0.05$) resulted in higher porosity for white matter (0.451) whereas grey matter did not change significantly (0.47).

4.4.2 Permeability

Figure 4.5 shows which regions of the spinal cord cross section were allocated as having either parallel or randomly oriented fibres based on the threshold ODI value of 0.3. Although not always clear, grey and white matter regions are largely differentiated using this threshold.

Mean permeability values calculated for each subject can be seen in Table 4.1. Permeability parallel to white matter fibres was an order of magnitude higher

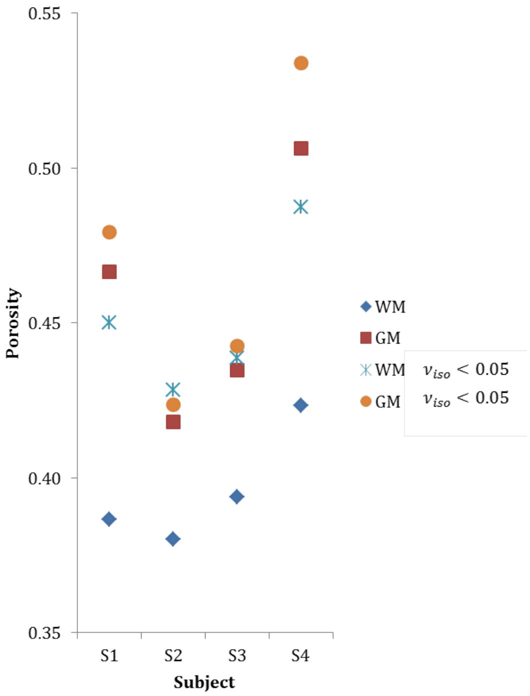

Figure 4.4: Mean porosity values for each subject. White and grey matter porosity values (WM and GM) are compared to porosity values when voxels with $\nu_{iso} \geq 0.05$ are excluded.

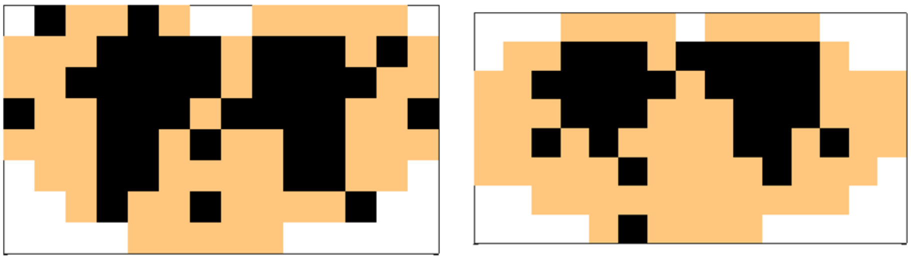

(a) Subject 1

(b) Subject 2

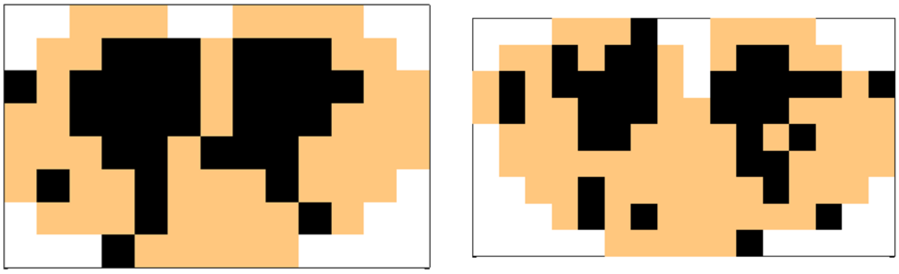

(c) Subject 3

(d) Subject 4

Figure 4.5: Grey matter (black) and white matter (orange) fibre regions, allocated based on the assumption that white matter fibres have ODI ≤ 0.3.

than grey matter permeability. Due to the similarity of the equations used, permeability perpendicular to white matter fibres was of the same order of magnitude as grey matter permeability.

Table 4.1: Permeability means for the four subjects, all units are in µm^2 for clarity
($1\,\mu\mathrm{m}^2 = 1 \times 10^{-12}\,\mathrm{m}^2$).

Subject	**WM (κ_{WMpa})**	**WM (κ_{WMpe})**	**GM (κ_{GM})**
Subject 1	0.296	0.062	0.032
Subject 2	0.344	0.070	0.026
Subject 3	0.219	0.047	0.022
Subject 4	0.423	0.086	0.053
Mean	0.321	0.066	0.033

Lower permeability in grey matter was largely due to the fact that the grey matter fibre radius a_{gm} was smaller than white matter fibre radius a_{wm}. An indication of how fibre radius affects permeability can be seen in Figure 4.6. With a higher fibre radius κ_{GM} increases whilst κ_{WMpe} remains low. When the grey and white matter fibre radii are assumed to be the same, κ_{GM} is higher than κ_{WMpe}. See Figure 4.7 for a comparison of calculated permeabilities when grey matter is calculated with both $a_{gm} = 0.8\,\mu\mathrm{m}$ and $a_{gm} = 2\,\mu\mathrm{m}$.

4.5 Evaluation of the method

4.5.1 Porosity

In the literature, the range of brain tissue porosity is stated as $0.15 < \phi < 0.3$ (Syková and Nicholson, 2008). Spinal cord tissue is often assumed to be similar for modelling purposes and a value of ~0.2 is used (as in (Harris and Hardwidge, 2010; Sarntinoranont et al., 2006)). This is lower than mean values for porosity

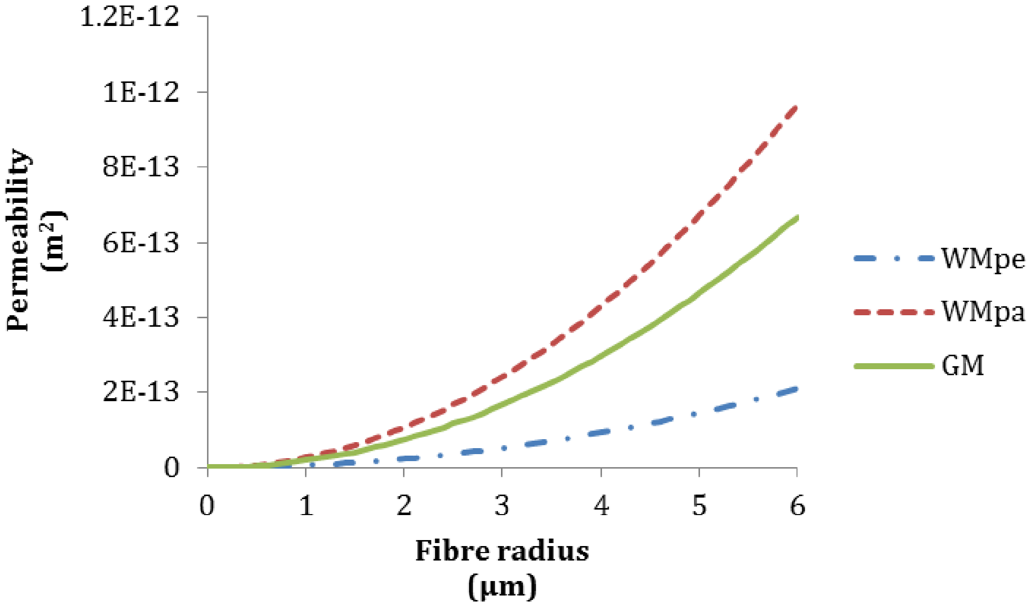

Figure 4.6: Relationship between fibre radius and calculated permeability. Values are shown for grey matter (GM), perpendicular to white matter fibres (WMpe) and parallel to white matter fibres (WMpa). A fixed porosity of $\phi = 0.4$ was used.

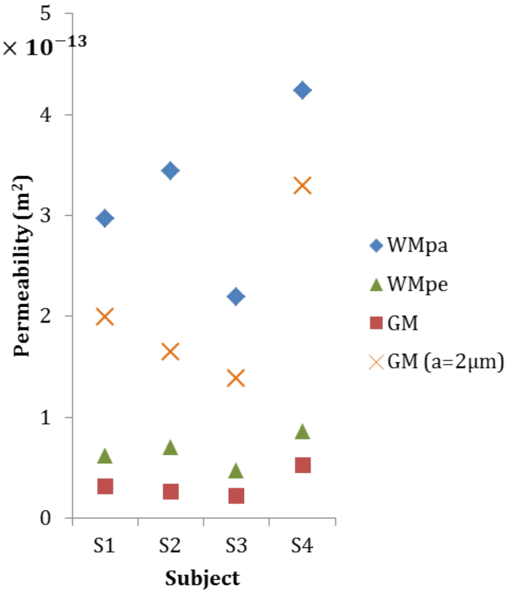

Figure 4.7: Mean subject permeabilities for κ_{WMpe} (WMpe), κ_{WMpa} (WMpa) and κ_{GM} (GM). White matter permeability calculated using $a_{wm} = 2\,\mu\text{m}$, grey matter shown for both $a_{gm} = 0.8\,\mu\text{m}$ and $a_{gm} = 2\,\mu\text{m}$ for comparison.

found here, which were 0.396 and 0.456 for white and grey matter respectively. The likely explanation is that NODDI volume fraction ν_{in} only includes fibre-like parts of tissue. Features such as neuron cell bodies and glial cells are excluded from ν_{in} and their volume instead contributes to the extracellular volume fraction ν_{en}, along with ECF, which is used for porosity. High porosity values (~0.4) for CNS tissues have been reported, although this is in subjects with pathological conditions or neonatal brain tissue (see Syková and Nicholson (2008)). Despite this, the finding that grey matter has a higher porosity has been observed in other studies (Kessler et al., 1976).

Reasons for the overestimation of porosity are varied. There is more non-fibrous material in grey matter (Bilston, 2016) hence grey matter porosity could be overestimated. Furthermore, myelin is invisible to DW-MRI (Stikov et al., 2015) and would be included in the white matter volume fraction increasing this value further. In addition if blood vessels are small enough to be excluded from the ν_{iso} signal, they would likely also contribute to the extracellular volume fraction ν_{en} as they are unlikely be included in the intracellular region. The precise volume of cell bodies, glial cells and myelin in spinal cord grey and white matter has not been determined, therefore their contribution to ν_{en} is uncertain.

The definition of porosity in Equation 4.2 excludes fluid regions described by ν_{iso}. This is justified as it is ECF, not CSF that porosity refers to. However, large diameter axons (~15 µm) could contribute to ν_{iso} (Grussu et al., 2015), resulting in a smaller ν_{in} volume fraction. When only voxels with $\nu_{iso} < 0.05$ were included, the porosity of both grey and white matter was similar, reflecting the fact that white matter is more susceptible to partial volume effect from the CSF that surrounds the spinal cord.

Overall, whilst the present method of calculating porosity values using NODDI data can detect regional porosity differences, there is much scope for improvement.

The calculated value is often overestimated for the reasons stated above. However, certain factors that contribute to this overestimation could be compensated in future iterations of the technique. For example, knowing the volumes of myelin and glia that are being included in the ν_{en} value would allow a compensation technique to be developed to overcome this.

4.5.2 Permeability

Intersubject means for subjects 1-3 were similar (Figure 4.7) whereas subject 4 permeability values were higher. The range of values (not shown) for each individual subject spanned several orders of magnitude. To date there has been little experimental work to determine spinal cord permeability values at different spinal levels or regions, so whether this large range of values accurately represents spinal cord permeability is uncertain. Existing work that has treated grey and white matter separately has assigned grey matter as less permeable (for example Sarntinoranont et al. (2006)) rather than measuring it. Shahim et al. (2010) used DTI to examine brain tissue permeability and found the same pattern of less permeable grey matter, slightly more permeable white matter perpendicular to the fibres and higher permeability along white matter fibres.

Values were calculated based on how easily fluid could move through the tissue space defined by ν_{en}. However, this space contains glial cells and other extracellular material which could hinder fluid movement. As such, the permeability values found can be considered an upper limit of permeability - the true value is likely to be less. Similarly, equations (4.4) to (4.6) assume rigid fibres which is not the case in cord tissue. Again this implies the permeability calculated serves as an upper limit as fluid movement in the ECS may be hindered by softer fibres. Furthermore permeability was calculated using porosity which as mentioned previously is higher than expected, this would also cause permeability values to be higher particularly in grey matter.

Equations (4.4) and (4.6) define a minimum porosity required for permeating flow to occur ($\phi = 0.0931$ and $\phi = 0.0743$ respectively). Furthermore, experimental validation of Equations (4.4) and (4.6) demonstrated that results for $\phi \leq 0.1$ and $\phi \geq 0.98$ may be unreliable (Gebart, 1992; Nabovati et al., 2009). When permeability values calculated with $0.1 < \phi < 0.98$ were excluded this had a minimal effect on the mean permeability for each subject (~1 % increase).

Fibre radius significantly affected the permeability value. The axon and dendrite radii used here for white and grey matter are as representative as possible (Duval et al., 2015; Fiala et al., 2008). However as shown in Figure 4.6, when a fibre radius of 2 µm rather than 0.8 µm was used for grey matter, the mean grey matter permeability was higher than perpendicular white matter permeability. Similarly, when a single value of ϕ was used white matter perpendicular permeability was lower than both parallel white matter and grey matter permeability (not shown).

4.5.3 Assumptions

The assumption that ϕ does not include fluid within cells is appropriate when fluid movement across the cell boundary is disregarded. In models of CNS tissues where the forces acting on the tissue are of short duration such as pulse, cough or trauma this assumption is appropriate and hence the permeability tensors derived here are appropriate. Noise in the scan data has been found to give non zero *ODI* values even for completely parallel fibres (Zhang et al., 2011). As such the higher assumed threshold value (0.3) between parallel and random fibres is reasonable. In addition the existence of crossing fibres in white matter indicate that it does not have strictly parallel fibres (Bilston, 2016), in which case a higher threshold such as $\textsc{odi} = 0.3$ captures this better.

4.5.4 Interpretation

Spinal cord and brain tissue permeability values in the literature were listed in Chapter 3, Table 3.3. Where grey and white matter permeability were measured separately grey matter was less permeable than white, which supports present results for κ_{WMpa} and κ_{GM}. Calculated permeability values here are larger than most existing values, likely because the porosity was overestimated.

Figure 4.6 showed how fibre radius affected the calculated permeability values. Wong et al. (2012) found higher radial diffusion in grey matter than in white matter which is in agreement with the values found here. In the literature, grey matter is sometimes modelled as less permeable than white matter (such as in (Kaczmarek et al., 1997; Sarntinoranont et al., 2006)) although this stems from an earlier study by Reulen et al. (1977) which did not address the difference between permeability parallel to and perpendicular to white matter axons. The present work suggests that differing fibre radius could cause the difference in grey and white matter permeability.

A DTI study by Yoon et al. (2016) found that white matter had a lower diffusivity. They noted that two DTI parameters used to diagnose oedema are more prominent in the grey matter than in the white matter. This suggests that porosity is slightly higher in grey matter, a result echoed using the present technique. The results presented in Section 4.4 also demonstrate that the microstructural information provided by NODDI provides a basis for obtaining the permeability of the spinal cord. The calculated permeability coefficients are reasonable when compared to existing values, although results from DW-MRI studies (Section 4.4, Shahim et al. (2010) and Venton et al. (2017)) are consistently higher than values found using other techniques. The data shown here demonstrates that this method will differentiate regions of the spinal cord that have different porosity and permeability.

4.5.4.1 Improving the method

There are several ways in which this technique for deriving spinal cord permeability and porosity can be improved. The porosity was overestimated and a way of compensating for the inclusion of cell bodies, glial cells and myelin in the porosity value would be beneficial. Further research to determine the average radius of fibres and the layout of fibres particularly in grey matter would answer how accurately equations (4.4), (4.5) and (4.6) calculate permeability of the cord. The equations relate to randomly oriented or strictly parallel fibre layouts which are not wholly representative of spinal cord microstructure. Ideally a range of values for the constants in Equation (4.6) would be available, each set relating to a different ODI , that is a different fibre spread and hence permeability.

Tortuosity is a dimensionless number that summarises the extent to which fluid movement in a permeable material is hindered by the shape of the pore space (Nicholson and Syková, 1998). It is neglected in the present work but if included would likely result in lower permeability values as the grey and white matter are complex materials. Furthermore in the present work all fibres in grey and white matter were assumed to be cylindrical, which is not always the case. However, at porosities nearer expected spinal cord porosity ($\phi \approx 0.2$) this would be less of an issue due to the effects of overlapping fibres.

At present, the white matter permeability tensors are parallel to the spinal cord whereas in reality the mean fibre direction deviated slightly from this. Incorporation of this directional information would be beneficial in three dimensional models of fluid transport within the spinal cord. Another benefit of using DW-MRI is the high resolution (compared to other methods) of data provided, which can be used to identify parameter differences between anatomical regions. Future work to compare permeabilities of more detailed regions such as the dorsal and ventral horn would be useful for mathematical spinal cord models.

4.6 Summary

The foundation of a technique for deriving spinal cord porosity and permeability values from DW-MRI data has been presented. Initial results based on existing DW-MRI data showed that for a plane strain model, grey matter is slightly less permeable than white matter, although these were based on slightly overestimated porosity values. These results are used to improve the poroelastic spinal cord model presented in Chapter 2. The improved model is used to investigate the formation of syringomyelia cavities within spinal cord tissue.

Chapter 5

Simulations

Introduction

The key aim of these simulations is to examine stresses in the spinal cord tissue when it is subjected to external CSF pressures. Including representative tissue properties and CSF pressure values indicates whether the spinal cord could sustain damage through purely mechanical means. Almost all current syringomyelia research accepts that mechanical means play a role in cavity formation. Whether this is the sole cause, or is combined with biological effects, is still under investigation.

Oedema in the spinal cord has been linked to syringomyelia (Fischbein et al., 2000). Recent research has explored possible links between syringomyelia, oedema and the presence of the water transport protein AQP4 (Hemley et al., 2012). However, an examination of the mechanical role of oedema in cavity formation has not been carried out. The need for further investigation into how oedema could lead to syringomyelia has previously been highlighted (Elliott et al., 2013).

To date no plane strain poroelastic models of the spinal cord cross section (as in Chapter 1, Figure 1.4) have been used to investigate syringomyelia. This allows a detailed analysis of the effect of increased CSF loading, a region of oedema, grey matter with different properties and NRDL tethering on cavity formation to be undertaken. This is beneficial in identifying the salient features of a mechanical syringomyelia model.

Section 5.1 gives details of the simulation set up and results post-processing. Section 5.2 presents results of simulations. This examines the effects of anatomical features in a two dimensional model of the spinal cord cross section, the presence of oedema and impact of increased CSF loading. A sensitivity analysis of the parameters used in the model is given in Section 5.3. Finally, an outline of the main themes and novel contribution is given in Section 5.4.

5.1 Simulation setup

5.1.1 Model parameter summary

Parameters used in the model were taken from the literature (see Chapter 3) or calculated using diffusion magnetic resonance imaging (DMRI) data (see Chapter 4). A summary of parameters used in the simulations can be seen in Table 5.1.

Table 5.1: Baseline parameters for white matter, grey matter, the pia mater and ECF. * indicates parameters for an oedema region located in the spinal cord white matter. Parameter units are given in brackets, where omitted the parameter is dimensionless.

		White matter	Grey matter	Pia mater	Oedema*	ECF
Young's modulus (Pa)	E	5000	10 000	100 000	5000	-
Poisson's ratio	ν	0.4	0.4	0.479	0.4	-
Density ($\mathrm{kg\,m^{-3}}$)	ρ	1050	1050	1050	1050	1000
Biot-Willis coeff.	α	0.9995	0.9995	0.9995	0.9995	-
Porosity	ϕ	0.2	0.25	0.2	0.3	-
Permeability ($\mathrm{m^2}$)	κ	6.6×10^{-14}	3.3×10^{-14}	3.1×10^{-15}	1.3×10^{-13}	-
Dynamic viscosity (Pa·s)	μ	-	-	-	-	7×10^{-4}

5.1.2 Programme checking

To verify the poroelastic model, output was compared with results from a static analytical solution and a fully coupled finite difference model. Details of the static analytical solution can be found in Appendix B. For a static problem the finite element system reduces to

$$\begin{pmatrix} K & -Q \\ 0 & H \end{pmatrix} \begin{bmatrix} \boldsymbol{u} \\ \boldsymbol{p} \end{bmatrix} = \begin{bmatrix} \boldsymbol{F}_s \\ \boldsymbol{F}_f \end{bmatrix} \tag{5.1}$$

where solid displacements $\boldsymbol{u}$ and pore pressure $\boldsymbol{p}$ are linked according to the coupling matrix Q. Definitions of the finite element matrices are given in Chapter 2.

The fully coupled poroelastic finite element model was checked on an annulus shaped mesh. Results were compared to an existing finite difference program, solving the fully coupled poroelastic problem in one dimensional cylindrical co-ordinates (Figure 5.1). Output from the finite difference model was compared to output from the finite element model for a coarse, medium and fine mesh with 648, 2448 and 9504 nodes respectively. Whilst displacements were in reasonably good agreement with one another, pressure output was dependent on mesh refinement (Figure 5.1(b)). This effect has been noted in finite element models with very low permeability such as the value $\kappa = 6.6 \times 10^{-14}\,\mathrm{m}^2$ used here for spinal cord tissue (Stokes et al., 2010; Vermeer and Verruijt, 1981).

5.1.3 Mesh refinement

Two simulations were run for $t = 5\,\mathrm{s}$ with spinal cord meshes of $\sim$2600 and $\sim$10000 nodes using the white matter parameters in Table 5.1. This took a total of 45 min and 5 h respectively using a desktop computer with an Intel Core i7

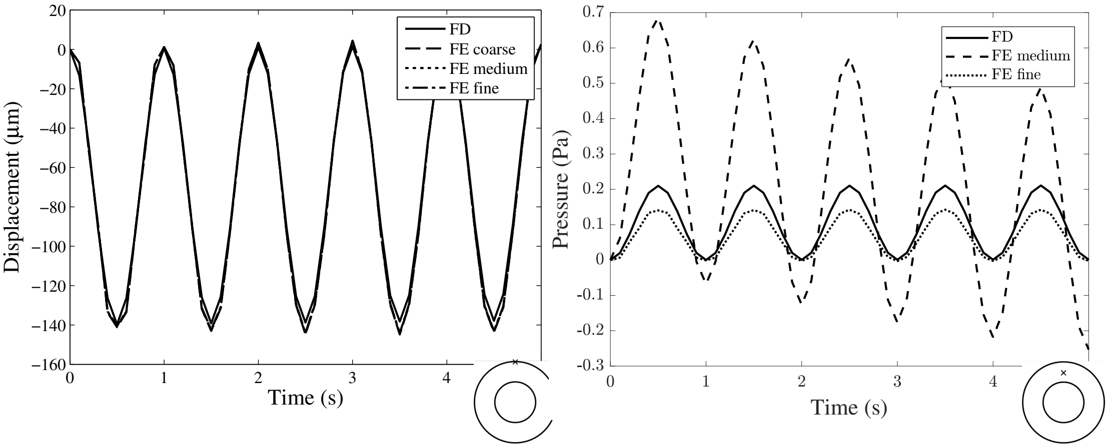

(a) Displacements.

(b) Pressure.

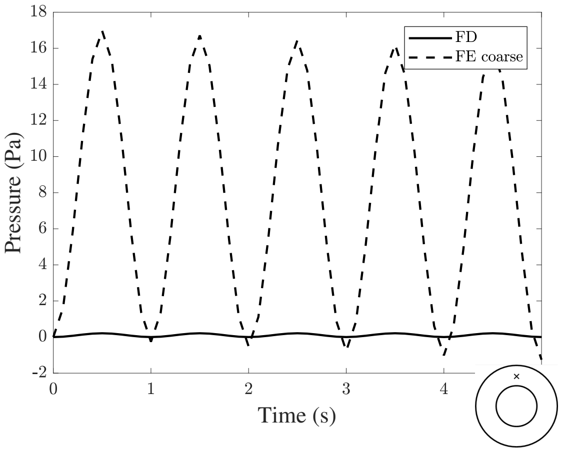

(c) Pressure (coarse mesh only).

Figure 5.1: A comparison of 5.1(a) displacement and 5.1(b) pressure results from the finite difference model (FD) and the finite element model for three mesh sizes (FE coarse, FE medium, FE fine). Pressure results for the coarse mesh plotted separately (Figure 5.1(c)) as output is significantly higher.

processor and 16BG RAM. The results can be seen in Figure 5.2. The results were near identical for both meshes, therefore the coarse mesh was chosen for the simulations to reduce run time.

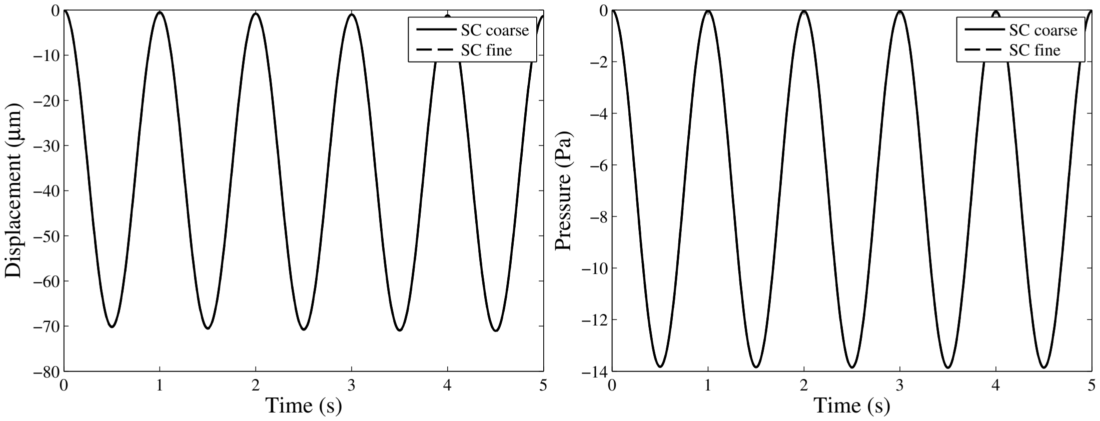

(a) Displacements.

(b) Pressure.

Figure 5.2: A comparison of 5.2(a) displacement and 5.2(b) pressure results for the spinal cord meshes with $\sim$ 2600 and $\sim$ 10000 nodes; both lines overlap.

5.1.4 Results analysis and post-processing

The finite element simulation calculates displacement and pressure at each node of the spinal cord mesh. Solid skeleton displacement and pore fluid pressure are approximations of the spinal cord cell tissue displacement and ECF pressure respectively. ECF pressures are compared to see how pressure gradients in the cord are affected. As different regions of the cord have different elasticity values, displacements are less revealing of potential cord damage than material stress. Stresses were recovered on each element during post-processing; stress provides an indication of where the cord is more likely to sustain damage that could lead to syrinx formation. To ease the comparison across different regions of the cord, principal stresses were calculated for each element, details of the stress recovery, principal stress calculation and nodal stress averaging can be seen in Appendix C. In the following sections pressure and stress have been plotted at various points across the cord cross section; for a breakdown see Figure 5.3.

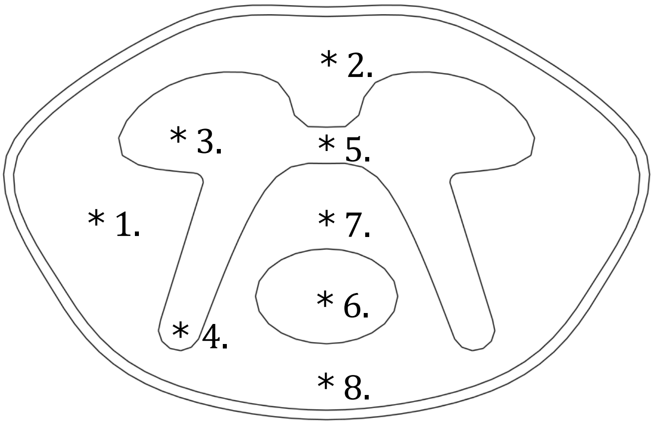

Figure 5.3: Points on the spinal cord cross section where pressure and stress have been evaluated and plotted. 1. lateral white matter; 2. anterior white matter; 3. grey matter ventral horn; 4. grey matter dorsal horn; 5. central grey matter; 6. oedema region; 7. central white matter; 8. posterior white matter.

5.2 Simulations

The primary aim of the simulations is to examine how stress and pressure in spinal cord tissue is affected by external CSF pressures. CSF pressure in the SAS is affected by pulse and is approximated using the function described in Chapter 2

$$p_b = A(\tfrac{1}{2} - \tfrac{1}{2}\cos(2\pi t))\,. \qquad \text{((2.29) restated)}$$

Based on values from the literature (Chapter 3, Section 3.6), healthy and pathological values of A are approximated with 200 Pa and 350 Pa respectively. The impact of a grey matter region, NRDL, stiff pia mater and oedema region are also evaluated. Five variations are included in the simulations, details of which can be seen in Table 5.2. Model SP has uniform parameters across the entire cord cross section; white matter parameters (as in Table 5.1) are used. Model GM introduces a region of grey matter and GMoed adds a region of oedema to this.

Model GMpia includes both a grey matter region and a pia mater and GMpiaoed adds a region of oedema to this. Where stress values are reported, a negative value implies compressive stress and positive value implies tensile stress.

Table 5.2: Variations of anatomical features included in the model.

Model name	**Features**	**Diagram**
SP (same parameters)	None	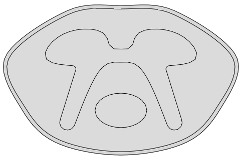
GM	Grey matter	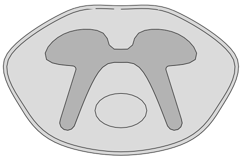
GMoed	Grey matter, oedema	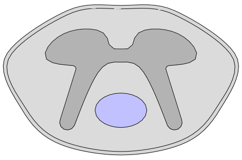
GMpia	Grey matter, pia mater	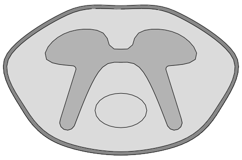
GMpiaoed	Grey matter, pia mater, oedema	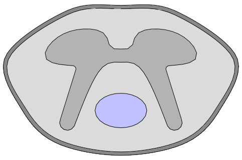

5.2.1 Grey matter

Of the existing poroelastic models of syringomyelia, few have included separate tissue properties for grey matter (for example Støverud et al. (2016a)) and none have examined how this affects stress in the spinal cord cross section. A region of grey matter with different tissue properties is included to evaluate how it affects stress and pressure distribution throughout the spinal cord. Introducing a stiffer and slightly less permeable grey matter region decreases the magnitude of pressure in the grey matter, particularly in the ventral horn (~80 Pa), see Figure 5.4. Pressure in the white matter is largely unchanged, except in the central white matter where the magnitude of pressure is slightly (~20 Pa) decreased (not shown).

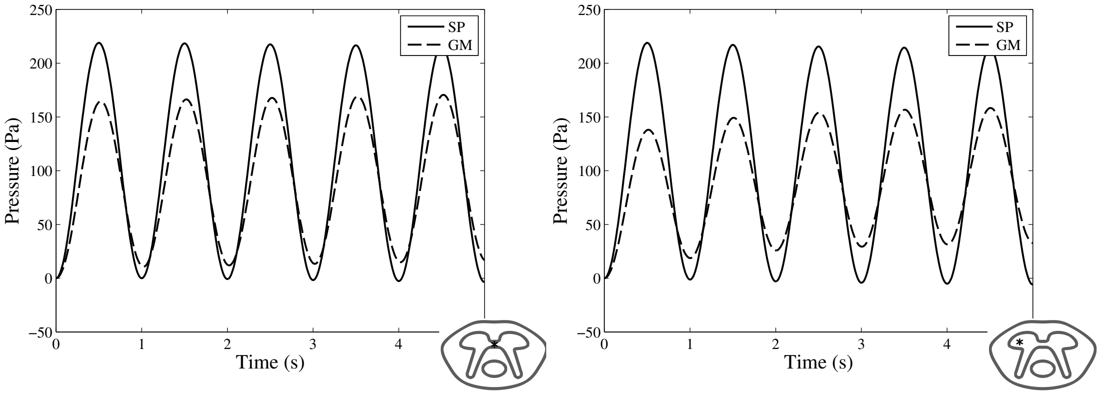

(a) Central grey matter.

(b) Grey matter ventral horn.

Figure 5.4: Comparison of pressure in the SP and GM models.

The magnitude of stress in the cord is affected by using different material parameters for grey matter. In white matter regions the magnitude of stress is minimally affected (<5 Pa). As expected grey matter stress is significantly affected, stress in the grey matter regions can be seen in Figure 5.5. Stress magnitude is increased by ~45 Pa in the grey matter ventral horn, ~43 Pa in the grey matter dorsal horn and ~82 Pa in the central grey matter.

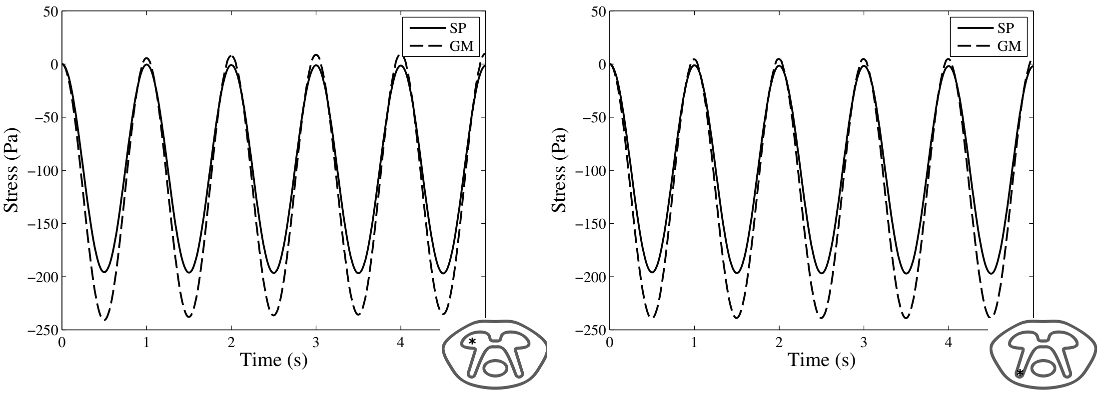

(a) Ventral horn.

(b) Dorsal horn.

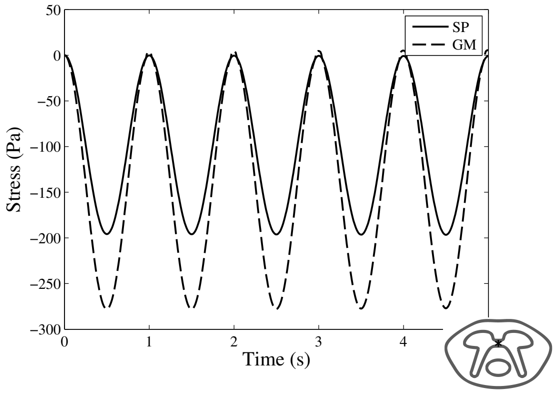

(c) Central grey matter.

Figure 5.5: Comparison of stress in the grey matter for the SP and GM models.

These results suggest that a stiffer grey matter increases compressive stress throughout the cord cross section especially in the grey matter region. Slightly increased porosity and decreased permeability in grey matter decreases the magnitude of pressure which in turn increases the magnitude of stress in the cord tissue. Grey matter and white matter are known to be different and these results suggest that grey and white matter material differences should not be neglected in poroelastic cord models as they affect model results, particularly in and near the grey matter.

5.2.2 Nerve roots and denticulate ligaments

The spinal cord is tethered in approximately the centre of the spinal canal by NRDL; denticulate ligaments in particular are known to apply a slight tension to the cord (Tunturi, 1978). To date these have not been included in a syringomyelia model to evaluate whether their mechanical effect may influence cavity formation.

The presence of NRDL tethering reduces pressure in all areas of the cord cross section (see Figure 5.6). When the external CSF pressure is at its highest (200 Pa) the pressure reduction is greatest (~70 Pa) in the anterior white matter and grey matter dorsal horn (see Figure 5.7); these regions are nearest to the sites of NRDL tethering. Interestingly the smallest pressure reduction occurred in the posterior white matter (~19 Pa, not shown) although this region was further from the NRDL tethering than the anterior white matter. It should be noted that NRDL were modelled by restraining displacements in the model - no change was made to the fluid pressure equation. All pressure changes arise due to the coupling between the solid and fluid equations.

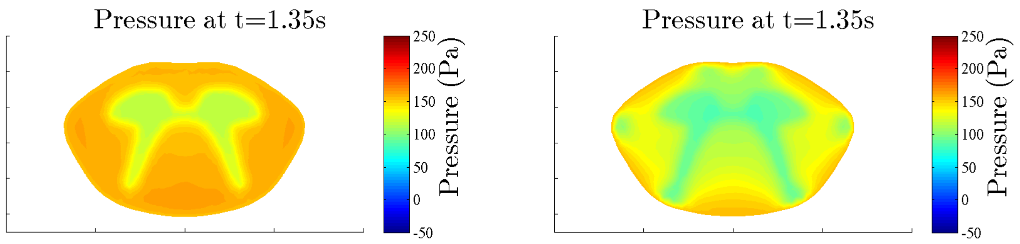

(a) Without NRDL tethering. (b) With NRDL tethering.

Figure 5.6: Effects of NRDL tethering on pressure across the cord cross section for the GM model, plotted at $t = 1.35\,\mathrm{s}$.

Comparing stresses in the GM model with and without NRDL tethering revealed a reduction of compressive stress in the cord. The lateral and posterior white

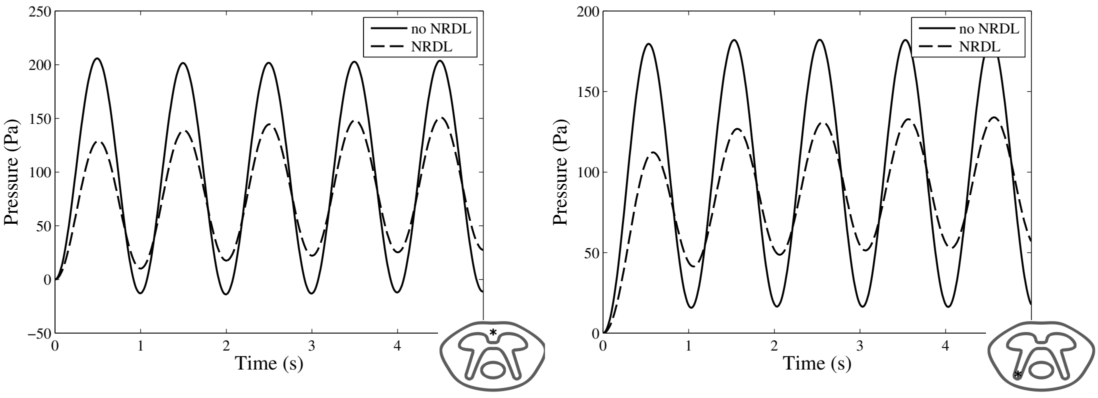

(a) Anterior white matter.

(b) Grey matter dorsal horn.

Figure 5.7: Comparison of pressure in the GM model both with (NRDL) and without (no NRDL) the effects of NRDL tethering.

matter showed a slight (<5 Pa) increase in compressive stress. The anterior and central white matter regions along with the central and dorsal horn grey matter region showed a reduction in the magnitude of stress (see Figure 5.8). This reduction suggests that NRDL tethering limits the amount of stress that can propagate through the cord.

Grey matter is modelled as slightly less permeable and more porous than white matter, consequently the reduced ECF pressure found when NRDL are introduced reduces the magnitude of stress in the tissue. Furthermore, *in vivo* the sites where nerve rootlets enter the spinal cord are aligned with the tips of the grey matter ventral and dorsal horns. In the simulations this restricted motion reduces the amount of external CSF loading the horns are subjected to, reducing stress in these regions. Tethering due to the anterior nerve rootlets (top of the cross section) may be responsible for the reduction of stress seen in the central grey matter (Figure 5.8(c)).

Comparing the central grey matter region in the SP (same parameters) model both with and without NRDL demonstrates that when the grey matter region is not modelled with separate parameters (as in the GM model), NRDL still reduces

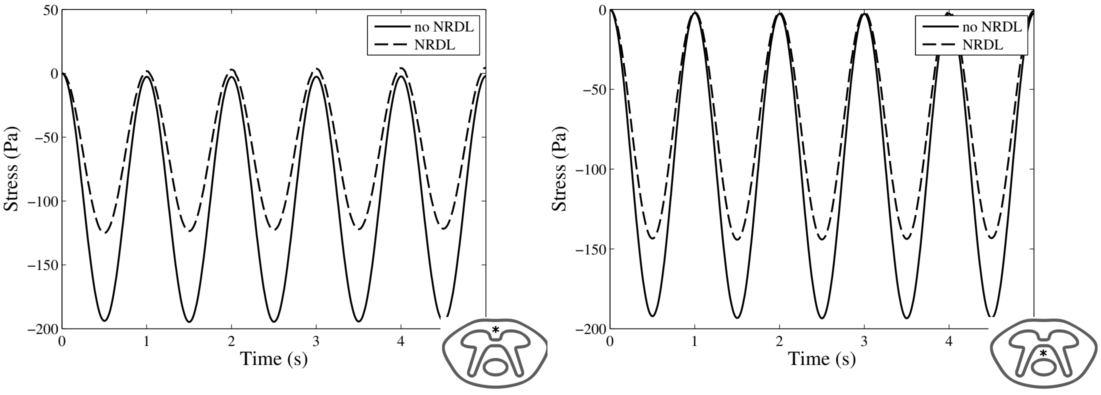

(a) Anterior white matter.

(b) Central white matter.

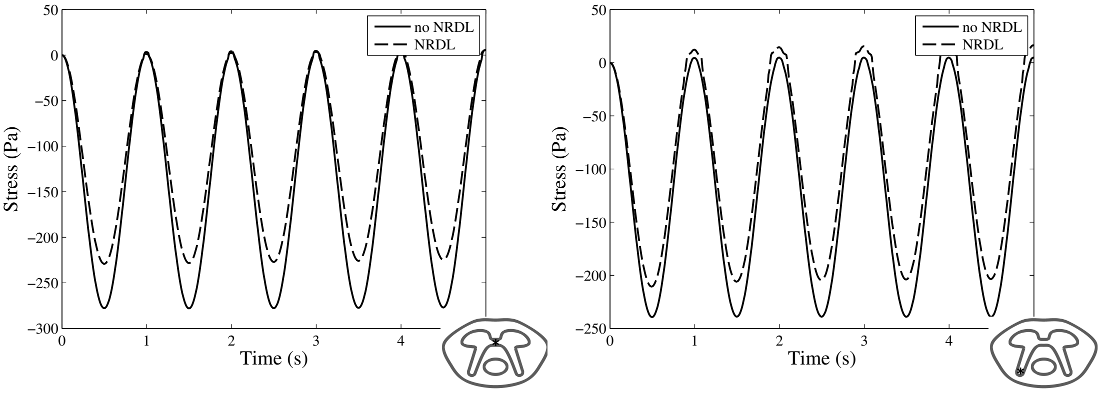

(c) Central grey matter.

(d) Grey matter dorsal horn.

Figure 5.8: Comparison of stress in the GM model both with (NRDL) and without (no NRDL) the effects of NRDL tethering.

the magnitude of stress in the central grey matter (Figure 5.9). This shows that including NRDL in spinal cord models is important as it will affect stress and pressure results.

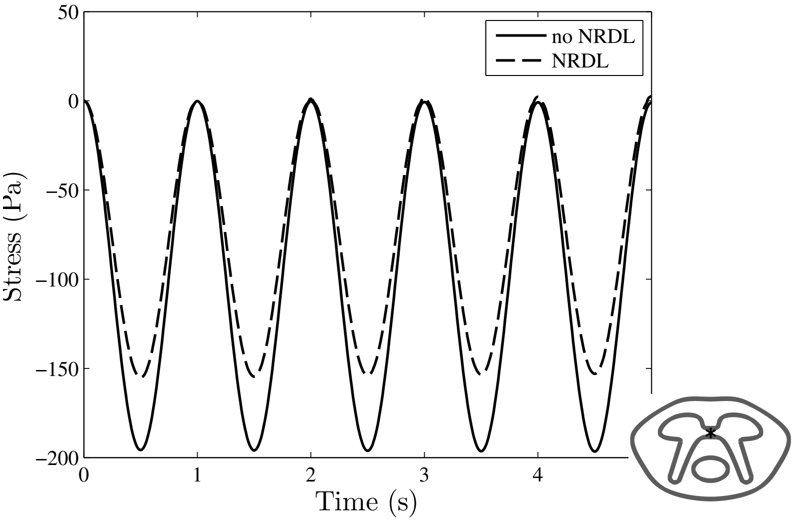

Figure 5.9: Comparison of the SP model with and without NRDL. Stress in the central grey matter region is plotted.

5.2.3 Oedema

Oedema is seen alongside syringomyelia cavities and its presence has been recorded in the spinal cord prior to cavity formation, leading it to be referred to as a presyrinx state (Fischbein et al., 2000). A region of increased porosity and permeability is introduced to the poroelastic model to simulate tissue oedema and the effects of this are evaluated. Elastic parameters in the oedema region such as Young's modulus and Poisson's ratio remain the same as the surrounding white matter.

When the cord is subjected to increased pressure from the external CSF it experiences compressive stress which is affected slightly by the coupling term ($-Q\boldsymbol{p}$) in the solid equation. The region of oedema in the GMoed model experiences a slight ($\sim$0.8 Pa) pressure decrease when compared to the GM model without oedema (not shown). The fluid to solid coupling causes a slight reduction in compressive stress in the oedema region, see Figure 5.10. Although the overall stress change is small ($\sim$1 Pa) in the oedema region, it is larger than stress change in other regions of the cord (mean $\sim$0.07 Pa).

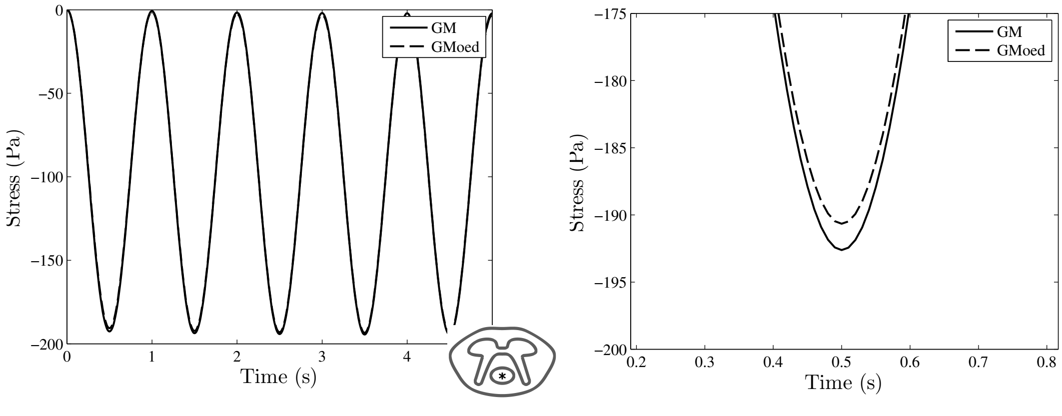

(a) (b)

Figure 5.10: Effects of oedema on stress in the cord, models without (GM) and with (GMoed) oedema are plotted from the same region. The small compressive stress reduction is magnified in Figure 5.10(b).

The tethering effects of nerve roots and denticulate ligaments (NRDL) have not been examined in relation to syringomyelia. Examining the effects of oedema with the GM and GMoed models when NRDL are introduced again reveals that pressure is slightly (~0.5 Pa, not shown) reduced. However, the presence of NRDL tethering causes compressive stress in the oedema region to be increased (~1.6 Pa), see Figure 5.11.

This is important as it demonstrates that NRDL tethering causes stresses to be increased in a region of tissue oedema, whereas stress was reduced in the tissue oedema in the model without NRDL tethering (Figure 5.10). This highlights the importance of including this anatomical feature and suggests a potential mechanism of cavity formation; that the presence of presyrinx oedema increases stress in the cord which over time could lead to tissue damage and syrinx formation. Theories of syringomyelia cavity development have attributed CSF pressure dropping in the SAS to syrinx formation (Greitz, 2006). When the external CSF boundary condition is changed from $A = 200\,\text{Pa}$ to $A = -200\,\text{Pa}$ to simulate a CSF pressure drop in the SAS, tensile stress in the oedema region is similarly increased (see

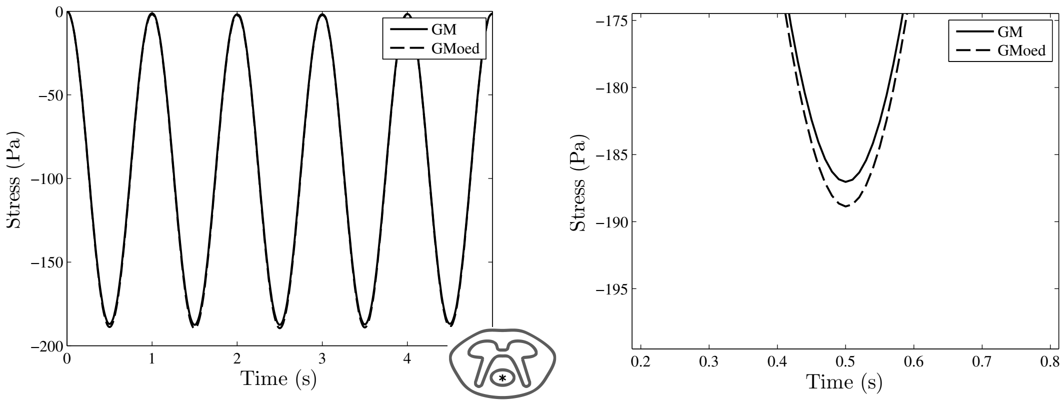

(a) (b)

Figure 5.11: Effects of oedema on stress in the cord when NRDL are included in the model. Models without (GM) and with (GMoed) oedema are plotted from the same region. The small stress increase is magnified in Figure 5.11(b).

Figure 5.12).

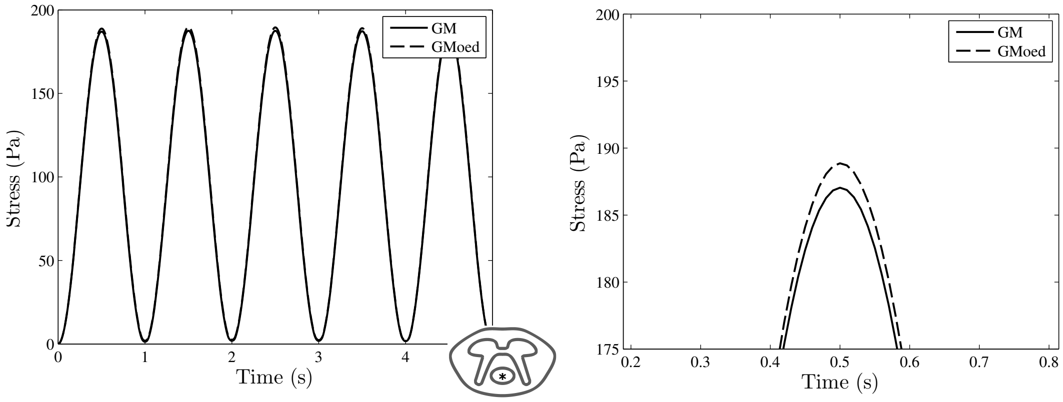

(a) (b)

Figure 5.12: Stress in the cord when CSF pressure outside the cord drops. Stress is plotted from the oedema region for the models with (GMoed) and without (GM) increased porosity and permeability in this area. The small stress change is magnified in Figure 5.12(b).

It is interesting to note that a negative pressure gradient leading into the oedema region would suggest a possible mechanism for fluid to move towards the oedema, potentially contributing to cavity formation. Examining the pressures in and near the oedema region does not reveal any tendency towards this behaviour, see Figure 5.13. The introduction of NRDL tethering did however steepen pressure gradients through the oedema region (Figure 5.13(a)) although the pressure gradients lead to the centre of the cord rather than the oedema.

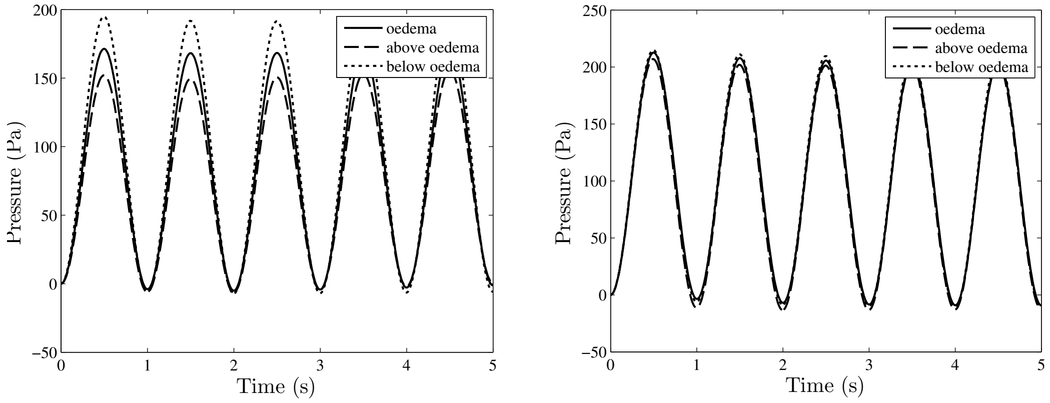

(a) (b)

Figure 5.13: Comparison of pressure at a point within the oedema, above the oedema and below the oedema. Plotted from the GMoed model both 5.13(a) with NRDL and 5.13(b) without NRDL tethering.

The findings here demonstrate that in a poroelastic material model with low permeability, a region of increased fluid content has a small effect on tissue stress and ECF pressure. This has relevance for modelling syringomyelia as it presents a way of modelling presyrinx oedema. The findings also have implications for theories of cavity formation as the presence of increased ECF (that is, oedema) increases both compressive and tensile stress in the oedema region and creates an environment where a cavity is more likely to form.

5.2.4 Pathological CSF pressures

Syringomyelia is often preceded by abnormal or exaggerated CSF flow and pressure in the SAS, caused by spinal cord conditions or injuries. To examine the effects of increased CSF on pressure and stress in the spinal cord the amplitude A of the boundary condition

$$p_b = A(\tfrac{1}{2} - \tfrac{1}{2}\cos(2\pi t))$$

is increased to $A = 350$Pa which simulates increased CSF pressure in the spinal SAS. As expected in a linear poroelastic model the stress and pressure increase linearly with increased CSF loading and the presence of oedema does not affect this. Figure 5.14 compares stresses in the oedema region for both healthy and pathological CSF loading pressures for both the GM and GMoed models. In both the GM and GMoed models the increased loading increases stress by 75 %.

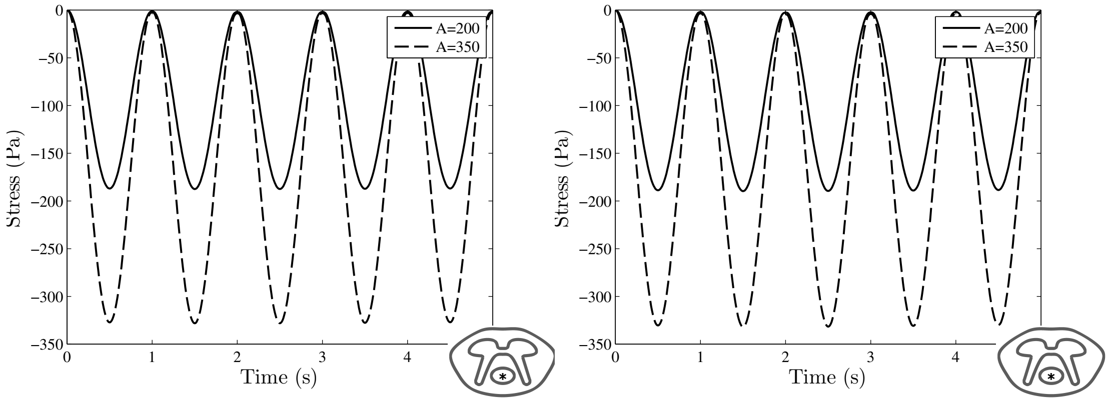

(a) GM model.

(b) GMoed model.

Figure 5.14: The effect of increased CSF loading on stress in the cord, comparing simulated healthy ($A = 200$Pa) and pathological ($A = 350$Pa) CSF pressure. Plotted from the oedema region for the 5.14(a) GM model and the 5.14(b) GMoed model.

5.3 Sensitivity analysis

As described previously, there is uncertainty surrounding the mechanical and poroelastic parameters that describe spinal cord tissue. With this in mind, a sensitivity analysis has been carried out to evaluate the impact of the parameters chosen for the model.

5.3.1 Young's modulus

White matter is modelled as softer than grey matter (5000 Pa and 10 000 Pa respectively), although whether this is the case remains to be confirmed (see Section 3.2.1). Examining the effects of a softer grey than white matter (YM $E = 5000\,\mathrm{Pa}$ and 10 000 Pa respectively) shows that pressure is reduced in all areas of the cord (see, for example, the lateral white matter in Figure 5.15(a)) except the anterior grey matter horn (Figure 5.15(b)). Compared to the model with stiffer grey matter, the model with softer grey matter has increased stress in the white matter and decreased stress in the grey matter (see Figure 5.16). Examining how a softer grey matter region affected the finding that oedema increases stress in the cord shows that this effect is increased, with stress in the oedema region increased by ~10 Pa (Figure 5.17).

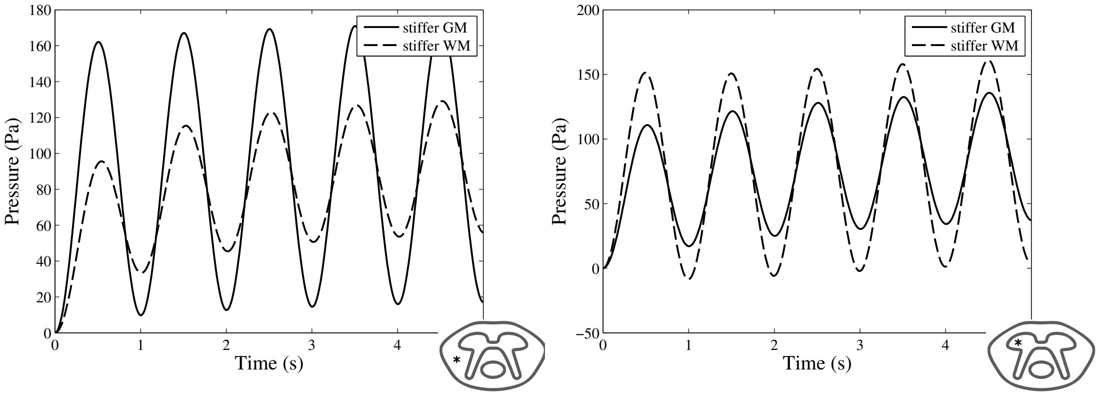

(a) Lateral white matter.

(b) Anterior grey matter horn.

Figure 5.15: Comparison of pressure in different regions of the cord for the GM model, with grey matter Young's modulus 10 000 Pa (stiffer GM) and 5000 Pa (stiffer WM).

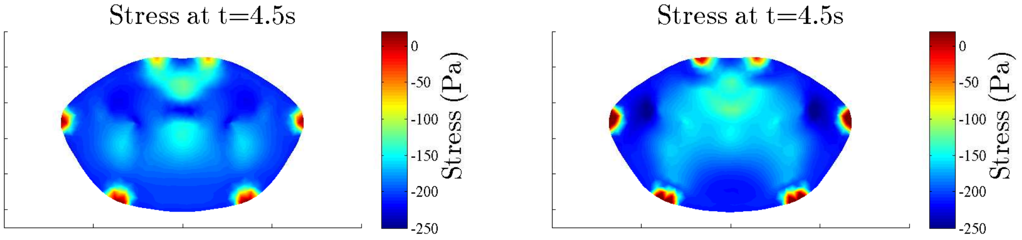

(a)

(b)

Figure 5.16: Stress distribution in the cord cross section for the GM model with 5.16(a) stiffer grey matter and 5.16(b) stiffer white matter.

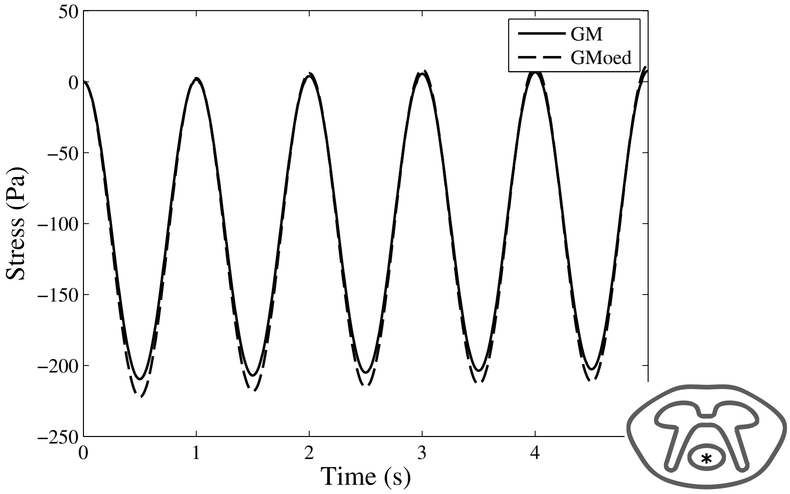

Figure 5.17: Comparison of stress in the oedema region for the GM and GMoed models when grey matter is modelled as softer than white matter.

5.3.2 Poroelastic coupling

The poroelastic model presented in Chapter 2 described a fully coupled system shown in Equation (2.21)

$$\begin{aligned} M\ddot{\boldsymbol{u}} + K\boldsymbol{u} - Q\boldsymbol{p} &= \boldsymbol{F}_s \\ Q^T\dot{\boldsymbol{u}} + S\dot{\boldsymbol{p}} + H\boldsymbol{p} &= \boldsymbol{F}_f \,. \end{aligned} \tag{(2.21) restated}$$

Poroelastic coupling models the effects of the solid skeleton on the pore fluid and the effects of the pore fluid on the solid skeleton. To examine the impact of this coupling two further simulations are run, with one way coupling

$$\begin{aligned} M\ddot{\boldsymbol{u}} + K\boldsymbol{u} - Q\boldsymbol{p} &= \boldsymbol{F}_s \\ S\dot{\boldsymbol{p}} + H\boldsymbol{p} &= \boldsymbol{F}_f \end{aligned}$$

and no coupling

$$
\begin{aligned}
M\ddot{\boldsymbol{u}} + K\boldsymbol{u} &= \boldsymbol{F}_s \\
S\dot{\boldsymbol{p}} + H\boldsymbol{p} &= \boldsymbol{F}_f \,.
\end{aligned}
$$

Comparing the results of an uncoupled, one way coupled and two way coupled model shows that pressure is affected more by the two way coupling (see Figure 5.18).

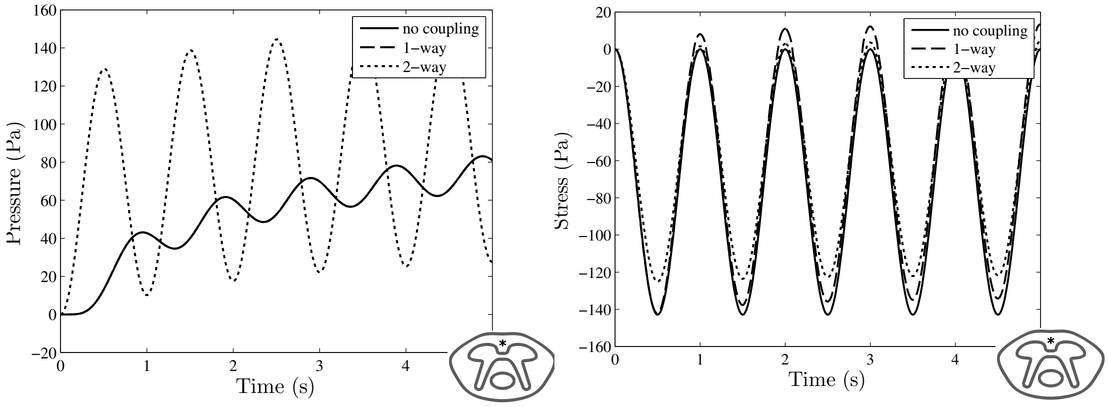

(a) (b)

Figure 5.18: Effects of poroelastic coupling on 5.18(a) pressure and 5.18(b) stress output. A representative plot from the anterior white matter region comparing models with no coupling, one way coupling (1-way) and two way coupling (2-way). In 5.18(a) the no coupling and 1-way plots overlap as for both models the pressure equation is uncoupled.

5.3.3 Poisson's ratio

Poisson's ratio of both grey and white matter is taken from the literature ($\nu = 0.4$). Comparing different values of PR ($\nu = 0.35$, 0.4 and 0.45) in the present poroelastic model reveals that increasing PR results in decreased pressure and compressive stress across the spinal cord cross section. Figure 5.19 shows these results in the central white matter although other cord regions show similar changes.

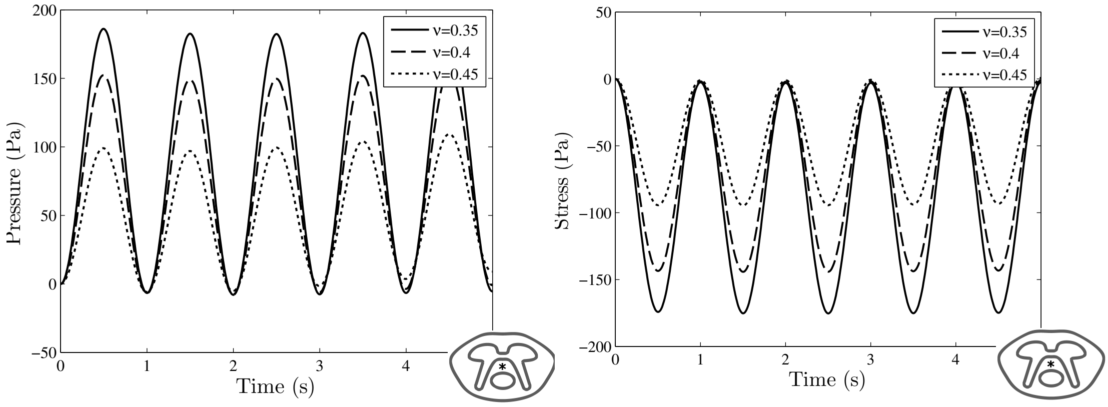

(a) (b)

Figure 5.19: Stress and pressure output from the GM model for three different values of Poisson's ratio ν. Results are plotted from the central white matter.

5.3.4 Biot modulus

In the model an inverse Biot modulus of $\frac{1}{M_b} = 0.0001$ is used. To evaluate the effect that the assumption of $\frac{1}{M_b} = 0.0001$ has on stress and pressure in a very low permeability material, simulations are run using a circular mesh. The circle has similar dimensions to the spinal cord, with radius 1 cm. As the value of $\frac{1}{M_b}$ increases, the pressure decreases and compressive stress increases (see Figure 5.20). For $\frac{1}{M_b} = 0.000001$, which is of a similar magnitude to that predicted in the spinal cord, the pressure is increased and is out of phase with the solid skeleton stress.

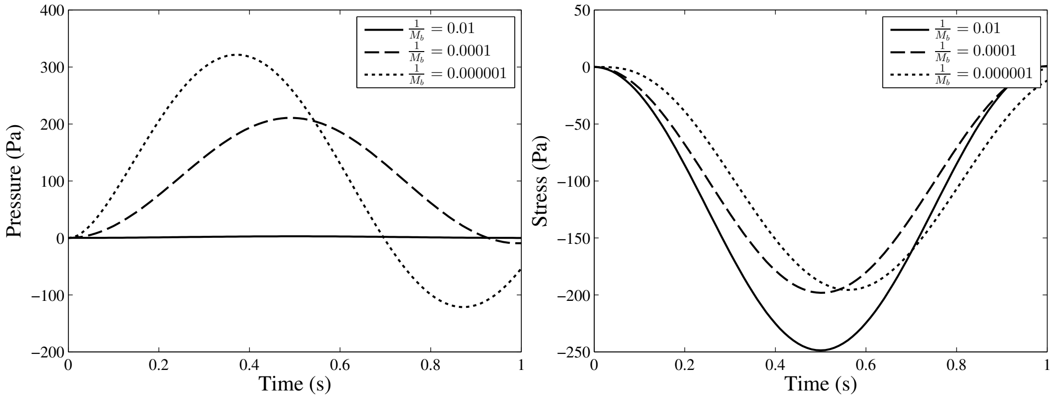

(a) (b)

Figure 5.20: Comparison of the effects of the inverse Biot modulus $\frac{1}{M_b}$ on 5.20(a) pressure and 5.20(b) stress in a material with low permeability.

5.4 Summary

The results presented here demonstrate that in a poroelastic model of the spinal cord cross section certain anatomical features such as grey matter should not be disregarded. NRDL were also found to affect the stress and pressure results which is beneficial as to date these have not been included in a model of syringomyelia. The tethering effects of NRDL were found to impact stresses in the cord caused by tissue oedema. In the absence of NRDL, oedema alleviated stress in the cord but their presence caused oedema to increase stress in the cord. Oedema has not been included in a poroelastic model of the cord and was represented here as region of increased porosity and permeability. The results showed that when oedema is modelled in this way, it contributes to stress in the spinal cord, suggesting a potential contributory mechanism towards syringomyelia cavity formation.

Chapter 6

Discussion

Introduction

Syringomyelia is a little understood condition affecting the spinal cord and the uncertainty surrounding its pathophysiology presents a problem to clinicians treating patients. The work here set out to develop a detailed poroelastic model of the spinal cord to better understand the mechanisms underlying syrinx formation.

A plane strain poroelastic model of the spinal cord cross section has revealed that certain anatomical features such as NRDL and different grey and white matter tissue properties significantly affect the stresses and pressure in the cord. The implications for future syringomyelia models are that these should not be neglected. Introducing a region of oedema to the model resulted in increased compressive and tensile stresses in this region. This contributes to the understanding of cavity formation in two ways. Firstly it presents the first study of how presyrinx oedema contributes to cavity formation from a mechanical perspective. Secondly it demonstrates how the cord might sustain damage internally when it is subjected to disturbed CSF pressure. These two findings are important in understanding how a syrinx might form.

In this final chapter an evaluation of the implications and limitations of the methods and findings are presented. Section 6.1 presents the simulation results in the context of existing syringomyelia research and explains how these findings contribute to understanding cavity formation. Section 6.2 evaluates the modelling techniques used to simulate the spinal cord and how the limitations may have impacted the results. Section 6.3 discusses the tissue properties chosen for the model, including limitations and implications of the DW-MRI based technique for calculating porosity and permeability, and how these affected the outcomes.

6.1 Implications for syringomyelia research

6.1.1 Summary of findings

The proposed hypothesis was that patients with a predisposition to disturbed CSF flow were more likely to develop syringomyelia if they had spinal cord oedema. Results from the poroelastic model showed that stress in a region of oedema is increased, supporting this hypothesis within limitations.

Given that the number of poroelastic models of syringomyelia is limited, the results here demonstrate that poroelasticity is a reasonable approximation for spinal cord tissue behaviour. In particular, when examining the pressure driven movement of fluid through the ECS in relation to syringomyelia cavity development, poroelasticity is particularly well suited.

The present model set out to examine the effect of certain anatomical features such as NRDL and a grey matter region on stresses and pressures in the spinal cord tissue. It was found that NRDL reduced stresses in the cord, particularly near the edges and that introducing a stiffer less permeable region of grey matter to the plane strain model increased stress in all regions of the cord cross section.

6.1.2 Clinical problem

Syringomyelia research has established that the disruption of CSF flow due to blockages in the SAS is at least partially responsible for the development of cavities in the spinal cord tissue (Flint and Rusbridge, 2014). Blockages of the SAS and CSF flow disturbances can occur as a result of conditions such as Chiari malformation (CM) and arachnoiditis or from traumatic SCI (Bilston et al., 2006; Klekamp, 2002; Pinna et al., 2000). Treatment options for syringomyelia are dependent on the cause and there is an element of uncertainty in deciding whether or not to carry out high risk surgical intervention (Flint, 2014).

To aid clinicians in making decisions on how best to treat a patient with a syrinx, or indeed whether to treat a patient with a stable syrinx at all, a better understanding of the mechanisms involved in cavity formation is required. Computational fluid dynamics studies and invasive pressure measurements have established that the presence of these blockages results in abnormal or exaggerated CSF pressures and velocities (Cheng et al., 2012; Clarke et al., 2013; Heiss et al., 2012; Støverud et al., 2013), although how this leads to cavity formation is uncertain.

Mechanisms of existing cavity growth have been evaluated (Harris and Hardwidge, 2010; Heil and Bertram, 2016) but to the best of the author's knowledge there has been no thorough examination of the processes taking place in the cord immediately prior to cavity formation. Oedema in the spinal cord has been noted prior to cavity formation (Fischbein et al., 2000) and near existing syrinxes (Akiyama et al., 2008) although its role in syringomyelia cavity formation has not been explored.

6.1.3 Syrinx formation

The research questions outlined in Chapter 1 were

- Is poroelasticity a suitable computational model for simulating syringomyelia?
- How does disturbed CSF affect the spinal cord cross section?
- Do regions of oedema in the spinal cord increase the likelihood of syringomyelia from a mechanical perspective?

The results presented in Chapter 5 demonstrated that NRDL tethering reduced stress in the cord. Introducing a stiffer less permeable grey matter region to the cord caused both grey and white matter stress to increase. In the presence of tissue oedema, represented as a region of increased porosity and permeability, compressive tissue stress within the cord increased when external CSF pressure increased. Similarly when external CSF pressure was decreased, tensile stress within the cord oedema region was increased. Removing NRDL tethering from the model reversed these effects. From this, it was deduced that oedema in the spinal cord under CSF loading provides an environment where damage to the spinal cord tissue, and therefore a syrinx, is more likely to occur.

The link between oedema and cavity formation could potentially explain why syringomyelia is associated with such a diverse array of conditions and injuries such as CM, arachnoiditis and traumatic SCI. In conjunction with disturbed CSF flow, oedema has been observed alongside the majority of these conditions and injuries (Akiyama et al., 2008; Hemley et al., 2012, 2013; Itoh et al., 2002; Klekamp et al., 2001). The present study has revealed a possible mechanical link between the presence of oedema and cord damage that, in the long term, could lead to syrinx growth.

The novel contribution of this work is to demonstrate that the presence of oedema in the spinal cord creates an environment in which a syringomyelia cavity is more likely to form, at least from a mechanical perspective. The link between oedema and syringomyelia has been probed by Feigin et al. (1971) and later Fischbein et al. (2000). Furthermore oedema has been noted in several experimental models of syringomyelia (Hackney et al., 1986; Josephson et al., 2001; Klekamp et al., 2001) and clinical case studies (Akiyama et al., 2008; Itoh et al., 2002). However, until now the causative link between oedema and syringomyelia has been unclear.

6.1.3.1 Occurence of spinal cord oedema with syringomyelia

The importance of the finding that oedema contributes to mechanical stress in the spinal cord becomes more apparent when the many instances of oedema occurring alongside syringomyelia are highlighted. Animal models of SCI have found oedema occuring shortly after the injury (Hackney et al., 1986) and it has been noted that oedema is often an inflammatory response to SCI (Brodbelt and Stoodley, 2003). Clinical case studies have found oedema alongside a syrinx in CM patients that resolved when the syrinx was treated (Akiyama et al., 2008).

Simulating oedema with a region of increased porosity and permeability resulted in decreased pressure and increased stresses in this region (Section 5.2.3, Chapter 5). When the cord was compressed by high CSF pressure, pressure across the cord section increased. This reasons for this behaviour become apparent when considering the fluid continuity equation

$$\alpha \frac{\partial \varepsilon_{ii}}{\partial t} + \frac{1}{M_b} \frac{\partial p}{\partial t} = \frac{\kappa}{\mu} \nabla^2 p \qquad \text{((2.8) restated)}$$

in the context of low permeability κ and inverse Biot modulus $\frac{1}{M_b}$. As $\kappa \rightarrow 0$ the continuity equation becomes dominated by the two left hand terms

$$\frac{1}{M_b} \frac{\partial p}{\partial t} = -\alpha \frac{\partial \varepsilon_{ii}}{\partial t} \,. \tag{6.1}$$

As the Biot Willis coefficient and inverse Biot modulus in the simulations were taken to be $\alpha = 0.9995$ and $\frac{1}{M_b} = 0.0001$ respectively, pressure changes in the ECF are very sensitive to the coupling term in the fluid equation.

Recalling the definition of the Biot modulus given in Chapter 3, Section 3.2.5 this effect is likely to become more prominent. Using the definition $M_b = \frac{K_s}{\alpha(1-\alpha)}$

Equation 6.1 can be rewritten

$$\frac{\partial p}{\partial t} = -\frac{K_s}{(1-\alpha)}\frac{\partial \boldsymbol{\varepsilon}_{ii}}{\partial t} \,. \tag{6.2}$$

The right hand side constant $\frac{K_s}{(1-\alpha)}$ will be large even with soft materials like the spinal cord which in the present model had a bulk modulus of $K_s \approx 8333\,\mathrm{Pa}$. Equation (6.2) demonstrates that when a material with very low permeability is deforming, pressure changes are driven by strains in the solid skeleton resulting in the pore pressure values seen in Chapter 5. Further discussion around the impact of poroelastic parameters in the spinal cord model is given in Section 6.3.

In the case of tissue oedema, the magnitude of pore pressure is reduced. Recalling the effective stress tensor

$$\boldsymbol{\sigma} = (1-\phi)\boldsymbol{\sigma}_s - \phi p\boldsymbol{I} \tag*{((2.2) restated)}$$

it becomes apparent why a negative pore pressure results in the increased stresses seen in the oedema region. Here a negative pore pressure implies a pressure lower than the initial condition, in the present model the pore pressure initial condition was zero. Poroelastic material models were developed to model hard materials like rocks and soils where the impact of the stiff solid skeleton altering pore pressure is easier to comprehend. In a soft material such as the spinal cord, the ability of the soft solid skeleton to affect pore pressure may be due to the fact that the system is fully saturated and that the stiffness of the solid skeleton may be dominated by fluid in tissue cells.

Traumatic SCI has been shown to increase pressure in the spinal cord (Dong et al., 2016) and it is interesting to note that oedema reduces pressure in a poroelastic material model. This indicates that from a mechanical perspective, oedema may form to alleviate pressure in the ECS which has the subsequent effect of worsening tissue stress although it should be noted that the pressure recordings in Dong et al. (2016) were measured from inside the spinal cord, not necessarily from the spinal cord ECS.

Developing oedema has been measured as regions of increasing fluid content in the brain (Vardakis et al., 2016). The present model represented an existing region of oedema and simulated this with a region of increased porosity and permeability. Fluid content values (ζ, see Chapter 2, Equation (2.4)) were not recovered from the pressure results but this would be an interesting marker of how fluid is varying in the spinal cord cross section.

Although the results have shown that an existing region of oedema could contribute to cavity formation, establishing how oedema forms is beyond the scope of this study. Klekamp et al. (2001) suggested that increased flow in the ECS may compensate for flow disruption in the SAS, although this is likely to be only one of the many contributing factors in oedema formation.

6.1.3.2 Oedema pathophysiology

In their study describing oedema as the presyrinx state, Fischbein et al. (2000) hypothesized that in circumstances preceding syringomyelia, perivascular spaces (PVS) play a prominent role in transporting fluid into the cord to create regions of oedema. This idea is supported by the finding that the PVS become dilated near a region of arachnoid scarring (Klekamp et al., 2001). The results of this thesis have built upon the notion of the presyrinx state by demonstrating that presyrinx oedema contributes to levels of stress in the spinal cord. When taken alongside studies that have suggested a syrinx forms to alleviate pressure in the cord (Elliott et al., 2011; Martin and Loth, 2009) this provides another step towards understanding the pathophysiology of this disease.

A case of oedema and syringomyelia following a foramen magnum decompression (FMD) to treat a patient with CM was reported by Nurboja and Choi (2009). They suggested several explanations such as direct trauma due to surgery or altered CSF flow as to how the oedema and syringomyelia formed, strengthening the link between disturbed CSF dynamics, oedema and syringomyelia. The pia mater may worsen existing oedema. Ozawa et al. (2004) suggested that in a region of higher pressure oedema the pia would restrict the cord resulting in damage.

Severity of spinal cord injury is thought to influence levels of pressure in the spinal cord (Dong et al., 2016) and the extent of swelling or oedema (Koyanagi et al., 1989). The model presented here has shown that the presence of oedema reduces ECF pressure and increases stress that could potentially damage the cord. Links between presyrinx oedema and the shape of the surrounding SAS have been noted (Gadde et al., 2017). This could be due to the shape of the SAS affecting pressure gradients around the spinal cord. When solely examining the mechanical behaviour of the cord, oedema may form to alleviate pressure which then has the unwanted effect of increasing tissue stresses and contributing to syrinx formation. However, the true situation is likely to be more complex than this.

Whilst examining the role of the water transport protein aquaporin-4 (AQP4) in oedema and swelling following traumatic SCI, Saadoun et al. (2008) demonstrated that mice lacking AQP4 had greatly reduced pressure and oedema following injury. This highlights the role of non-mechanical factors in oedema formation and indeed syringomyelia pathophysiology. Non-mechanical factors were not addressed in the poroelastic model presented here, however this work complements and provides a foundation for a more detailed model of spinal cord tissue behaviour.

6.1.3.3 Aquaporin-4 and syringomyelia

The water transport protein AQP4 is an increasingly relevant topic in syringomyelia research (Brodbelt, 2014; Hemley et al., 2012, 2013; Saadoun et al., 2008; Saadoun and Papadopoulos, 2010). Current evidence is contradictory regarding the role of AQP4 in syrinx development. Hemley et al. (2013) found high levels of AQP4 near a syrinx induced by arachnoiditis although it was not clear whether its presence was a cause or consequence of the syrinx.

Following a spinal cord compression injury, mice without the AQP4 protein were found to have less swelling, less fluid content and lower pressure in the spinal cord (Saadoun et al., 2008). The consequent reduced oedema indicates a lower risk of cavity formation. An AQP4 study involving syrinxes that are an expansion of the central canal (canalicular syrinxes, see Chapter 1, Section 1.1.3) found no significant increase in levels of AQP4 near a canalicular syrinx (Hemley et al., 2012). It appears the relevance of AQP4 in syrinx development may be dependent on whether the syringomyelia develops as a result of CM, SCI or other conditions such as arachnoiditis.

Whether oedema is more likely to form in grey or white matter is uncertain. Oedema induced by arachnoiditis has been found to form in the white matter near the arachnoid scar and in the grey matter below it (Klekamp et al., 2001), other studies have found increased fluid content in white matter following induced oedema (Naruse et al., 2000). Oshio et al. (2004) found that AQP4 is expressed predominantly in the spinal cord grey matter. It would perhaps be unwise to assume oedema is more likely to form in the grey matter due to the increased presence of AQP4 as there are likely other factors that contribute to oedema formation.

At present the exact role of AQP4 in the pathophysiology of syringomyelia is uncertain. Furthermore, recent research into CSF production and absorption in the CNS suggests that increased pressure lowers the production of CSF and vice versa (Chikly and Quaghebeur, 2013). With this in mind it is evident that several factors contribute to the production, absorption and movement of ECF within the spinal cord. The model described in Chapter 2 did not address the influence of AQP4 or other biochemical effects on syrinx formation. It does however provide a foundation for future models that include fluid sink or source terms in the equations to model these effects.

6.1.3.4 Implications for syrinx formation theories

The results presented in Chapter 5, Section 5.2.3 showed that the presence of oedema increases the likelihood of internal cord damage. Although the connection between syringomyelia, oedema and potentially AQP4 is still under investigation, the mechanical, biochemical, experimental and clinical findings suggest that oedema does play an important role in syrinx formation.

Spinal cord ECF, blood and surrounding CSF are thought to maintain a dynamic equilibrium with one another, an effect known as the Monro-Kellie hypothesis (Mokri, 2001). Hackney et al. (1986) noted that blood flow to the grey matter declined soon after a compression spinal cord injury due to an increased volume of fluid in the PVS surrounding the blood vessels. According to the Monro-Kellie hypothesis, this may cause an excess of ECF in the area or the SAS surrounding the cord if the blood flow reduction does not fully compensate for increased fluid in the PVS. Furthermore the role of PVS as a means for fluid to enter the spinal cord tissue from the SAS is under investigation (Lloyd et al., 2017).

The finding that the presence of oedema can increase stress in the spinal cord tissue lends support to other theories of syrinx formation. Greitz (2006) proposed the intramedullary pulse pressure theory (IMPPT) which aimed to explain syringomyelia following CM, SCI and all other causes. The IMPPT states that syringomyelia develops when the cord is repeatedly distended due to CSF pressure decreases and that a syrinx is an accumulation of ECF. A poroelastic model is well suited to examine pressures and movement of ECF in the cord. Other authors have found that pressure drops near an SAS blockage are not strong enough to distend the cord enough to cause damage (Martin and Loth, 2009). However this does not consider the behaviour of fluid inside the spinal cord. The poroelastic model allowed ECF pressure to affect tissue stress and allowed the tissue solid skeleton (cells) to affect ECF pressure. Simulation results in Section 5.2 demonstrated that ECF pressure change is strongly driven by the solid skeleton deformations and that stress in the cord is affected by these changes. With this in mind, the true pressure dynamics that occur within the spinal cord may be more complex than previously thought and the notion that syrinx fluid originates from the ECS should not be dismissed.

It is established in syringomyelia research that disrupted CSF dynamics play an important role in syrinx formation (Flint and Rusbridge, 2014). Section 5.2.4 showed how both pressure and stress increased linearly when the boundary pressure applied to the spinal cord model was increased. Stress in the oedema region increased by ~1% regardless of the external pressure boundary condition. This was expected as the poroelastic tissue model had a linear elastic solid skeleton. At present there is little information regarding what level of stress is likely to cause damage in the spinal cord. If there was an indication of the yield stress of spinal cord tissue, it would be possible to use a model such as this to determine at what magnitude CSF pressure might become problematic.

6.1.4 Anatomical features

Anatomical features such as nerve roots and denticulate ligaments (NRDL) and different grey and white matter tissue properties were included in the model to examine how they affected stress and pressure distribution in the spinal cord. White matter YM was 5000 Pa and grey matter was represented as a region of increased stiffness $E = 10\,000\,\mathrm{Pa}$, porosity $\phi = 0.25$ and decreased permeability $\kappa = 3.3 \times 10^{-14}\,\mathrm{m}^2$. Section 5.2.1 described how introducing a grey matter region with these properties decreased the magnitude of pressure and increased the magnitude of stress, particularly in the grey matter region. Although the most suitable possible grey and white matter properties were chosen for the model, there is uncertainty as to whether grey or white matter is mechanically stiffer (see Section 3.2.1).

Modelling the grey matter as softer than white matter revealed reduced pressure in almost all areas of the cord, along with increased stress in white matter and decreased stress in grey matter (Section 5.3.1). Støverud et al. (2016a) found a negligible difference when modelling grey matter separately as only the permeability, not elasticity, properties were different. Evaluating the impact of modelling grey matter as softer on the findings relating to oedema showed that stress was still increased in the oedema region (Figure 5.17).

Grey matter is known to have a higher concentration of blood vessels than white matter (Bilston, 2016; Melissano et al., 2015) and perfused blood vessels are thought to give additional stiffness to CNS tissues (Bilston, 2002). If grey matter is indeed stiffer than white matter it could explain findings such as how post SCI extracanalicular syrinxes mainly form in grey matter (Brodbelt and Stoodley, 2003; Wong et al., 2012). Both the increased concentration of blood vessels and increased AQP4 levels in the grey matter (Oshio et al., 2004) may also play a role in the formation of cavities in grey matter.

NRDL tethering has not, to the author's best knowledge, been included in a poroelastic model of the spinal cord. The findings in Chapter 5, Section 5.2.2 demonstrated that NRDL tethering reduces pressure and stress across the cord cross section although a slight (<5 Pa) stress increase was found in the cord white matter. This implies that the effects of NRDL tethering should be considered in future models of syringomyelia.

The central canal (CC) was neglected in the present model and it has been found that fluid moves preferentially along a modelled CC (Støverud et al., 2011). This effect is not represented in the present two dimensional model. Milhorat et al. (1994) found that the CC is closed in many adults therefore excluding it from the model, whilst a simplification, may not be a major assumption. Furthermore, as the present model was focussing on the stage immediately prior to syrinx formation (see Chapter 1, Figure 1.12), an open section of CC or a small existing syrinx was not necessary.

6.1.5 Limitations

It should be noted that the pressures and stresses reported in Chapter 5 are not absolute values as the initial conditions were zero. However, they do give an indication of whether particular regions of the cord are more susceptible to high stress and potentially damage. As with any biological tissue there are difficulties surrounding accurate measurement of spinal cord mechanical properties, making it hard to verify absolute pressure and stress values calculated using a mathematical model. Currently there are no reported figures of the absolute stress levels required to damage the cord during syrinx formation. As such, these initial findings that relative stresses are increased when oedema is present are still beneficial to the understanding of cavity formation.

Whilst the present study has demonstrated that a region of higher porosity and permeability such as oedema can increase tissue pressures and stresses, the link to syringomyelia is still being explored. For example, although the presyrinx state has been demonstrated in certain circumstances (Fischbein et al., 2000), it is not known whether oedema always precedes syringomyelia. However, clinical imaging used to diagnose and monitor syringomyelia does look for presyrinx oedema in susceptible patients (Ross and Moore, 2015).

6.1.6 Clinical application

There are several clinical studies showing oedema preceding syringomyelia (Akiyama et al., 2008; Gauge et al., 2012; Itoh et al., 2002; Levy et al., 2000; Nair et al., 2006) and the assertion by Fischbein et al. (2000) that oedema represents the presyrinx state is fairly well established. Diagnostic techniques for syringomyelia often revolve around looking for this presyrinx region (Jinkins et al., 1998; Ross and Moore, 2015). The finding that oedema increases mechanical stress in the spinal cord is important as it contributes to the understanding of how presyrinx oedema could lead to syrinx formation from a mechanical viewpoint. Imaging techniques that quantify the water content in the spinal cord such as the NODDI technique presented in Chapter 4 would be beneficial in a clinical setting to evaluate the level of tissue oedema and ultimately the risk that a syrinx may form or worsen.

6.2 Poroelastic model evaluation

6.2.1 Poroelastic material model

There is evidence to suggest that the dominant causes of syringomyelia cavities are mechanical rather than biological as CSF pressure and flow disruption is frequently associated with syringomyelia. For example, syrinxes associated with CM often resolve following decompression surgery (Klekamp, 2014) or whole cord syrinxes completely resolve following the removal of an arachnoid cyst (Thakar et al., 2011). Unfortunately, neurological damage to the cord is not always reversed even if the cavity itself has closed. The present model used a poroelastic model to examine tissue stress and ECF pressure within the cord when conditions preceding cavity formation were simulated, whereas existing poroelastic models have looked at an existing cavity (Heil and Bertram, 2016) or the effect of cord geometry (Støverud et al., 2016a).

Two way poroelastic coupling in the model allowed the effects of the solid skeleton on the pore pressure to be modelled and vice versa. Comparing the effects of an uncoupled, one way coupled and fully two way coupled model revealed that two way coupling has more of an impact on pressure than stress (Section 5.3.2). The pressure changes become dominated by the $Q^T\dot{\boldsymbol{u}}$ coupling term. One way coupled models of the spinal cord tissue exist and this demonstrates that two way coupling is important and should not be neglected. It is important to note that poroelastic equations were developed with stiff materials such as rocks and soils in mind (Biot, 1941); in soft, fully saturated tissues like the spinal cord the effects of solid to fluid coupling may cause additional damage to the solid skeleton as the pore pressure resists the solid skeleton strains. A full FSI model combining the spinal cord and CSF fluid dynamics was not built although it is thought that a full FSI model has minimal effects on the CSF pressure (Cheng et al., 2014).

However, the presence of CM is thought to increase spinal cord/CSF pressure interaction (Pahlavian et al., 2015).

Poroelastic material models are increasingly being used to simulate CNS tissues in relation to a variety of conditions (Bertram and Heil, 2017; Harris and Hardwidge, 2010; Wirth and Sobey, 2006). Syringomyelia is characterised by an accumulation of fluid within the spinal cord tissue, the development of which is increasingly attributed to CSF flow disturbances in the SAS surrounding the cord (Elliott et al., 2013; Flint and Rusbridge, 2014). In the present work, a poroelastic material model was chosen to allow the analysis of both tissue stresses and ECF pressures within the cord to help identify factors that contribute to syrinx formation. Furthermore, the use of the poroelastic model allowed the mechanical impact of spinal cord oedema, often found preceding and alongside syrinxes, to be analysed. An existing area of oedema was modelled as a region of increased porosity and permeability to represent the increased extracellular fluid content characteristic of oedema preceding syringomyelia. Developing oedema has been studied in brain tissue by identifying regions of increasing fluid content (Nagashima et al., 1990; Vardakis et al., 2016). The model developed for this thesis is the first to model the effects of a pre existing region of oedema using increased porosity and permeability.

Spinal cord models have demonstrated that using a poroelastic rather than an elastic material model yields different results (Støverud et al., 2016a). For the poroelastic solid skeleton a linear elastic model was chosen. However, mechanical behaviour of spinal cord tissue is known to be more complex than this and studies have investigated the suitability of other material models. Cheng and Bilston (2007) found that a poroviscoelastic[1] model captured the behaviour of spinal cord tissue but only evaluated this with low strain rates; following rigorous

---

[1] A poroelastic model with a viscoelastic solid skeleton.

testing Franceschini et al. (2006) found that a poroviscoelastic model was most appropriate for brain tissue and that at low strains poroelasticity was appropriate. Other material models such as viscoelastic and hyperelastic have also been explored (Bilston and Thibault, 1996; Shetye et al., 2014).

Although poroelasticity is a popular method for modelling brain and spinal cord tissues, there are arguments against it. For example, that it cannot fully account for the strong strain stiffening effects seen in CNS tissue tests (Miller, 2000). Strain stiffening effects were not addressed in the present model. The effective stiffness of spinal cord tissue is thought to change with water content, an effect partially incorporated with the use of a poroelastic rather than a solely elastic model. Despite this there were advantages to using a linear elastic solid skeleton in the poroelastic model. Lower computational intensity allowed more simulations to be run which in turn enabled more features of the spinal cord model to be compared (see Chapter 5, Section 5.2). Furthermore many existing poroelastic spinal cord tissue models are quasi-static whereas the model here included dynamic effects. As an examination of the spinal cord cross section in relation to oedema with syringomyelia has not been carried out, initial results from a linear model are a beneficial starting point.

Pressure in the SAS is intrinsically linked to syrinx formation and some intrusive pressure measurements have found that syrinx and nearby SAS pressure remain the same throughout the cardiac cycle. This suggests a path of communication between the spinal cord and SAS. Whether this is via larger pathways such as the PVS or via the ECS of the cord itself is uncertain. The poroelastic model allowed potential communication via the ECS to be explored. Fluid communication between the ECS and spinal cord cells themselves was assumed to be negligible and the solid skeleton was modelled as impermeable. However it has been suggested that fluid movement across the cell boundary could have more of an impact on fluid movement in the CNS than previously thought (Brinker et al., 2014). At present it is not known whether the timescales and volumes of this fluid transport are comparable with fluid transport through the ECS so the assumption of an impermeable solid skeleton is reasonable.

The present model assumed spinal cord ECS was the main fluid pathway and means for pressure changes to propagate through the tissue. Fluid movement in the ECS is thought to be largely diffusive, with little bulk flow in healthy conditions (Brinker et al., 2014). Darcy's law approximates bulk flow with diffusive movement based on fluid pressure. In this respect it is a suitable model for fluid movement in the ECS. Whether ECS fluid movement is diffusive or bulk flow, pressure waves from the SAS still propagate through the cord fluid, affecting the cord tissue in the form of mechanical stress. The poroelastic model allowed the analysis of this potential source of tissue damage.

Although ECF and tissue components were represented with the pore fluid and solid skeleton, fluid compartments such as blood vessels and PVS were neglected. These different fluid compartments in the CNS maintain a dynamic equilibrium along with the SAS fluid, an effect known as the Monro-Kellie hypothesis (Mokri, 2001). Other mathematical models of CNS diseases and injuries have included the interaction between these compartments to evaluate the impact they have on the progression of certain conditions such as hydrocephalus (Eisenträger and Sobey, 2013; Tully et al., 2010; Wirth and Sobey, 2006). The interaction of CSF pressure, blood vessels, PVS and ECF space in the spinal cord is likely to be influential in the pathogenesis of syringomyelia (Clarke et al., 2017) and a multi-compartmental poroelastic model that accounts for this interaction would give a fuller picture of the processes involved.

With the present state of tissue mechanical testing it is difficult to determine the proportion of viscoelastic behaviour that can be attributed to fluid shifting within the ECS, inside cells or to a truly viscoelastic tissue. As all biological tissues have an extremely high fluid content, it is possible that much of this apparent viscoelastic behaviour originates in extra- and intracellular fluid movement. A potential way of capturing this behaviour is with a nested porosity model, where the poroelastic solid skeleton is itself modelled as a poroelastic material. This approach been used with bone tissue (Cowin et al., 2009). In the present model, cellular components of spinal cord tissue were approximated by the solid skeleton and the mechanical behaviour of other non-CNS cells has been shown to be well represented by a poroelastic model (Moeendarbary et al., 2013). Nested porosity has been shown to capture strain stiffening behaviour of other biological tissues (Le Pense and Chen, 2017); strain-stiffening behaviour has been observed in the spinal cord (Koser et al., 2015).

6.2.2 Spinal cord cross section geometry

The poroelastic model was solved on a two dimensional finite element mesh of the spinal cord cross section (Chapter 5, Section 5.1). Two dimensional modelling allowed more detail of the cord cross section to be included, such as NRDL and grey and white matter regions. Studies have shown longitudinal pressure differences along the SAS surrounding an existing syrinx (Klekamp et al., 2001) and in this respect the two dimensional modelling is an oversimplification as longitudinal differences are not represented. However, using a two dimensional plane strain model revealed detailed pressure and stress information on a representative section of the cervical spinal cord when NRDL and grey matter regions were introduced to the model (Chapter 5, Sections 5.2.1 and 5.2.2).

Idealised spinal cord geometry was used to generate the finite element meshes, which is less realistic than using subject-specific geometry based on scan data.

Certain aspects of the mesh were informed by high resolution MRI images presented in Massire et al. (2016) such as overall cross section width and height, NRDL location on the boundary and grey matter shape and size. Mesh dimension was important in the model and the finite element mesh had width and height ~1.3 cm and ~0.8 cm respectively, using larger or smaller meshes affected the model output (not shown). Other poroelastic models of the cord have used anatomically realistic data (Sarntinoranont et al., 2006; Støverud et al., 2016a) however, as these used *ex vivo* or low resolution data they also have inaccuracies. Accurate geometrical information regarding the spinal cord is hard to obtain due to its location within the bony vertebrae, small size and its constant motion with CSF motion and heartbeat (Stroman et al., 2014). With these considerations, the idealised mesh informed by high resolution *in vivo* data was not unreasonable.

The simulations in Chapter 5 modelled a region of oedema located in the posterior white matter. The interstitial oedema that often accompanies syringomyelia or hydrocephalus is known to affect white matter rather than grey matter (Weller, 2014). However oedema has been noted in both the white matter following experimental SCI (Saadoun et al., 2008) and grey matter following induced arachnoid scarring (Klekamp et al., 2001). Furthermore, early studies linking oedema and syringomyelia stated that both spinal cord grey matter and white matter are susceptible to oedema (Feigin et al., 1971). As such it would be beneficial to simulate oedema in different regions of the cord to examine the mechanical effects. The present model has provided an initial investigation into the mechanical role of oedema in syringomyelia cavity formation.

Certain features of spinal cord anatomy were excluded from the model. The fully open CC has been implicated in early syringomyelia theories (Gardner and Angel, 1958; Williams, 1980) although it is now commonly accepted that it is rare for it to remain fully open into adulthood (Milhorat et al., 1994; Petit-Lacour et al., 2000).

In a poroelastic model of the spinal cord, Støverud et al. (2016a) modelled the CC as a small region of greatly increased permeability and found that it had little effect on fluid movement in the grey and white matter. Another similar study found the central canal influenced pressure gradients in the cord (Drøsdal et al., 2013). Not including an open CC in the model is not thought to have greatly affected the results although including it would give an indication of whether a cavity is more likely to form near or in an open section of CC and should be explored with future work.

Including separate tissue properties for grey matter, as opposed to using the same elasticity and fluid transport properties for both grey and white matter, is thought to affect results (Støverud et al., 2016a) particularly in a poroelastic model. Section 5.2.1 showed that grey matter affected pressure and stress in the spinal cord. Despite this, including grey and white matter differences is more likely to impact results in a three dimensional or axisymmetric model; as seen in Chapter 3, the elastic and fluid transport behaviours are more markedly different in the longitudinal direction which is excluded in a two dimensional model.

NRDL were modelled by restraining nodal displacements on the cord boundary. Denticulate ligaments are attached laterally along the entire length of the spinal cord so it is reasonable to include them in any plane strain model. They cross the SAS and attach to the arachnoid mater at intervals along the spinal column (Chapter 1, Figure 1.5), applying slight tension to the spinal cord *in vivo* (Tunturi, 1978). It is uncertain whether the amount of tension applied to a particular cross section of the cord depends on its proximity to where the denticulate ligament attaches to the arachnoid mater. These differences in tension at different spinal levels have not apparently been measured.

A pair of nerve rootlets exits the spinal cord at each spinal level, alternating with locations where the denticulate ligament attaches to the arachnoid mater (Figure

1.5). As such there will be some cord cross sections containing nerve rootlets and others without. Both nerve rootlets and denticulate ligaments were included in the finite element mesh as restrained nodes on the edge of the mesh, the locations for these restraints were informed by the high resolution MRI images of Massire et al. (2016) (Chapter 2, Figure 2.4). With regards to model geometry, Section 5.2.2 showed that NRDL tethering reduced pressure and stress in most areas of the cord cross section and should not be neglected in mechanical models of syringomyelia.

To the author's best knowledge there is no apparent data on where syrinxes form in relation to NRDL or whether indeed there is any correlation between syrinx location and proximity to NRDL tethering. Rather than one long continuous syrinx, some syrinxes show a segmented effect (Figure 6.1) although it is uncertain whether this segmentation occurs in relation to NRDL locations. It would be interesting to examine syringomyelia imaging data for any patterns with regards to syrinx and NRDL location. In the present work, NRDL tethering was found to interact with oedema causing increased stresses (Section 5.2.3); in the model without NRDL, stress was reduced when oedema was introduced.

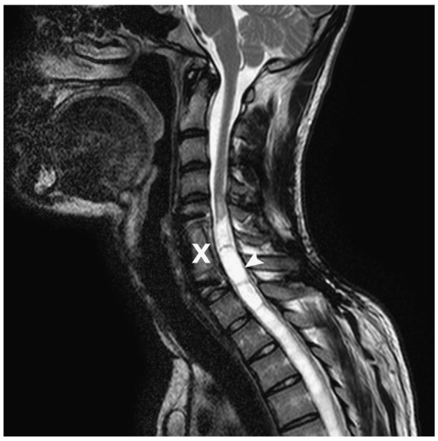

Figure 6.1: A syringomyelia cavity in the neck (arrowhead). The large white cavity region is segmented. (Elliott et al., 2013). *Reproduced with permission.*

6.2.3 Initial and boundary conditions

Initial pressure conditions in the spinal cord ECS were assumed to be zero, however in reality the absolute pressure is non-zero (Heiss et al., 2012). The loading boundary conditions applied to the cord took this into consideration, that is the amplitude of the SAS pressure wave induced by heartbeat was used disregarding the baseline absolute pressure of the SAS. In healthy conditions the pressure difference between the spinal cord and SAS is thought to be small (Klekamp et al., 2001) so modelling both as zero may have a small impact. However, as the cord was modelled as a fully coupled poroelastic material, the initial ECF pressure would provide added stiffness to the very soft spinal cord tissue, so a non-zero initial condition is more accurate.

To fully mimic the conditions surrounding the formation of a syrinx it would be pertinent to have an initial pressure dissociation between the cord ECS pressure and SAS pressure. Heiss et al. (1999) found that syrinx pressure is the same as cervical SAS pressure when measured during surgery, although the ECF pressure was not measured. Some experimental and clinical reports have noted that syrinx pressure may be higher than the surrounding tissue pressure (Brodbelt and Stoodley, 2003; Dong et al., 2016). Although a cavity was not modelled, pressure initial conditions for the region of presyrinx oedema were the same as the surrounding tissue.

Future work to evaluate the influence of increased pressure in the oedema would explore the findings of Dong et al. (2016). In a rat SCI model they found the cord interstitial pressure of control and injured animals to be $\sim 900\,\mathrm{Pa}$ and $\sim 3000\,\mathrm{Pa}$ respectively. There are no apparent poroelastic models of SCI and this threefold increase in ECF pressure would have a significant effect on the stiffness of the tissue in a fully coupled poroelastic model. Comparing different initial pressure conditions using a poroelastic model would give insight into the mechanics of post-SCI syringomyelia.

From a mechanical perspective, the NRDL are effectively flexible tethers and allow the cord to move ~0.5 mm radially in the SAS (Cai et al., 2007). The effect of NRDL in the model were represented by completely restraining the displacement and velocity of nodes on the boundary of the spinal cord where the NRDL join it. This completely restricted movement at these nodes, which is not the case *in vivo*. However, as a fully coupled FSI model was not built, the absolute tethering was a reasonable approximation as the NRDL entry sites remained fixed in relation to the cord.

NRDL apply a slight tension to the cord *in vivo* (Tunturi, 1978) and these effects were neglected in the model. To include these would involve a non-zero strain initial condition; considering that spinal cord tissue is known to exhibit strain stiffening behaviour this suggests that *in situ* the spinal cord is stiffer than the *ex vivo* samples used in experiments. Both non-zero strain initial conditions and the consequent increased Young's modulus of the tissue should be considered in future spinal cord models.

Disrupted CSF pressure in the SAS is thought to be at least partially responsible for syringomyelia cavity development and this was modelled as a boundary condition applied to the edges of the cord cross section. Pressure changes in the SAS are induced by pulse, breathing, movement and actions such as coughing and straining; following SCI or conditions such as CM these pressures become exaggerated (Brodbelt and Stoodley, 2003; Linge et al., 2013). Exaggerated SAS pressures due to pulse were applied to the cord cross section model, pulse was approximated with a cos wave and pressure magnitudes were taken from the literature. The use of simplified pressure loading was largely due to the lack of data in the literature regarding CSF pressure measurements in the spinal SAS and may have reduced accuracy of the model output. *In vivo* SAS pressure data would have been more accurate, such as the measurements of Eide (2008) in the brain. Techniques are being developed to non-invasively calculate relative SAS pressures using MRI techniques (Loth, 2017) which could be applied to future syringomyelia models.

The model simulated a section of the cervical spinal cord; flow velocities in the cervical spinal cord are thought to increase from spinal levels C1 to C4 (see Chapter 1, Figure 1.2) in CM patients (Shah et al., 2011). Due to the Venturi effect this may induce a pressure drop in this region although the extent of this effect is uncertain. Simulating a pressure drop by changing the boundary condition pressure amplitude from $A = 200\,\text{Pa}$ to $A = -200\,\text{Pa}$ revealed that the tension applied to the cord by the pressure drop caused increased tensile stress in the oedema region of the cord (Chapter 5, Figure 5.12).

Pressure boundary conditions were uniformly applied to the edge of the cord cross section, when in reality simultaneous flows in opposite directions around the spinal cord have been observed (Bradley et al., 2016) suggesting pressure applied around the cord cross section is not uniform. These bidirectional flows have been observed in CFD models of the CSF alongside CM (Linge et al., 2013; Støverud et al., 2016b) and arachnoiditis (Cheng et al., 2012). Repeated non-uniform loading on the cord cross section model could increase stresses in particular regions of the cord and would benefit from further exploration.

6.3 Tissue property implications

The detailed analysis of tissue properties given in Chapter 3 provides a resource for other researchers creating poroelastic models of the spinal cord. CNS tissues, as with all biological tissues, are complex materials and the use of purely mechanical models to represent them whilst useful is likely to be a gross oversimplification. Parameter choices for the present model were made taking into account the function and composition of the tissue they described. Despite this, the pressure and stress figures presented in Chapter 5 should not be seen as absolute values.

6.3.1 Elasticity

It is well documented that CNS elasticity values are strongly dependent on the measuring technique and size of sample used, an effect which has itself been the focus of study (Budday et al., 2015). Differentiating between YM values of individual cellular components and the overall tissue sample is important in a poroelastic model, where YM refers only to the solid skeleton. YM values were chosen that were thought to best represent the solid skeleton, that is the cellular components, of spinal cord tissue. Other poroelastic models of CNS tissue have used lower YM values (Bertram and Heil, 2017; Heil and Bertram, 2016), although the values chosen for the present model did not take into account any strain stiffening effects (as in Taylor and Miller (2004)).

Based on existing experimental values such as Ichihara et al. (2001), the grey matter was assigned a stiffer YM value than white matter however there are other tests that show the opposite (see Chapter 3, Table 3.2). Elastography is an *in vivo* technique for measuring tissue elasticity and studies on human brain tissue have found white matter to be stiffer (Johnson et al., 2013). With this in mind, whilst the model YM values with a stiffer grey matter and softer white matter were chosen to be as representative as possible, they cannot be taken as definitive at present. Despite this, the finding that oedema increases compressive stress still holds when the grey matter is modelled as softer (Figure 5.17).

Spinal cord tissue was modelled as slightly compressible with a PR value of $\nu = 0.4$, lower than some existing models (Harris and Hardwidge, 2010; Støverud et al., 2016a). Fluid within the ECS is known to move preferentially along white matter tracts (Abbott, 2004) and this effect is not represented in a two dimensional model. In a three dimensional model the assumption of overall incompressibility ($\nu = 0.5$) is not unreasonable, however in a two dimensional model fluid moving away in the longitudinal direction would lend an effective compressibility ($\nu < 0.5$) to the cross section; the chosen value of $\nu = 0.4$ approximates some of this effect.

The Monro-Kellie hypothesis (that ECF, tissue, blood vessels and CSF volumes maintain a dynamic equilibrium (Mokri, 2001)) suggests the CNS is effectively incompressible ($\nu = 0.5$). As the present model only accounted for ECF and tissue it was not unreasonable to have a compressible spinal cord model with PR $\nu = 0.4$ to compensate for the blood vessel and CSF compartments. Furthermore, comparing different values of PR revealed that both pressure and stress were affected similarly, when PR was increased both compressive stress and pressure decreased (see Section 5.3.3).

Compressibility of the cellular solid skeleton is also affected by fluid leaving and entering the cells from the ECS (Brinker et al., 2014; Hladky and Barrand, 2014), although whether this is rapid enough to have an impact during the timescales modelled is uncertain. Fluid communication to and from the spinal cord and surrounding SAS also affects the effective compressibility of a cord only model, as the volume of ECF changes. PVS are a suggested pathway for this communication to take place (Stoodley et al., 1996) although it is uncertain how fast this can happen. Slightly lowering the PR can compensate for these effects, similar compensation techniques have been explored by Elliott et al. (2017).

Several simplifications were made in choosing appropriate tissue properties. Both grey and white matter were assumed to be isotropic. In three dimensions white matter is almost certainly anisotropic, or at least orthotropic, due to the long bundles of axons that run its length (Sarntinoranont et al., 2006). Elasticity in the radial direction is thought to be more isotropic (Koser et al., 2015) and the assumption of an isotropic YM will detract less in a two dimensional model of the cord cross section. Furthermore, elasticity was considered to be constant across the entire grey or white matter region although it has been suggested that elasticity is slightly different in across regions of the cord cross section (Koser et al., 2015). The NODDI parameters described in Chapter 4 included the mean orientation vector $\boldsymbol{\mu}$, which indicated the direction of fibres in spinal cord tissues (see Figure 6.2). As fibre layout likely influences elasticity this further demonstrates the elastically anisotropic nature of the grey matter cross section.

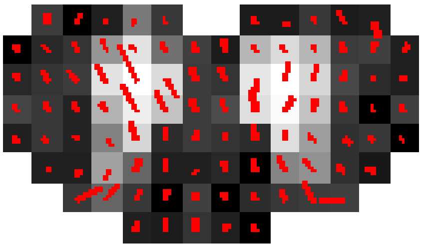

Figure 6.2: NODDI mean orientation vectors (red) indicating the orientation of fibres in the grey and white matter regions. If fibre layout influences YM anisotropy then grey matter is definitely not isotropic as assumed.

Young's modulus is a measure of elasticity that refers to a perfectly elastic material and has long been considered by some as inadequate for representing biological tissue (Fung, 1967; McKee et al., 2011). This partly explains the wide range of spinal cord YM values measured in the literature. Strain stiffening is also responsible as tissue samples are tested at a variety of strains (see Chapter 3, Section 3.2.1). Whilst it was beyond the scope of this project to determine the magnitude and frequency of strain stiffening that occurs in the cord, it can be incorporated into future models for example by using a viscoelastic solid skeleton.

Grey and white matter YM values used were 10 000 Pa and 5000 Pa respectively. Taylor and Miller (2004) have argued that values of the order of 10 000 Pa are too high and relate to a higher strain rate than the CNS is commonly exposed to. However, the spinal cord is held in slight tension *in vivo* (Tunturi, 1978) and this would incur a certain amount of strain stiffening. With this in mind the slightly higher values chosen are reasonable.

6.3.2 DW-MRI technique

The method presented in Chapter 4 for obtaining spinal cord permeability and porosity values provided the foundation of an alternative tissue testing technique. Porosity and permeability values were derived from DW-MRI data (originally obtained by Grussu et al. (2015)) that had been analysed using the NODDI technique (see Chapter 4, Section 4.2). DW-MRI data had been acquired from four subjects. For future developments of the technique a larger sample size would be beneficial. Despite the limitations, the clear benefits of a DW-MRI based method are its non-invasive nature and potential to be applied clinically. To date, the vast majority of techniques for measuring spinal cord permeability and porosity require using intrusive methods (Nicholson and Syková, 1998; Syková and Nicholson, 2008).

Besides their utility in the syringomyelia model described in this thesis, the porosity and permeability values obtained are beneficial in other research areas. Models of the spinal cord often note the lack of porosity and permeability data (Harris and Hardwidge, 2010; Sarntinoranont et al., 2003) and the preliminary results in Chapter 4, Section 4.4 contribute to what is already known about fluid transport in the spinal cord (see Chapter 3, Table 3.3). These results from healthy subjects have the potential to be used as a baseline with which to compare results from patients susceptible to syringomyelia. Absolute porosity and permeability values would not necessarily be required to make this comparison, as long as errors generated by the method were consistent across subjects. Finally, this technique could also be applied to brain tissue to obtain parameters for poroelastic brain tissue models, as used in hydrocephalus (Wirth and Sobey, 2006) and drug delivery (Chen and Sarntinoranont, 2007).

There are however drawbacks and refinements to the technique. First and foremost is the scarcity of existing spinal cord porosity and permeability data with which to compare these results. An alternative way of verifying the technique would be to evaluate the porosity and permeability of CNS phantom materials (such as in Ivanchenko et al. (2010)). As some physical properties of these materials (for example fibre diameter or even permeability) could be measured beforehand using invasive techniques, this could be used to verify the porosity and permeability values revealed by the DW-MRI technique. It would be wrong to assume that results from a non-biological material could completely verify a technique designed for biological tissue, however it could provide an indication of its accuracy.

Other studies have used DW-MRI to obtain structural and fluid transport information regarding the spinal cord. For example the size of ECS in *ex vivo* porcine tissue (Koch and Finsterbusch, 2008), the volume fraction and fibre direction of *ex vivo* rat spinal cord (Sarntinoranont et al., 2006) and *in vivo* human brain (Shahim et al., 2010). The method presented in Chapter 4 builds upon these by presenting a method for obtaining *in vivo* human spinal cord data. A potential future benefit of a non-invasive technique for characterising spinal cord porosity and permeability is the ability to evaluate how fluid volume and movement within the cord is affected by movement, exertion, respiration, pulse and other physiological processes.

At present the technique does not fully exploit the data provided by NODDI analysis, in particular the mean orientation vector $\boldsymbol{\mu}$. The anisotropic permeability tensors were not truly anisotropic as it was assumed that white matter fibres lay strictly parallel to the z axis and the permeability values κ_{pe} and κ_{pa} lay perpendicular and parallel to this direction respectively. In reality $\boldsymbol{\mu}$ was orientated differently for each voxel; white matter and to a lesser extent grey matter are known to have aligned as well as crossing axons (Bilston, 2016). As the κ_{pe} and κ_{pa} values found were perpendicular and parallel to $\boldsymbol{\mu}$, a method for translating these to the z axis would be more accurate and would generate truly anisoptropic rather than orthotropic permeability tensors.

One of the main limitations of the present technique was the tendency to overestimate porosity (ϕ) values. Whilst CNS porosity values in the literature are often $\sim$0.2, the values derived in Chapter 4 were $\sim$0.4. Porosity was calculated using the intracellular volume fraction $\phi \approx 1 - \nu_{in}$. This attributed any tissue volume which did not contain large regions of fluid ν_{iso} (such as the central canal and larger blood vessels) or tissue fibres ν_{in} to the region described by ϕ Zhang et al. (2012). As smaller blood vessels were not included in either ν_{in} or ν_{iso} these likely caused an increase in the calculated porosity value. In the poroelastic spinal cord model porosity was defined as the region containing ECF and blood vessels were included in the solid skeleton volume. As such the use of smaller 0.2 porosity values in the simulations presented in Chapter 5, rather than calculated porosity values was not unreasonable.

Other factors that plausibly contributed to the high porosity value include PVS and myelin. Fluid within PVS could contribute to the porosity for similar reasons as smaller blood vessels. White matter contains a high volume of myelin which would also contribute to the high porosity value. Myelin is invisible to DW-MRI although there are techniques for quantifying the volume of myelin in white matter

(Stikov et al., 2015); combining this with the present technique would give a more accurate picture of tissue porosity. The NODDI extracellular volume fraction ν_{en} includes glial cells and cell bodies (Zhang et al., 2012), consequently these also contributed to the calculated porosity value. Grey matter was found to have a higher porosity than white matter (0.45 and 0.4 respectively). There is a heavier concentration of blood vessels in the grey matter (Bilston, 2016) which could be the reason, along with the smaller amount of myelin, for the higher porosity values found in grey matter in Chapter 4.

As permeability was calculated using this overestimated porosity, the reliability of the resulting permeability tensors is questionable. An option for overcoming this limitation is to introduce a compensation technique to the porosity calculation, whereby the volume of blood, myelin, glial cells, PVS fluid or cell bodies that are included in ν_{en} are quantified and subtracted from the ϕ value. There is limited information on this in the literature.

White matter permeability values were calculated based on an assumed hexagonal fibre arrangement. The organisation of fibres is thought to strongly influence DW-MRI data (Novikov et al., 2014), although precisely how this would influence the calculated permeability it uncertain. Fibre radii used in the permeability calculation equations were taken from the literature, a single value was used for grey and for white matter. In reality tissue fibres have a range of radii which would also affect the permeability of tissue. To conclude, there were several limitations and assumptions inherent in these calculations, however the foundations of a non-invasive method for determining spinal cord porosity and permeability using DW-MRI data have been described.

6.3.3 Fluid transport

Grey and white matter fluid transport properties were calculated using the DW-MRI data. Oedema porosity was taken from the literature (Syková and Nicholson, 2008) and its permeability was calculated using the technique in Chapter 4. Several factors affect the porosity and permeability of a material. Tortuosity is a dimensionless number that characterises how fluid transport is hindered by the microstructure of a material (Nicholson and Syková, 1998). It was not considered in the permeability calculations; this is something that should be considered in future work. Blood vessels were neither modelled nor taken into account in the porosity value. The extent to which this affected results is likely to be small as the model was only representing tissue cells and ECS, not the entire blood, tissue, CSF and ECF system. Finally, the equations used to calculate permeability were based on bulk flow through fibrous materials (see Chapter 4, Section 4.3) and it is uncertain how much bulk flow occurs within the spinal cord ECS. However, it has been found that in certain circumstances (such as fluid moving towards a syrinx (Wong et al., 2012)) and oedema (Reulen et al., 1977), bulk flow can occur in the spinal cord.

Each voxel of NODDI scan data yielded a porosity and permeability value, however these regional differences across the spinal cord cross section (see Figure 6.3 for scale) were not included in the finite element model. Primarily this was due to the exploratory nature of the porosity and permeability calculation technique, as the field of non-invasive mechanical characterisation of CNS tissues is still developing. It was uncertain how reliable the regional differences were, therefore including them in the finite element simulations may not have been useful at this stage. Furthermore, there are challenges to imaging the spinal cord itself such as its small size, location within the bony vertebrae and susceptibility to movement (Wheeler-Kingshott et al., 2014). As imaging techniques progress, along with the methods for deriving suitable poroelastic parameters, regional porosity and permeability differences can be used in finite element models.

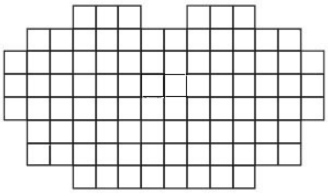

Figure 6.3: Voxel size ($1 \times 1 \times 5\,\text{mm}^3$) with respect to the human cervical spinal cord cross section.

Constant porosity and permeability were assumed, whilst *in vivo* they are likely to be variable. Variable porosity and permeability have not apparently been included in a spinal cord model although strain dependent permeability has been used in models of the brain (Eisenträger, 2012). Any deformation of grey or white matter may alter the size and shape of the ECS thereby affecting the porosity and permeability of the tissue. As such, CNS fluid transport is highly likely to be strain dependent unlike the constant values chosen here. However, due to the scarcity of spinal cord fluid transport data and the relative rarity of poroelastic spinal cord models, constant porosity and permeability are a reasonable assumption which can be improved in future iterations of the model.

The inverse Biot modulus in the pore fluid governing equation (see Chapter 2, Equation (2.19)) was set to $\frac{1}{M_b} = 0.0001$ for all tissue types in the simulations. This was due to the prohibitively small time step required to run the simulations with more realistic values (simulations took approximately 9 days to run). The definition of the Biot modulus $M_b = \frac{K_s}{\alpha(1-\alpha)}$ given in Chapter 3, Section 3.2.5 results in much smaller values of $\frac{1}{M_b}$ that differ according to the bulk modulus of the tissue and the Biot-Willis coefficient α (see Table 6.1). Comparing the effects of more realistic values of $\frac{1}{M_b}$ demonstrated the relevance of accurate poroelastic parameters in a spinal cord tissue model and confirms that this should be considered in future models of syringomyelia (see Section 5.3.4).

Table 6.1: Values of the inverse Biot Modulus $\frac{1}{M_b}$ for different tissue regions and Biot-Willis coefficients α.

	$\boldsymbol{\alpha = 0.9995}$	$\boldsymbol{\alpha = 0.95}$	$\boldsymbol{\alpha = 0.8}$
White matter	6×10^{-8}	5.7×10^{-6}	1.92×10^{-5}
Grey matter	3×10^{-8}	2.85×10^{-6}	9.6×10^{-6}
Oedema	6×10^{-8}	5.7×10^{-6}	1.92×10^{-5}

6.4 Future work

This thesis has highlighted several avenues of research that would contribute to the understanding of how syringomyelia cavities form. The natural extension of the plane strain poroelastic model presented here is a three dimensional cord model. Primarily this would provide a better representation of the spinal cord, but furthermore the anisotropic elasticity and permeability properties described in Chapters 3 and 4 have a greater difference in the longitudinal direction. Combining the spinal cord model with a CFD model of the surrounding CSF would allow the interaction between the spinal cord and CSF to be explored further.

One current area of syringomyelia research is examining the role of blood, PVS, ECF and CSF interaction in syringomyelia cavity formation, for example in Clarke et al. (2017). A more detailed tissue model, such as the nested poroelasticity described by Cowin et al. (2009) or the multi-compartmental brain tissue model of Vardakis et al. (2016), would allow the effects of this interaction on the spinal cord tissue to be studied in more detail.

The finding that oedema contributes to mechanical stress in the spinal cord partially explains how presyrinx oedema contributes to cavity formation. It would be useful to know where presyrinx oedema is more likely to form in relation to the site of CSF disruption; a review of clinical syringomyelia images would provide insight into this. Further simulations comparing the effects of oedema in different regions of the cord would give insight into how this affects stress in the spinal cord tissue.

Potential biochemical factors of syringomyelia, such as the water transport protein AQP4, are the focus of some current syringomyelia research (Saadoun et al., 2008). Incorporating these factors into the poroelastic model via multiscale modelling such as in Vardakis et al. (2016) would provide insight into how mechanical and biochemical factors contribute to cavity formation.

Finally, the ultimate aim of a mathematical model of syringomyelia is to provide insight that will be useful for understanding and treating the clinical condition. Applying the DW-MRI technique to patient data, and combining these findings with a more sophisticated spinal cord model, would give further insight into syringomyelia cavity formation and growth.

6.5 Conclusion

Syringomyelia is a rare spinal cord condition associated with a wide variety of injuries, diseases and congenital conditions that affect the CNS (Bogdanov, 2014). Whilst a common factor amongst all these is a disruption of CSF flow in the SAS surrounding the cord, how this causes a syringomyelia cavity to form remains uncertain. In this thesis a poroelastic finite element model of a section of the cervical spinal cord has been built to examine how tissue stress and ECF pressure is affected by external CSF pressure, to better understand how CSF disruption could lead to cavity formation. The model has been improved using elastic and poroelastic tissue properties from the literature and from a preliminary technique to derive spinal cord porosity and permeability properties from DW-MRI data.

Based on the results presented in Chapter 5 it can be concluded that mechanical factors such as stress may be at least partially responsible for cavity formation. Furthermore, the presence of tissue oedema which is often found preceding cavity formation (Fischbein et al., 2000), increased stress in the spinal cord providing a link between presyrinx oedema and cavity formation from a mechanical viewpoint. Nerve roots and denticulate ligaments (NRDL) tether the cord in approximately the centre of the spinal canal and including NRDL tethering in the model reduced stress and pressure across the spinal cord cross section. Introducing a region of grey matter to the cord model similarly altered stress and pressure distribution in the spinal cord. However, as there is still disagreement surrounding the difference between grey and white matter material properties these alterations should not be seen as absolute. Spinal cord porosity and permeability values were derived from DW-MRI data and demonstrated that DW-MRI has the potential for determining spinal cord parametric data suitable for use in mathematical models.

At present, techniques for measuring spinal cord porosity and permeability have involved tracers or other invasive methods. Whilst not a direct measurement technique, the method presented here for deriving spinal cord parameters from DW-MRI data presents an alternative, non-invasive method for acquiring parameters suitable for use in mathematical models. Furthermore, results showed that the common modelling assumption that grey matter is isotropic is not necessarily the case.

A plane strain model that examines the cervical spinal cord cross section in detail has been developed; NRDL have not previously been included in a model of syringomyelia and including different properties for grey and white matter is uncommon. The results imply that these anatomical features should not be neglected in future tissue models of syringomyelia. A detailed consideration of the poroelastic properties of the spinal cord is also uncommon. Whilst oedema is associated with syringomyelia, the mechanical role of oedema in syrinx formation has not previously been examined or modelled. Results showed that external CSF pressure causes higher stresses in the cord when oedema is present.

Finding that oedema increases both compressive and tensile stress in the spinal cord is significant for future syringomyelia research, as increased stress may present a means for a cavity to form or for an existing cavity to worsen. Furthermore the implications of this finding are to provide a modelling foundation, and persuasive justification, for future research into the role of presyrinx oedema in syringomyelia cavity formation. Tissue focussed syringomyelia models are becoming more popular; development of the poroelastic spinal cord model and scrutiny of the elastic and poroelastic parameters required for the model has contributed to the development of future spinal cord tissue models.

As with any mathematical model of a biological system, there were limitations in the methods used. Spinal cord tissue was modelled using a linear poroelastic model; the spinal cord is much more complex than a two phase solid/fluid material. However, poroelasticity provides a means to calculate extracellular fluid pressure and the effects that it has on stress in the cord. Stress in the cord tissue was taken to be an indicator of tissue damage and therefore syrinx formation. At present there is no information regarding levels of stress in the spinal cord that could cause damage so it is not currently possible to determine at what external CSF pressure a cavity is likely to form. The usefulness of the model was restricted by the inherent complexity of accurately measuring tissue parameters. As such the results were an indication of how spinal cord tissue behaves when external CSF pressure is applied rather than providing absolute pressure or stress values. Nevertheless the work presented here is an efficient non-invasive method for understanding the factors that contribute to syringomyelia cavity formation.

Presyrinx oedema has been noted clinically and in experimentally induced cases of syringomyelia and is used to indicate potential syrinx formation (Ross and

Moore, 2015) yet its role in cavity formation has not been thoroughly investigated. Recent syringomyelia research has suggested that non-invasive treatments to improve water transport in the cord could reduce the likelihood of syringomyelia (Saadoun et al., 2008) and the work of this thesis supports this from a mechanical perspective.

The present work has provided a useful insight into syrinx formation and modelling and has highlighted several avenues for future work. Future developments of the spinal cord tissue model, such as including viscoelastic effects, would improve fidelity of the output to *in vivo* tissue behaviour. Refining the DW-MRI based technique to fully exploit the microstructural information provided by NODDI analysis would provide better parameters and improve the model. The interplay between syringomyelia, the water transport protein AQP4 and stress in the cord would benefit from further investigation and a multiscale mathematical model that includes biochemical factors would deepen the understanding of processes that take place in the cord prior to and during syringomyelia cavity formation. The present work provides a foundation for such a model and has outlined the challenges faced when modelling the spinal cord.

Bibliography

N. J. Abbott. Evidence for bulk flow of brain interstitial fluid: Significance for physiology and pathology. *Neurochemistry International*, 45(4):545–552, 2004.

Y. Akiyama, I. Koyanagi, K. Yoshifuji, T. Murakami, T. Baba, Y. Minamida, T. Nonaka, and K. Houkin. Interstitial spinal-cord oedema in syringomyelia associated with Chiari type 1 malformations. *Journal of Neurology, Neurosurgery & Psychiatry*, 79(10):1153–1158, 2008.

F. O. Alpak and M. F. Wheeler. A supercoarsening multigrid method for poroelasticity in 3D coupled flow and geomechanics modeling. *Computational Geosciences*, 16(4):953–974, 2012.

C. G. Armstrong, W. M. Lai, and V. C. Mow. An analysis of the unconfined compression of articular cartilage. *Journal of Biomechanical Engineering*, 106 (2):165, 1984.

Y. Assaf, T. Blumenfeld-Katzir, Y. Yovel, and P. J. Basser. AxCaliber: A method for measuring axon diameter distribution from diffusion MRI. *Magnetic Resonance in Medicine*, 59(6):1347–1354, 2008.

T. W. Barber, J. A. Brockway, and L. S. Higgins. The density of tissues in and about the head. *Acta Neurologica Scandinavica*, 46(1):85–92, 1970.

P. J. Basser and E. Özarslan. Anisotropic diffusion: From the apparent diffusion coefficient to the apparent diffusion tensor. In D. Jones, editor, *Diffusion MRI: Theory, Methods, and Applications*, chapter 6, pages 79–91. Oxford University Press, New York, 2011.

P. J. Basser and E. Özarslan. Introduction to diffusion MR. In H. Johansen-Berg and T. E. J. Behrens, editors, *Diffusion MRI: From Quantitative Measurement to In Vivo Neuroanatomy*, chapter 1. Elsevier, 2nd edition, 2014.

U. Batzdorf. Historical Aspects. In G. Flint and C. Rusbridge, editors, *Syringomyelia: A Disorder of CSF Circulation*. Springer, 2014.

U. Batzdorf, J. Klekamp, and P. Johnson. A critical appraisal of syrinx cavity shunting procedures. *Journal of Neurosurgery*, 89(3):382–388, 1998.

C. D. Bertram. A numerical investigation of waves propagating in the spinal cord and subarachnoid space in the presence of a syrinx. *Journal of Fluids and Structures*, 25(7):1189–1205, 2009.

C. D. Bertram. Evaluation by fluid/structure-interaction spinal-cord simulation of the effects of subarachnoid-space stenosis on an adjacent syrinx. *Journal of Biomechanical Engineering*, 132(6), 2010.

C. D. Bertram and M. Heil. A poroelastic fluid/structure-interaction model of the spinal cord and surrounding structures with a cord syrinx and associated stenosis of the subarachnoid space. In *Proceedings of the 2015 Summer Biomechanics, Bioengineering and Biotransport Conference*, Snowbird, Utah, 2015.

C. D. Bertram and M. Heil. A poroelastic fluid/structure-interaction model of cerebrospinal fluid dynamics in the cord with syringomyelia and adjacent subarachnoid-space stenosis. *Journal of Biomechanical Engineering*, 139(1), 2017.

C. D. Bertram, L. E. Bilston, and M. A. Stoodley. Tensile radial stress in the spinal cord related to arachnoiditis or tethering: A numerical model. *Medical & Biological Engineering & Computing*, 46(7):701–707, 2008.

L. E. Bilston. *The Biomechanics of the Spinal Cord during Traumatic Spinal Cord Injury.* PhD thesis, University of Pennsylvania, 1994.

L. E. Bilston. The effect of perfusion on soft tissue mechanicalproperties: A computational model. *Computer Methods in Biomechanics and Biomedical Engineering*, 5(4):283–290, 2002.

L. E. Bilston. The Influence of Microstructure on Neural Tissue Mechanics. In G. S. Kassab and M. S. Sacks, editors, *Structure-Based Mechanics of Tissues and Organs*, chapter 1, pages 1–14. Springer, 2016.

L. E. Bilston and L. E. Thibault. The mechanical properties of the human cervical spinal cord in vitro. *Annals of Biomedical Engineering*, 24(S1):67–74, 1996.

L. E. Bilston, D. F. Fletcher, A. R. Brodbelt, and M. A. Stoodley. Arterial pulsation-driven cerebrospinal fluid flow in the perivascular space: A computational model. *Computer Methods in Biomechanics and Biomedical Engineering*, 6(4):235–241, 2003.

L. E. Bilston, D. F. Fletcher, and M. A. Stoodley. Focal spinal arachnoiditis increases subarachnoid space pressure: A computational study. *Clinical Biomechanics*, 21(6):579–584, 2006.

L. E. Bilston, M. A. Stoodley, and D. F. Fletcher. The influence of the relative timing of arterial and subarachnoid space pulse waves on spinal perivascular cerebrospinal fluid flow as a possible factor in syrinx development. *Journal of Neurosurgery*, 112(4):808–813, 2010.

M. A. Biot. General theory of three-dimensional consolidation. *Journal of Applied Physics*, 12(2):155–164, 1941.

M. A. Biot. Theory of propagation of elastic waves in a fluidsaturated porous solid. I. Lowfrequency range. *The Journal of the Acoustical Society of America*, 28(2):168–178, 1956.

I. G. Bloomfield, I. H. Johnston, and L. E. Bilston. Effects of proteins , blood cells and glucose on the viscosity of cerebrospinal fluid. *Pediatric Neurosurgery*, 28(5):246–251, 1998.

E. Bogdanov. Epidemiology. In G. Flint and C. Rusbridge, editors, *Syringomyelia: A Disorder of CSF Circulation*. Springer, 2014.

A. Bower. *Applied Mechanics of Solids*. CRC Press, 2010.

W. G. Bradley, V. Haughton, and K.-A. Mardal. Cerebrospinal fluid flow in adults. In J. C. Masdeu and R. G. González, editors, *Handbook of Clinical Neurology, Vol.135*, chapter 28. Elsevier, 2016.

T. Brinker, E. Stopa, J. Morrison, and P. Klinge. A new look at cerebrospinal fluid circulation. *Fluids and Barriers of the CNS*, 11(10), 2014.

A. R. Brodbelt. The Biochemistry of Syringomyelia. In G. Flint and C. Rusbridge, editors, *Syringomyelia: A Disorder of CSF Circulation*, pages 261–278. Springer, 2014.

A. R. Brodbelt and M. A. Stoodley. Post-traumatic syringomyelia: a review. *Journal of Clinical Neuroscience*, 10(4):401–408, 2003.

S. Budday, R. Nay, R. de Rooij, P. Steinmann, T. Wyrobek, T. C. Ovaert, and E. Kuhl. Mechanical properties of gray and white matter brain tissue by indentation. *Journal of the Mechanical Behavior of Biomedical Materials*, 46: 318–330, 2015.

J. Cai, K. Sheng, J. P. Sheehan, S. H. Benedict, J. M. Larner, and P. W. Read.

Evaluation of thoracic spinal cord motion using dynamic MRI. *Radiotherapy and Oncology*, 84(3):279–282, 2007.

M. Catala. Embryonic and fetal development of structures associated with the cerebro-spinal fluid in man and other species. *Archives d'Anatomie et de Cytologie Pathologiques*, 46(3):153–169, 1998.

S. Chakrabortty, N. Tamaki, K. Ehara, and C. Ide. Experimental syringomyelia in the rabbit: An ultrastructural study of the spinal cord tissue. *Neurosurgery*, 35(6):1112–1120, 1994.

H. S. Chang and H. Nakagawa. Hypothesis on the pathophysiology of syringomyelia based on simulation of cerebrospinal fluid dynamics. *Journal of Neurology, Neurosurgery & Psychiatry*, 74(3):344–347, 2003.

D. Chapelle, J. Sainte-Marie, J.-F. Gerbeau, and I. Vignon-Clementel. A poroelastic model valid in large strains with applications to perfusion in cardiac modeling. *Computational Mechanics*, 46(1):91–101, 2010.

X. Chen and M. Sarntinoranont. Biphasic finite element model of solute transport for direct infusion into nervous tissue. *Annals of Biomedical Engineering*, 35 (12):2145–2158, 2007.

X. Chen, K. Sase, A. Konno, and T. Tsujita. Identification of mechanical properties of brain parenchyma for brain surgery haptic simulation. In *Proceedings of the 2014 IEEE International Conference on Robotics and Biomimetics*, pages 1656–1661, Bali, Indonesia, 2014.

A. H. D. Cheng. *Poroelasticity.* Theory and Applications of Transport in Porous Media. Springer International Publishing, 2016.

S. Cheng and L. E. Bilston. Unconfined compression of white matter. *Journal of Biomechanics*, 40(1):117–124, 2007.

S. Cheng, E. C. Clarke, and L. E. Bilston. Rheological properties of the tissues of the central nervous system: A review. *Medical Engineering & Physics*, 30 (10):1318–1337, 2008.

S. Cheng, M. A. Stoodley, J. Wong, S. Hemley, D. F. Fletcher, and L. E. Bilston. The presence of arachnoiditis affects the characteristics of CSF flow in the spinal subarachnoid space: A modelling study. *Journal of Biomechanics*, 45 (7):1186–1191, 2012.

S. Cheng, D. Fletcher, S. Hemley, M. Stoodley, and L. Bilston. Effects of fluid structure interaction in a three dimensional model of the spinal subarachnoid space. *Journal of Biomechanics*, 47(11):2826–2830, 2014.

B. Chikly and J. Quaghebeur. Reassessing cerebrospinal fluid (CSF) hydrodynamics: A literature review presenting a novel hypothesis for CSF physiology. *Journal of Bodywork and Movement Therapies*, 17(3):344–354, 2013.

E. C. Clarke, S. Cheng, and L. E. Bilston. The mechanical properties of neonatal rat spinal cord in vitro, and comparisons with adult. *Journal of Biomechanics*, 42(10):1397–1402, 2009.

E. C. Clarke, D. F. Fletcher, M. A. Stoodley, and L. E. Bilston. Computational fluid dynamics modelling of cerebrospinal fluid pressure in Chiari malformation and syringomyelia. *Journal of Biomechanics*, 46(11):1801–9, 2013.

E. C. Clarke, D. F. Fletcher, and L. E. Bilston. Sustained high-pressure in the spinal subarachnoid space while arterial expansion is low may be linked to syrinx development. *Computer Methods in Biomechanics and Biomedical Engineering*, 20(5):457–467, 2017.

O. Coussy. *Poromechanics*. John Wiley & Sons Ltd, Chichester, UK, 2004.

S. C. Cowin, G. Gailani, and M. Benalla. Hierarchical poroelasticity: Movement of interstitial fluid between porosity levels in bones. *Philosophical Transactions: Mathematical, Physical and Engineering Sciences*, 367(1902):3401–3444, 2009.

M. Czyz, K. Scigala, W. Jarmundowicz, and R. Beidziński. The biomechanical analysis of the traumatic cervical spinal cord injury using finite element approach. *Acta of Bioengineering and Biomechanics*, 10(1):43–54, 2008.

E. Detournay and A. H.-D. Cheng. Fundamentals of Poroelasticity. In C. Fairhurst, editor, *Comprehensive Rock Engineering: Principles, Practice and Projects*, volume II, chapter 5, pages 113–171. Pergamon Press, 1993.

X. Dong, D. Yang, J. Li, C. Liu, M. Yang, L. Du, R. Gu, A. Hu, and H. Zhang. Intramedullary pressure changes in rats after spinal cord injury. *Spinal Cord*, 54(11):947–950, 2016.

S. Dreha-Kulaczewski, A. A. Joseph, K.-D. Merboldt, H.-C. Luwig, J. Gärtner, and J. Frahm. Inspiration is the major regulator of human CSF flow. *Journal of Neuroscience*, 35(6):2485–2491, 2015.

I. N. Drøsdal. *Porous and Viscous Modeling of Cerebrospinal Fluid Flow in the Spinal Canal Associated with Syringomyelia.* PhD thesis, University of Oslo, 2011.

I. N. Drøsdal, K.-A. Mardal, K. Støverud, and V. Haughton. Effect of the central canal in the spinal cord on fluid movement within the cord. *The Neuroradiology Journal*, 26(5):585–590, 2013.

T. Duval, J. A. McNab, K. Setsompop, T. Witzel, T. Schneider, S. Y. Huang, B. Keil, E. C. Klawiter, L. L. Wald, and J. Cohen-Adad. In vivo mapping of human spinal cord microstructure at 300mT/m. *NeuroImage*, 118:494–507, 2015.

P. K. Eide. Comparison of simultaneous continuous intracranial pressure (ICP) signals from ICP sensors placed within the brain parenchyma and the epidural space. *Medical Engineering and Physics*, 30(1):34–40, 2008.

A. Eisenträger. *Finite Element Simulation of a Poroelastic Model of the CSF System in the Human Brain during an Infusion Test.* PhD thesis, St John's College, University of Oxford, 2012.

A. Eisenträger and I. Sobey. Multi-fluid poroelastic modelling of CSF flow through the brain. In C. Hellmich, B. Pichler, and D. Adam, editors, *Poromechanics V: Proceedings of the Fifth Biot Conference on Poromechanics*, pages 2148–2157, Vienna, Austria, 2013. American Society of Civil Engineers.

N. S. Elliott, A. D. Lucey, D. A. Lockerby, and A. R. Brodbelt. Fluid-structure interactions in a cylindrical layered wave guide with application in the spinal column to syringomyelia. *Journal of Fluids and Structures*, 70:464–499, 2017.

N. S. J. Elliott. Syrinx fluid transport: Modeling pressure-wave-induced flux aacross the spinal pial membrane. *Journal of Biomechanical Engineering*, 134 (3), 2012.

N. S. J. Elliott, D. A. Lockerby, and A. R. Brodbelt. A lumped-parameter model of the cerebrospinal system for investigating arterial-driven flow in posttraumatic syringomyelia. *Medical Engineering & Physics*, 33(7):874–882, 2011.

N. S. J. Elliott, C. D. Bertram, B. A. Martin, and A. R. Brodbelt. Syringomyelia: A review of the biomechanics. *Journal of Fluids and Structures*, 40:1–24, 2013.

N. S. J. Elliott, D. A. Lockerby, A. D. Lucey, and A. R. Brodbelt. Syringomyelia and the fluid-structure interactions of a cerebrospinal waveguide. In *Proceedings of the ASME 2014 Pressure Vessels and Piping Conferences*, Anaheim, California, 2014. ASME.

D. R. Enzmann, J. O. O'Donohue, J. B. Rubin, L. Shuer, P. Cogen, and G. Silverberg. CSF pulsations within nonneoplastic spinalcord cysts. *American Journal of Neuroradiology*, 1987.

I. Feigin, J. Ogata, and G. Budzilovich. Syringomyelia: the role of edema in its pathogenesis. *Journal of Neuropathology & Experimental Neurology*, 30(2): 216–32, 1971.

J. C. Fiala, J. Spacek, and K. M. Harris. Dendrite structure. In G. Stuart, N. Spruston, and M. Häusser, editors, *Dendrite*, chapter 1. Oxford University Press, New York, 2nd edition, 2008.

R. J. Fiford and L. E. Bilston. The mechanical properties of rat spinal cord in vitro. *Journal of Biomechanics*, 38(7):1509–1515, 2005.

C. R. Figley and P. W. Stroman. Investigation of human cervical and upper thoracic spinal cord motion: Implications for imaging spinal cord structure and function. *Magnetic Resonance in Medicine*, 58(1):185–189, 2007.

N. J. Fischbein, W. P. Dillon, C. Cobbs, and P. R. Weinstein. The presyrinx state: Is there a reversible myelopathic condition that may precede syringomyelia? *Neurosurgical Focus*, 8(3), 2000.

G. Flint. Post-traumatic and post-inflammatory syringomyelia. In G. Flint and C. Rusbridge, editors, *Syringomyelia: A Disorder of CSF Circulation*, chapter 11, pages 167–184. Springer, 2014.

G. Flint and C. Rusbridge, editors. *Syringomyelia: A Disorder of CSF Circulation*. Springer, 2014.

G. Franceschini, D. Bigoni, P. Regitnig, and G. A. Holzapfel. Brain tissue deforms similarly to filled elastomers and follows consolidation theory. *Journal of the Mechanics and Physics of Solids*, 54(12):2592–2620, 2006.

Y. C. Fung. Elasticity of soft tissues in simple elongation. *The American Journal of Physiology*, 213(6):1532–1544, 1967.

J. A. Gadde, V. Shah, G. B. Liebo, G. A. Ringstad, I. J. Pomeraniec, S. J. Bakke, R. Fric, A. Ksendzovsky, J. A. Jane Jr, E. S. Schwartz, and V. Haughton. Anatomical features of the cervical spinal canal in Chiari I deformity with presyrinx : A case-control study. *The Neuroradiology Journal*, 30(5):405–409, 2017.

F. Gaillard. Case courtesy of Prof Frank Gaillard, Radiopaedia.org, rID: 2592, 2008. URL `https://radiopaedia.org/cases/chiari-i-malformation-7`.

W. Gardner and J. Angel. The cause of syringomyelia and its surgical treatment. *Cleveland Clinic Quarterly*, 25(1):4–8, 1958.

N. Gauge, B. Zebian, A. Hoey, and S. Bassi. Chiari I malformation, syringomyelia and liver disease: An unusual resolution with implications for clinical practice. *Clinical Neurology and Neurosurgery*, 114(6):686–688, 2012.

B. Gebart. Permeability of unidirectional reinforcements for RTM. *Journal of Composite Materials*, 26(8):1100–1133, 1992.

C. Geuzaine and J. F. Remacle. Gmsh: A three-dimensional finite element mesh generator with built-in pre- and post-processing facilities. *International Journal for Numerical Methods in Engineering*, 79(11):1309–1331, 2009.

D. Greitz. Unraveling the riddle of syringomyelia. *Neurosurgical Review*, 29(4): 251–264, 2006.

F. Grussu, T. Schneider, H. Zhang, D. C. Alexander, and C. A. M. Wheeler-Kingshott. Neurite orientation dispersion and density imaging of the healthy cervical spinal cord in vivo. *NeuroImage*, 111:590–601, 2015.

D. B. Hackney, R. Asato, P. M. Joseph, M. J. Carvlin, J. T. McGrath, R. I. Grossman, E. A. Kassab, and D. DeSimone. Hemorrhage and edema in acute spinal cord compression: Demonstration by MR imaging. *Radiology*, 161(2): 387–390, 1986.

C. Hardwidge. Hurstwood Park Neurological Unit, 2014.

P. J. Harris and C. Hardwidge. A porous finite element model of the motion of the spinal cord. In C. Constanda and M. E. Pérez, editors, *Integral Methods in Science and Engineering, Volume 2*, pages 193–201. Birkhäuser Boston, 2010.

D. E. Harrison, R. Cailliet, D. D. Harrison, S. J. Troyanovich, and S. O. Harrison. A review of biomechanics of the central nervous system - Part 1: Spinal canal deformations caused by changes in posture. *Journal of Manipulative and Physiological Therapeutics*, 22(4):227–234, 1999.

D. M. Harwell, J. L. Gibson, R. D. Fessler, J. Holtz, D. B. Pettigrew, and C. Kuntz. Pia mater significantly contributes to spinal cord intraparenchymal pressure in a simulated model of edema. *Spine*, 41(9):E524–E529, 2016.

M. Heil and C. D. Bertram. A poroelastic fluid-structure interaction model of syringomyelia. *Journal of Fluid Mechanics*, 809:360–389, 2016.

J. D. Heiss, N. Patronas, H. L. DeVroom, T. Shawker, R. Ennis, W. Kammerer, A. Eidsath, T. Talbot, J. Morris, E. Eskioglu, and E. H. Oldfield. Elucidating the pathophysiology of syringomyelia. *Journal of Neurosurgery*, 91:553–562, 1999.

J. D. Heiss, K. Snyder, M. M. Peterson, N. J. Patronas, J. A. Butman, R. K. Smith, H. L. DeVroom, C. A. Sansur, E. Eskioglu, W. A. Kammerer, and E. H. Oldfield. Pathophysiology of primary spinal syringomyelia. *Journal of Neurosurgery: Spine*, 17(5):367–380, 2012.

S. J. Hemley, L. E. Bilston, S. Cheng, and M. A. Stoodley. Aquaporin-4 expression and bloodspinal cord barrier permeability in canalicular syringomyelia. *Journal of Neurosurgery: Spine*, 17(6):602–612, 2012.

S. J. Hemley, L. E. Bilston, S. Cheng, J. N. Chan, and M. A. Stoodley. Aquaporin-4 expression in post-traumatic syringomyelia. *Journal of Neurotrauma*, 30(16): 1457–1467, 2013.

S. B. Hladky and M. A. Barrand. Mechanisms of fluid movement into, through and out of the brain: evaluation of the evidence. *Fluids and Barriers of the CNS*, 11(1):26, 2014.

HSL (2013). A collection of Fortran codes for large scale scientific computation. http://www.hsl.rl.ac.uk.

K. Ichihara, T. Taguchi, Y. Shimada, I. Sakuramoto, S. Kawano, and S. Kawai. Gray matter of the bovine cervical spinal cord is mechanically more rigid and fragile than the white matter. *Journal of Neurotrauma*, 18(3):361–367, 2001.

Y. Itoh, N. Kuwahara, T. Sasajima, K. Mizoi, and J. Hatazawa. Spinal cord edema preceding syringomyelia associated with Chiari I malformation. *Neurologia Medico-Chirurgica*, 42(9):410–413, 2002.

O. Ivanchenko, N. Sindhwani, and A. Linninger. Experimental techniques for studying poroelasticity in brain phantom gels under high flow microinfusion. *Journal of Biomechanical Engineering*, 132(5), 2010.

J. C. Jaeger, N. G. W. Cook, and R. W. Zimmerman. *Fundamentals of Rock Mechanics*. Blackwell Publishing, Oxford, 4th edition, 2007.

S. Javid, A. Rezaei, and G. Karami. A micromechanical procedure for viscoelastic characterization of the axons and ECM of the brainstem. *Journal of the Mechanical Behavior of Biomedical Materials*, 30:290–299, 2014.

J. R. Jinkins, S. Reddy, C. C. Leite, C. Bazan, and L. Xiong. MR of parenchymal spinal cord signal change as a sign of active advancement in clinically progressive posttraumatic syringomyelia. *American Journal of Neuroradiology*, 19(1): 177–182, 1998.

C. L. Johnson, M. D. J. McGarry, A. A. Gharibans, J. B. Weaver, K. D. Paulsen, H. Wang, W. C. Olivero, B. P. Sutton, and J. G. Georgiadis. Local mechanical properties of white matter structures in the human brain. *NeuroImage*, 79: 145–152, 2013.

D. Jones. Optimal Approaches to Diffusion MRI Acquisition. In D. Jones, editor, *Diffusion MRI: Theory, Methods, and Applications*, chapter 15, pages 250–271. Oxford University Press, New York, 2011.

A. Josephson, D. Greitz, T. Klason, L. Olson, and C. Spenger. A spinal thecal sac constriction model supports the theory that induced pressure gradeints in the cord cause edema and cyst formation. *Neurosurgery*, 48(3):636–646, 2001.

M. Kaczmarek, R. P. Subramaniam, and S. R. Neff. The hydromechanics of hydrocephalus: Steady-state solution for cylindrical geometry. *Bulletin of Mathematical Biology*, 59(2):295–323, 1997.

E. N. Kahn, K. M. Muraszko, and C. O. Maher. Prevalence of Chiari I malformation and syringomyelia. *Neurosurgery Clinics of North America*, 26(4):501 – 507, 2015.

Y. Karam, P. W. Hitchon, N. E. Mhanna, W. He, and J. Noeller. Post-traumatic syringomyelia: Outcome predictors. *Clinical Neurology and Neurosurgery*, 124: 44–50, 2014.

J. A. Kessler, J. D. Fenstermacher, and E. S. Owens. Spinal subarachnoid perfusion of rhesus monkeys. *The American Journal of Physiology*, 230(3):614–618, 1976.

J. Klekamp. The pathophysiology of syringomyelia - Historical overview and current concept. *Acta Neurochirurgica*, 144(7):649–664, 2002.

J. Klekamp. Hindbrain-Related Syringomyelia. In G. Flint and C. Rusbridge, editors, *Syringomyelia: A Disorder of CSF Circulation*, chapter 10, pages 141–166. Springer, 2014.

J. Klekamp, U. Batzdorf, M. Samii, and H. W. Bothe. Treatment of syringomyelia associated with arachnoid scarring caused by arachnoiditis or trauma. *Journal of Neurosurgery*, 86(2):233–240, 1997.

J. Klekamp, K. Völkel, C. J. Bartels, and M. Samii. Disturbances of cerebrospinal fluid flow attributable to arachnoid scarring cause interstitial edema of the cat spinal cord. *Neurosurgery*, 48(1):174–186, 2001.

H.-Y. Ko, J. H. Park, Y. B. Shin, and S. Y. Baek. Gross quantitative measurements of spinal cord segments in human. *Spinal Cord*, 42(1):35–40, 2004.

M. A. Koch and J. Finsterbusch. Compartment size estimation with double wave vector diffusion-weighted imaging. *Magnetic Resonance in Medicine*, 60(1): 90–101, 2008.

M. E. Komlosh, E. Özarslan, M. J. Lizak, I. Horkayne-Szakaly, R. Z. Freidlin, F. Horkay, and P. J. Basser. Mapping average axon diameters in porcine spinal cord white matter and rat corpus callosum using d-PFG MRI. *NeuroImage*, 78:210–216, 2013.

R. K. Korhonen, M. S. Laasanen, J. Töyräs, R. Lappalainen, H. J. Helminen, and J. S. Jurvelin. Fibril reinforced poroelastic model predicts specifically mechanical behavior of normal, proteoglycan depleted and collagen degraded articular cartilage. *Journal of Biomechanics*, 36(9):1373–1379, 2003.

D. E. Koser, E. Moeendarbary, J. Hanne, S. Kuerten, and K. Franze. CNS cell distribution and axon orientation determine local spinal cord mechanical properties. *Biophysical Journal*, 108(9):2137–2147, 2015.

I. Koyanagi and K. Houkin. Pathogenesis of syringomyelia associated with Chiari type 1 malformation: Review of evidences and proposal of a new hypothesis. *Neurosurgical Review*, 33(3):271–275, 2010.

I. Koyanagi, Y. Iwasaki, T. Isu, M. Akino, and H. Abe. Significance of spinal cord swelling in the prognosis of acute cervical spinal cord injury. *Paraplegia*, 27(3):190–197, 1989.

R. R. Kumari, J. S. Dhaliwal, M. A. Stoodley, and N. R. Jones. Perivascular CSF flow in the rat cerebellum. *Journal of Clinical Neuroscience*, 6(2):143–146, 1998.

Y. W. Kwon and H. Bang. *The Finite Element Method using MATLAB*. CRC Press, 2nd edition, 2000.

D. Le Bihan. Magnetic Resonance Diffusion Imaging: Introduction and Concepts. In D. K. Jones, editor, *Diffusion MRI: Theory, Methods, and Applications*, chapter 5, pages 57–78. Oxford University Press, New York, 2011.

S. Le Pense and Y. Chen. Contribution of fluid in bone extravascular matrix to strain-rate dependent stiffening of bone tissue - A poroelastic study. *Journal of the Mechanical Behavior of Biomedical Materials*, 65:90–101, 2017.

S. J. Lee, M. A. King, J. Sun, H. K. Xie, G. Subhash, and M. Sarntinoranont. Measurement of viscoelastic properties in multiple anatomical regions of acute rat brain tissue slices. *Journal of the Mechanical Behavior of Biomedical Materials*, 29:213–224, 2014.

D. N. Levine. The pathogenesis of syringomyelia associated with lesions at the foramen magnum: A critical review of existing theories and proposal of a new hypothesis. *Journal of the Neurological Sciences*, 220(1-2):3–21, 2004.

E. I. Levy, J. D. Heiss, M. S. Kent, C. J. Riedel, and E. H. Oldfield. Spinal cord swelling preceding syrinx development. *Journal of Neurosurgery*, 92(1):93–97, 2000.

S. O. Linge, K. A. Mardal, V. Haughton, and A. Helgeland. Simulating CSF flow dynamics in the normal and the Chiari I subarachnoid space during rest and exertion. *American Journal of Neuroradiology*, 34(1):41–45, 2013.

A. A. Linninger, M. Xenos, B. Sweetman, S. Ponkshe, X. Guo, and R. Penn. A mathematical model of blood, cerebrospinal fluid and brain dynamics. *Journal of Mathematical Biology*, 59(6):729–759, 2009.

R. A. Lloyd, D. F. Fletcher, E. C. Clarke, and L. E. Bilston. Chiari malformation may increase perivascular cerebrospinal fluid flow into the spinal cord: A subject-specific computational modelling study. *Journal of Biomechanics*, 65: 185–193, 2017.

F. Loth. Pressure gradient estimation in the spinal canal based on in vivo MR measurements. In *Cerebrospinal Fluid Dynamics Symposium*, Atlanta, Georgia, 2017. URL `https://csfdynamics.org/atlanta2017/scientific-program/`.

Y.-B. Lu, K. Franze, G. Seifert, C. Steinhäuser, F. Kirchhoff, H. Wolburg, J. Guck, P. Janmey, E.-Q. Wei, J. Käs, and A. Reichenbach. Viscoelastic properties of individual glial cells and neurons in the CNS. *Proceedings of* *the National Academy of Sciences of the United States of America*, 103(47): 17759–17764, 2006.

B. A. Martin and F. Loth. The influence of coughing on cerebrospinal fluid pressure in an in vitro syringomyelia model with spinal subarachnoid space stenosis. *Cerebrospinal Fluid Research*, 6(17), 2009.

B. A. Martin, R. Labuda, T. J. Royston, J. N. Oshinski, B. Iskandar, and F. Loth. Spinal subarachnoid space pressure measurements in an in vitro spinal stenosis model: Implications on syringomyelia theories. *Journal of Biomechanical Engineering-Transactions of the ASME*, 132(11), 2010.

A. Massire, M. Taso, P. Besson, M. Guye, J. P. Ranjeva, and V. Callot. High-resolution multi-parametric quantitative magnetic resonance imaging of the human cervical spinal cord at 7T. *NeuroImage*, 143:58–69, 2016.

E. L. Mazuchowski and L. E. Thibault. Biomechanical properties of the spinal cord and pia mater. In *Summer Bioengineering Conference*, Key Biscayne, Florida, 2003. ASME.

C. T. McKee, J. A. Last, P. Russell, and C. J. Murphy. Indentation versus tensile measurements of Young's modulus for soft biological tissues. *Tissue Engineering. Part B, Reviews*, 17(3):155–164, 2011.

A. Mehrabian and Y. Abousleiman. General solutions to poroviscoelastic model of hydrocephalic human brain tissue. *Journal of Theoretical Biology*, 291:105–118, 2011.

G. Melissano, L. Bertoglio, E. Rinaldi, M. Leopardi, and R. Chiesa. An anatomical review of spinal cord blood supply. *The Journal of Cardiovascular Surgery*, 56(5):699–706, 2015.

H. Metz, J. McElhaney, and A. Ommaya. A comparison of the elasticity of live, dead, and fixed brain tissue. *Journal of Biomechanics*, 3(4):453–458, 1970.

T. H. Milhorat, R. M. Kotzen, and A. P. Anzil. Stenosis of central canal of spinal cord in man: Incidence and pathological findings in 232 autopsy cases. *Journal of Neurosurgery*, 80(4):716–722, 1994.

K. Miller. Biomechanics of soft tissues. *Medical Science Monitor*, 6(1):158–167, 2000.

K. Miller, K. Chinzei, G. Orssengo, and P. Bednarz. Mechanical properties of brain tissue in-vivo: Experiment and computer simulation. *Journal of Biomechanics*, 33(11):1369–1376, 2000.

E. Moeendarbary, L. Valon, M. Fritzsche, A. R. Harris, D. A. Moulding, A. J. Thrasher, E. Stride, L. Mahadevan, and G. T. Charras. The cytoplasm of living cells behaves as a poroelastic material. *Nature Materials*, 12(3):253–261, 2013.

B. Mokri. The Monro-Kellie hypothesis: Applications in CSF volume depletion. *Neurology*, 56(12):1746–1748, 2001.

P. F. Morrison, D. W. Laske, H. Bobo, E. H. Oldfield, and R. L. Dedrick. High-flow microinfusion: Tissue penetration and pharmacodynamics. *American Physiological Society*, 266(1):R292–R305, 1994.

A. Nabovati, E. W. Llewellin, and A. C. M. Sousa. A general model for the permeability of fibrous porous media based on fluid flow simulations using the lattice Boltzmann method. *Composites: Part A*, 40(6):860–869, 2009.

T. Nagashima, B. Horwitz, and S. Rapoport. A mathematical model for vasogenic brain edema. *Advances in Neurology*, 52:317–326, 1990.

N. Nair, P. Kalsi, and M. Papadopoulos. Cervical cord presyrinx. *British Journal of Neurosurgery*, 20(3):175–176, 2006.

H. Naruse, K. Tanaka, and A. Kim. A microstructural study of spinal cord edema. In A. D. et al. Mendelow, editor, *Acta Neurochirurgica Supplements*, pages 101–104, Vienna, 2000. Springer.

O. Nesic, J. Lee, Z. Ye, G. C. Unabia, D. Rafati, C. E. Hulsebosch, and J. R. Perez-Polo. Acute and chronic changes in aquaporin 4 expression after spinal cord injury. *Neuroscience*, 143:779–792, 2006.

C. Nicholson. Diffusion and related transport mechanisms in brain tissue. *Reports on Progress in Physics*, 64(7):815–884, 2001.

C. Nicholson and E. Syková. Extracellular space structure revealed by diffusion analysis. *Trends in Neurosciences*, 21(5):207–215, 1998.

S. Nicolle and J.-F. Palierne. Dehydration effect on the mechanical behaviour of biological soft tissues: observations on kidney tissues. *Journal of the Mechanical Behavior of Biomedical Materials*, 3(8):630–635, 2010.

N. Nishida, T. Kanchiku, Y. Kato, Y. Imajo, S. Kawano, and T. Taguchi. Biomechanical analysis of the spinal cord in Brown-Séquard syndrome. *Experimental and Therapeutic Medicine*, 6:1184–1188, 2013.

D. S. Novikov, J. H. Jensen, J. A. Helpern, and E. Fieremans. Revealing mesoscopic structural universality with diffusion. *Proceedings of the National Academy of Sciences*, 111(14):5088–5093, 2014.

B. Nurboja and D. Choi. Extensive spinal cord oedema and early syrinx formation due to tension pseudomeningocele after foramen magnum decompression. *British Journal of Neurosurgery*, 23(4):443–445, 2009.

K. Oshio, D. K. Binder, B. Yang, S. Schecter, A. S. Verkman, and G. T. Manley. Expression of aquaporin water channels in mouse spinal cord. *Neuroscience*, 127(3):685–693, 2004.

H. Ouyang, E. Nauman, and R. Shi. Contribution of cytoskeletal elements to the axonal mechanical properties. *Journal of Biological Engineering*, 7(1):21, 2013.

H. Ozawa, T. Matsumoto, T. Ohashi, M. Sato, and S. Kokubun. Mechanical properties and function of the spinal pia mater. *Journal of Neurosurgery: Spine*, 1(1):122–127, 2004.

P. A. Ozisik, B. H. Hazer, I. M. Ziyal, and O. E. Ozcan. Spontaneous resolution of syringomyelia without Chiari malformation. *Neurologia Medico-Chirurgica*, 46(10):512–517, 2006.

S. H. Pahlavian, T. Yiallourou, R. S. Tubbs, A. C. Bunck, F. Loth, M. Goodin, M. Raisee, and B. A. Martin. The impact of spinal cord nerve roots and denticulate ligaments on cerebrospinal fluid dynamics in the cervical spine. *PloS One*, 9(4), 2014.

S. H. Pahlavian, F. Loth, M. Luciano, J. Oshinski, and B. A. Martin. Neural tissue motion impacts cerebrospinal fluid dynamic at the cervical medullary junction: A patient-specific moving-boundary computational model. *Annals of Biomedical Engineering*, 43(12):2911–23, 2015.

A. J. Pattison, S. S. Lollis, P. R. Perriñez, I. M. Perreard, M. D. J. McGarry, J. B. Weaver, and K. D. Paulsen. Time-harmonic magnetic resonance elastography of the normal feline brain. *Journal of Biomechanics*, 43(14):2747–2752, 2010.

C. Persson, J. Summers, and R. M. Hall. The effect of cerebrospinal fluid thickness on traumatic spinal cord deformation. *Journal of Applied Biomechanics*, 27(4): 330–335, 2011.

M. C. Petit-Lacour, P. Lasjaunias, C. Iffenecker, M. Hadj Rabia, M. Hurth, and D. Doyon. Visibility of the central canal on MRI. *Neuroradiology*, 42(10): 756–761, 2000.

G. Pinna, F. Alessandrini, A. Alfieri, M. Rossi, and A. Bricolo. Cerebrospinal fluid flow dynamics study in Chiari I malformation: Implications for syrinx formation. *Neurosurgical Focus*, 8(3):1–8, 2000.

R. Raghavan and M. Brady. Predictive models for pressure-driven fluid infusions into brain parenchyma. *Physics in Medicine and Biology*, 56(19):6179–6204, 2011.

B. Rashid, M. Destrade, and M. D. Gilchrist. Mechanical characterization of brain tissue in compression at dynamic strain rates. *Journal of the Mechanical Behavior of Biomedical Materials*, 10:23–38, 2012.

M. A. Reina, O. D. L. Casasola, M. C. Villanueva, A. López, F. Machés, and J. A. De Andrés. Ultrastructural findings in human spinal pia mater in relation to subarachnoid anesthesia. *Anesthesia & Analgesia*, 98(5):1479–1485, 2004.

H.-J. Reulen. Bulk flow and diffusion revisited, and clinical applications. In Z. Czernicki, A. Baethmann, U. Ito, Y. Katayama, T. Kuroiwa, and D. Mendelow, editors, *Brain Edema XIV*, pages 3–13, Warsaw, Poland, 2010. Springer.

H.-J. Reulen, R. Graham, M. Spatz, and I. Klatzo. Role of pressure gradients and bulk flow in dynamics of vasogenic brain edema. *Journal of Neurosurgery*, 46(1):24–35, 1977.

J. S. Ross and K. R. Moore. *Diagnostic Imaging: Spine.* Elsevier, Philadelphia, 3rd edition, 2015.

C. G. Roth. *Fundamentals of Body MRI.* Fundamentals of Radiology. Elsevier, 1st edition, 2012.

G. Rutkowska, V. Haughton, S. Linge, and K.-A. Mardal. Patient-specific 3D simulation of cyclic CSF flow at the craniocervical region. *American Journal of Neuroradiology*, 33(9):1756–1762, 2012.

S. Saadoun and M. C. Papadopoulos. Aquaporin-4 in brain and spinal cord oedema. *Neuroscience*, 168(4):1036–1046, 2010.

S. Saadoun, B. A. Bell, A. S. Verkman, and M. C. Papadopoulos. Greatly improved neurological outcome after spinal cord compression injury in AQP4-deficient mice. *Brain*, 131(4):1087–1098, 2008.

L. Sakka, G. Coll, and J. Chazal. Anatomy and physiology of cerebrospinal fluid. *European Annals of Otorhinolaryngology, Head and Neck diseases*, 128 (6):309–16, 2011.

M. Sarntinoranont, R. K. Banerjee, R. R. Lonser, and P. F. Morrison. A computational model of direct interstitial infusion of macromolecules into the spinal cord. *Annals of Biomedical Engineering*, 31(4):448–461, 2003.

M. Sarntinoranont, X. Chen, J. Zhao, and T. H. Mareci. Computational model of interstitial transport in the spinal cord using diffusion tensor imaging. *Annals of Biomedical Engineering*, 34(8):1304–1321, 2006.

J. M. Schuster, F. Zhang, D. C. Norvell, and J. T. Hermsmeyer. Persistent/recurrent syringomyelia after Chiari decompression - Natural history and management strategies: A systematic review. *Evidence-Based Spine-Care Journal 2013*, 4(2):116–125, 2013.

S. Shah, V. Haughton, and A. Muñoz del Rio. CSF flow through the upper cervical spinal canal in Chiari I malformation. *American Journal of Neuroradiology*, 32 (6):1149–1153, 2011.

K. Shahim, J.-M. Drezet, J.-F. Molinari, R. Sinkus, and S. Momjian. Finite element analysis of normal pressure hydrocephalus: Influence of CSF content and anisotropy in permeability. *Applied Bionics and Biomechanics*, 7(3):187–197, 2010.

S. S. Shetye, K. L. Troyer, F. Streijger, J. H. T. Lee, B. K. Kwon, P. A. Cripton, and C. M. Puttlitz. Nonlinear viscoelastic characterization of the porcine spinal cord. *Acta Biomaterialia*, 10(2):792–797, 2014.

D. I. Shreiber, H. Hao, and R. A. I. Elias. Probing the influence of myelin and glia on the tensile properties of the spinal cord. *Biomechanics and Modeling in Mechanobiology*, 8(4):311–321, 2009.

B. R. Simon. Multiphase poroelastic finite element models for soft tissue structures. *Applied Mechanics Reviews*, 45(6):191–216, 1992.

I. M. Smith and D. V. Griffiths. *Programming the Finite Element Method*. John Wiley & Sons Ltd, Chichester, UK, 4th edition, 2004.

J. H. Smith and J. A. C. Humphrey. Interstitial transport and transvascular fluid exchange during infusion into brain and tumor tissue. *Microvascular Research*, 73(1):58–73, 2007.

I. Sobey and B. Wirth. Effect of non-linear permeability in a spherically symmetric model of hydrocephalus. *Mathematical Medicine and Biology*, 23(4): 339–361, 2006.

C. J. Sparrey and T. M. Keaveny. Compression behavior of porcine spinal cord white matter. *Journal of Biomechanics*, 44(6):1078–1082, 2011.

C. J. Sparrey, G. T. Manley, and T. M. Keaveny. Effects of white, grey, and pia mater properties on tissue level stresses and strains in the compressed spinal cord. *Journal of Neurotrauma*, 26(4):585–595, 2009.

M. C. Speer, D. S. Enterline, L. Mehltretter, P. Hammock, J. Joseph, M. Dickerson, R. G. Ellenbogen, T. H. Milhorat, M. A. Hauser, and T. M. George. Chiari type I malformation with or without syringomyelia: Prevalence and genetics. *Journal of Genetic Counselling*, 12(4):297–311, 2003.

N. Stikov, J. S. W. Campbell, T. Stroh, M. Lavelée, S. Frey, J. Novek, S. Nuara, M.-K. Ho, B. J. Bedell, R. F. Dougherty, I. R. Leppert, M. Boudreau, S. Narayanan, T. Duval, J. Cohen-Adad, P.-A. Picard, A. Gasecka, D. Côté, and G. B. Pike. In vivo histology of the myelin g-ratio with magnetic resonance imaging. *NeuroImage*, 118:397–405, 2015.

I. A. Stokes, S. Chegini, S. J. Ferguson, M. G. Gardner-Morse, J. C. Iatridis, and J. P. Laible. Limitation of finite element analysis of poroelastic behavior of biological tissues undergoing rapid loading. *Annals of Biomedical Engineering*, 38(5):1780–1788, 2010.

M. A. Stoodley, N. R. Jones, and C. J. Brown. Evidence for rapid fluid flow from the subarachnoid space into the spinal cord central canal in the rat. *Brain Research*, 707(2):155–164, 1996.

M. A. Stoodley, N. R. Jones, L. Yang, and C. J. Brown. Mechanisms underlying the formation and enlargement of noncommunicating syringomyelia: experimental studies. *Neurosurgical Focus*, 8(3):1–7, 2000.

K. H. Støverud, K. A. Mardal, V. Haughton, and H. P. Langtangen. CSF flow in Chiari I and syringomyelia from the perspective of computational fluid dynamics. *The Neuroradiology Journal*, 24(1):20–23, 2011.

K. H. Støverud, H. P. Langtangen, V. Haughton, and K.-A. Mardal. CSF pressure and velocity in obstructions of the subarachnoid spaces. *The Neuroradiology Journal*, 26(2):218–226, 2013.

K. H. Støverud, M. Alnæs, H. P. Langtangen, V. Haughton, and K.-A. Mardal. Poro-elastic modeling of syringomyelia - A systematic study of the effects of pia mater, central canal, median fissure, white and gray matter on pressure wave propagation and fluid movement within the cervical spinal cord. *Computer Methods in Biomechanics and Biomedical Engineering*, 19(6):686–698, 2016a.

K. H. Støverud, H. P. Langtangen, G. A. Ringstad, P. K. Eide, and K. A. Mardal. Computational investigation of cerebrospinal fluid dynamics in the posterior cranial fossa and cervical subarachnoid space in patients with Chiari I malformation. *PLoS ONE*, 11(10):1–16, 2016b.

P. W. Stroman, C. Wheeler-Kingshott, M. Bacon, J. M. Schwab, R. Bosma, J. Brooks, D. Cadotte, T. Carlstedt, O. Ciccarelli, J. Cohen-Adad, A. Curt, N. Evangelou, M. G. Fehlings, M. Filippi, B. J. Kelley, S. Kollias, A. Mackay, C. A. Porro, S. Smith, S. M. Strittmatter, P. Summers, and I. Tracey. The current state-of-the-art of spinal cord imaging: Methods. *NeuroImage*, 84: 1070–1081, 2014.

A. F. Struck, C. M. Carr, V. Shah, J. R. Hesselink, and V. M. Haughton. Cervical spinal canal narrowing in idiopathic syringomyelia. *Neuroradiology*, 58(8):771–775, 2016.

E. Syková and C. Nicholson. Diffusion in brain extracellular space. *Physiological Reviews*, 88(4):1277–1340, 2008.

E. Sykova, J. Svoboda, J. Polak, and A. Chvatal. Extracellular volume fraction and diffusion characteristics during progressive ischemia and terminal anoxia in the spinal cord of the rat. *Journal of Cerebral Blood Flow & Metabolism*, 14 (2):301–311, 1994.

Z. Taylor and K. Miller. Reassessment of brain elasticity for analysis of biomechanisms of hydrocephalus. *Journal of Biomechanics*, 37(8):1263–1269, 2004.

S. Thakar, N. A. S. Kiran, and A. S. Hegde. A sacral arachnoid cyst causing holocord syringomyelia. *Journal of Neurosurgery: Pediatrics*, 8(3):299–302, 2011.

A. Thompson. The cervical spinal canal tapers differently in patients with Chiari

I with and without syringomyelia. *American Journal of Neuroradiology*, 37(4): 755–758, 2016.

G. J. Tortora and B. Derrickson. *Principles of Anatomy and Physiology.* Wiley, Hoboken, NJ, 14th edition, 2014.

B. Tully, J. Byrne, and Y. Ventikos. Is normal pressure hydrocephalus more than a mechanical disruption to CSF flow? In *2010 Annual International Conference of the IEEE Engineering in Medicine and Biology Society*, pages 235–238, 2010.

A. R. Tunturi. Elasticity of the spinal cord, pia, and denticulate ligament in the dog. *Journal of Neurosurgery*, 48(6), 1978.

E. Turan and P. Arbenz. Large scale micro finite element analysis of 3D bone poroelasticity. *Parallel Computing*, 40(7):239–250, 2014.

J. C. Vardakis, D. Chou, B. J. Tully, C. C. Hung, T. H. Lee, P. H. Tsui, and Y. Ventikos. Investigating cerebral oedema using poroelasticity. *Medical Engineering and Physics*, 38(1):48–57, 2016.

J. Venton, S. Bouyagoub, P. J. Harris, and G. Phillips. Deriving spinal cord permeability and porosity using diffusion-weighted MRI data. In M. Vandamme, P. Dangla, J.-M. Pereira, and S. Ghabezloo, editors, *Poromechanics VI: Proceedings of the Sixth Biot Conference on Poromechanics*, pages 1451–1457, Paris, France, 2017. American Society of Civil Engineers.

F. Vergani, C. Nicholson, and A. Jenkins. Tethering of the cervico-medullary junction with central cord oedema after foramen magnum decompression for Chiari malformation. *British Journal of Neurosurgery*, 25(3):327–329, 2011.

P. Vermeer and A. Verruijt. An accuracy condition for consolidation by finite elements. *Numerical and Analytical Methods in Geomechanics*, 5(1):1–14, 1981.

H. F. Wang. *Theory of Linear Poroelasticity with Applications to Geomechanics and Hydrogeology*. Princeton University Press, 2000.

P. Wang and W. L. Olbricht. Fluid mechanics in the perivascular space. *Journal of Theoretical Biology*, 274(1):52–57, 2011.

T. Wehner, J. S. Ross, and R. M. Ransohoff. Fluid in the flute: Reversible hydromyelia. *Journal of the Neurological Sciences*, 236(1-2):85–6, 2005.

J. Weickenmeier, R. de Rooij, S. Budday, P. Steinmann, T. C. Ovaert, and E. Kuhl. Brain stiffness increases with myelin content. *Acta Biomaterialia*, 42:265–272, 2016.

R. Weller. Anatomy and Physiology. In G. Flint and C. Rusbridge, editors, *Syringomyelia: A Disorder of CSF Circulation*, chapter 3, pages 25–44. Springer, 2014.

C. A. Wheeler-Kingshott, P. W. Stroman, J. M. Schwab, M. Bacon, R. Bosma, J. Brooks, D. W. Cadotte, T. Carlstedt, O. Ciccarelli, J. Cohen-Adad, A. Curt, N. Evangelou, M. G. Fehlings, M. Filippi, B. J. Kelley, S. Kollias, A. Mackay, C. A. Porro, S. Smith, S. M. Strittmatter, P. Summers, A. J. Thompson, and I. Tracey. The current state-of-the-art of spinal cord imaging: Applications. *NeuroImage*, 84:1082–1093, 2014.

B. Williams. Cerebrospinal fluid pressure changes in response to coughing. *Brain*, 99(2):331–346, 1976.

B. Williams. On the pathogenesis of syringomyelia: A review. *Journal of the Royal Society of Medicine*, 73:798–806, 1980.

B. Wirth and I. Sobey. An axisymmetric and fully 3D poroelastic model for the evolution of hydrocephalus. *Mathematical Medicine and Biology: A Journal of the IMA*, 23(4):363–388, 2006.

B. Wirth and I. Sobey. Analytic solution during an infusion test of the linear unsteady poroelastic equations in a spherically symmetric model of the brain. *Mathematical Medicine and Biology: A Journal of the IMA*, 26(1):25–61, 2009.

J. Wong, S. Hemley, N. Jones, S. Cheng, L. E. Bilston, and M. A. Stoodley. Fluid outflow in a large-animal model of posttraumatic syringomyelia. *Neurosurgery*, 71(2):474–480, 2012.

J. Xu, H. Li, K. D. Harkins, X. Jiang, J. Xie, H. Kang, M. D. Does, and J. C. Gore. Mapping mean axon diameter and axonal volume fraction by MRI using temporal diffusion spectroscopy. *NeuroImage*, 103:10–19, 2014.

H. Yan, X. Han, M. Jin, Z. Liu, D. Xie, S. Sha, Y. Qiu, and Z. Zhu. Morphometric features of posterior cranial fossa are different between Chiari I malformation with and without syringomyelia. *European Spine Journal*, 25(7):2202–2209, 2016.

H. Yoon, N. won Park, Y. M. Ha, J. Kim, W. J. Moon, and K. Eom. Diffusion tensor imaging of white and grey matter within the spinal cord of normal Beagle dogs: Sub-regional differences of the various diffusion parameters. *Veterinary Journal*, 215:110–117, 2016.

E. T. Zhang, C. B. E. Inman, and R. Weller. Interrelationships of the pia mater and the perivascular (Virchow-Robin) spaces in the human cerebrum. *Journal of Anatomy*, 170:111–123, 1990.

H. Zhang, P. L. Hubbard, G. J. M. Parker, and D. C. Alexander. Axon diameter mapping in the presence of orientation dispersion with diffusion MRI. *NeuroImage*, 56(3):1301–1315, 2011.

H. Zhang, T. Schneider, C. A. Wheeler-Kingshott, and D. C. Alexander. NODDI:

Practical in vivo neurite orientation dispersion and density imaging of the human brain. *NeuroImage*, 61(4):1000–1016, 2012.

Z. Zhu, S. Sha, X. Sun, Z. Liu, H. Yan, W. Zhu, Z. Wang, and Y. Qiu. Tapering of the cervical spinal canal in patients with distended or nondistended syringes secondary to Chiari type I malformation. *American Journal of Neuroradiology*, 35(10):2021–2026, 2014.

O. C. Zienkiewicz and R. L. Taylor. *The Finite Element Method Vol. 1.* McGraw-Hill, London, 4th edition, 1989.

Appendices

Appendix A

Finite element program outline

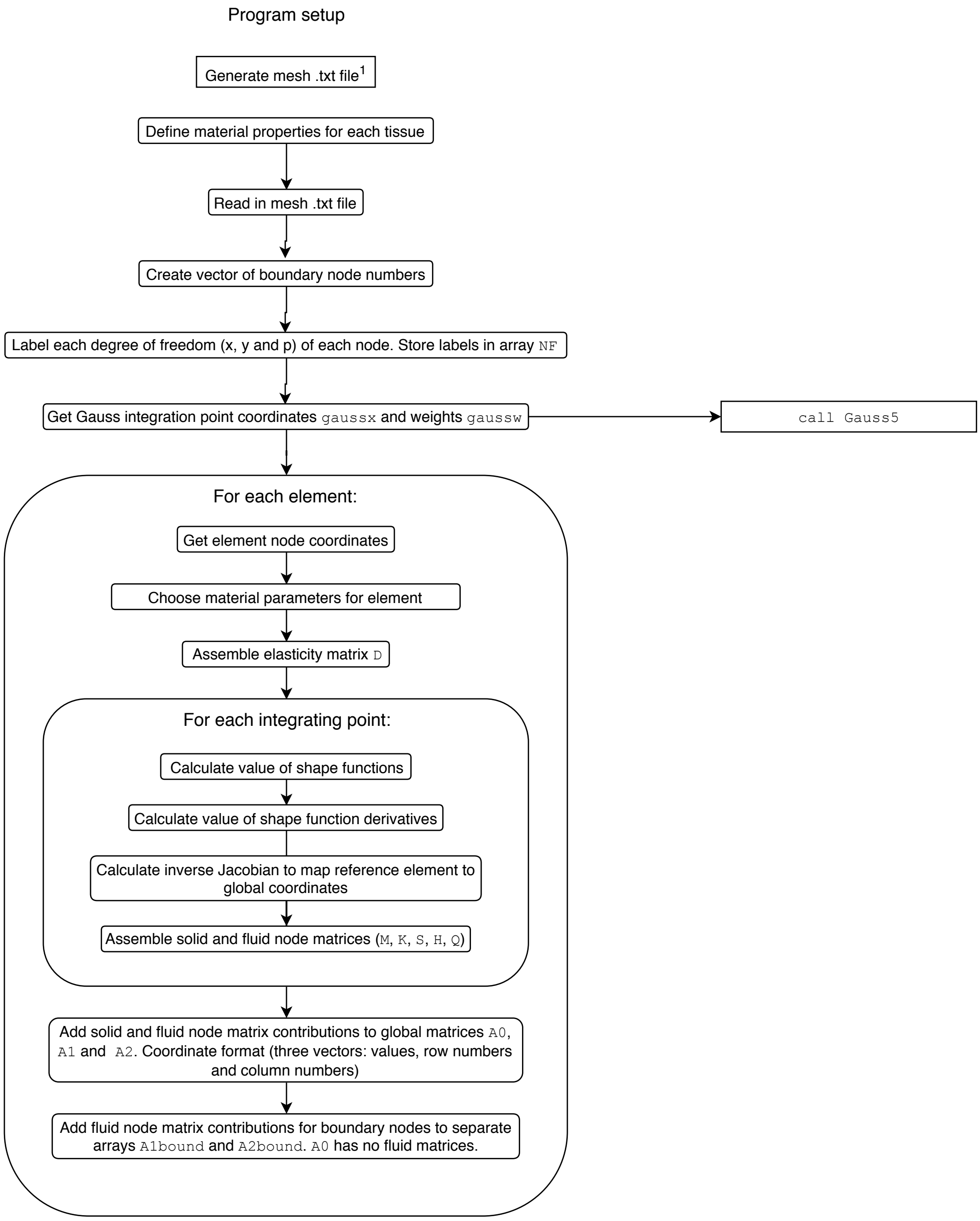

Figure A.1: Flow diagram outlining the main stages of the finite element program, indicating external libraries and software used. [1] Gmsh version 3.0.5 (Geuzaine and Remacle, 2009), [2] Harwell Subroutine Library (HSL (2013)), uses BLAS (Basic Linear Algebra Subprograms).

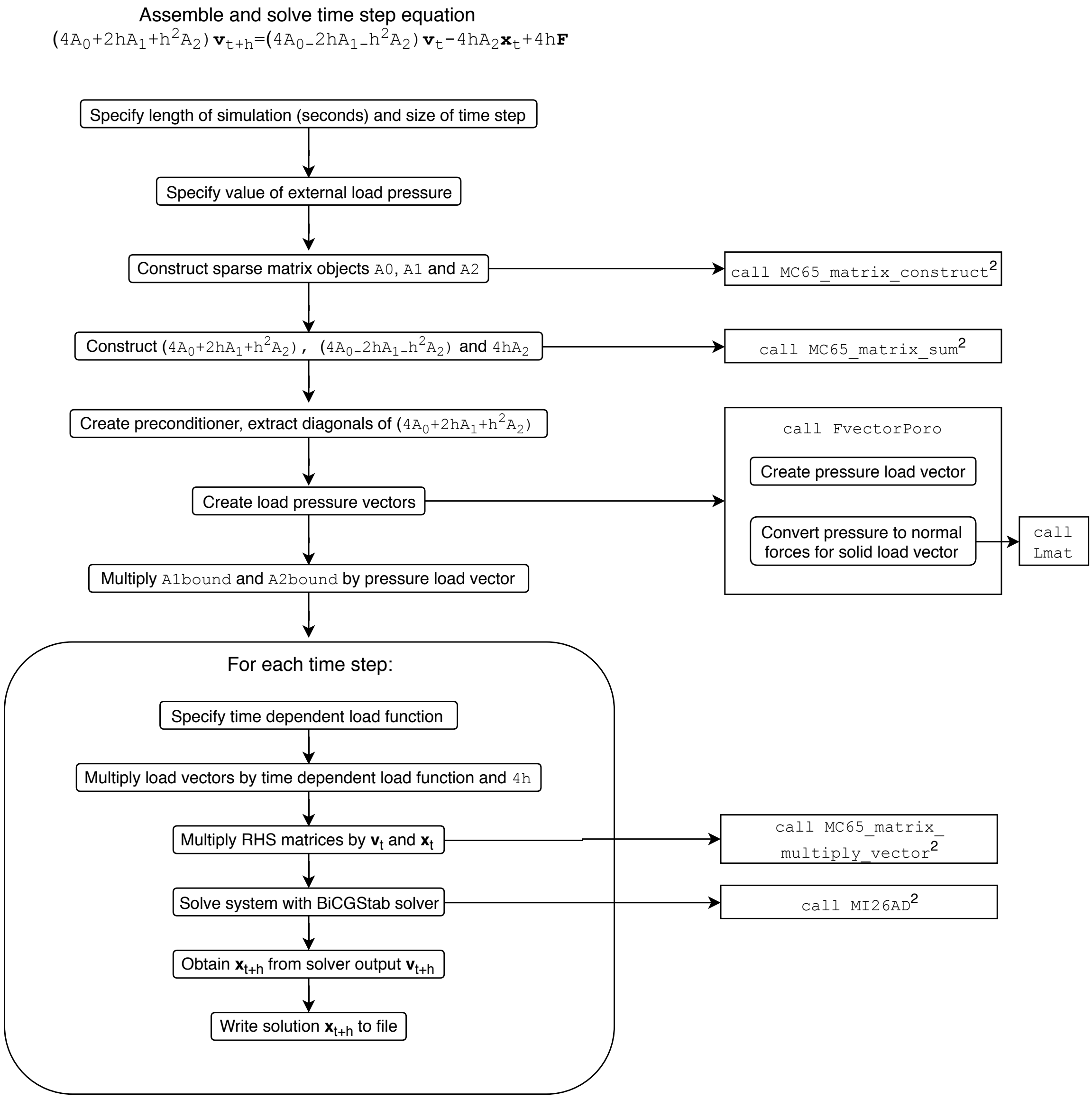

Figure A.1: *(cont.)*

Appendix B

Static analytical solution

This is an uncoupled problem, as the effects of solid displacement on pore pressure are disregarded (there is no Q^T term) but pore fluid is still able to influence solid displacements (via the Q term). The matrix equation for the static problem

$$\begin{pmatrix} K & -Q \\ 0 & H \end{pmatrix} \begin{bmatrix} \boldsymbol{u} \\ \boldsymbol{p} \end{bmatrix} = \begin{bmatrix} \boldsymbol{F}_s \\ \boldsymbol{F}_f \end{bmatrix} \tag{B.1}$$

can be written as

$$A\boldsymbol{x} = \boldsymbol{b} \tag{B.2}$$

and solving this linear equation will give the pore pressure $\boldsymbol{p}$ and solid skeleton displacement $\boldsymbol{u}$ when a predetermined force $\boldsymbol{b}$ is applied.

Results from this static poroelastic model were compared to an analytical solution for validation (Bower, 2010). For simplicity the analytical solution for a poroelastic disc was calculated using two dimensional cylindrical coordinates (r, θ), solving

$$\frac{d\sigma_r}{dr} + \frac{\sigma_r - \sigma_\theta}{r} = 0 \tag{B.3}$$

where stresses are given in terms of strains by

$$\sigma_r = (1-\phi)\frac{E}{(1+\nu)(1-2\nu)}\Big((1-\nu)\varepsilon_r + \nu\varepsilon_\theta\Big) - \phi p$$
$$\sigma_\theta = (1-\phi)\frac{E}{(1+\nu)(1-2\nu)}\Big((1-\nu)\varepsilon_\theta + \nu\varepsilon_r\Big) - \phi p$$

and strains are defined by

$$\varepsilon_r = \frac{d}{dr}u(r), \quad \varepsilon_\theta = \frac{u(r)}{r} \ .$$

As before p represents internal pore pressure, ϕ is the porosity, σ and ε are stresses and strains, E and ν are Young's modulus and Poisson's ratio.

Appendix C

Stress analysis

Details of the post-processing stress analysis is given here. Stress was calculated at the centre of each element (see Figure C.1).

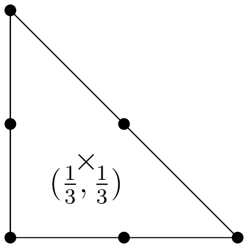

Figure C.1: Stress was evaluated at the centre point (marked ×).

The simulation output nodal displacements $\boldsymbol{u}$ for each element. Stress values

$$\boldsymbol{\sigma} = \begin{pmatrix} \sigma_{xx} & \sigma_{xy} \\ \sigma_{yx} & \sigma_{yy} \end{pmatrix}$$

were recovered, where σ_{xx} and σ_{yy} are normal stresses in the x and y directions respectively and σ_{xy} and σ_{yx} are shear stresses. As the stress tensor is symmetric $\sigma_{xy} = \sigma_{yx}$; hereafter shear stresses will be denoted τ. Stresses were calculated with

$$\boldsymbol{\sigma} = \boldsymbol{DBu} \tag{C.1}$$

where $\boldsymbol{D}$ is the elasticity matrix defined by

$$\boldsymbol{D} = \frac{E(1-\nu)}{(1+\nu)(1-2\nu)} \begin{bmatrix} 1 & \frac{\nu}{1-\nu} & 0 \\ \frac{\nu}{1-\nu} & 1 & 0 \\ 0 & 0 & \frac{1-2\nu}{2(1-\nu)} \end{bmatrix}. \tag{C.2}$$

Here ν and E are the elasticity parameters Poisson's ratio and Young's modulus respectively. The strain-displacement matrix $\boldsymbol{B}$ is given by

$$\boldsymbol{B} = \begin{bmatrix} \frac{\partial N_i}{\partial x} & 0 \\ 0 & \frac{\partial N_i}{\partial y} \\ \frac{\partial N_i}{\partial y} & \frac{\partial N_i}{\partial x} \end{bmatrix}$$

where N_i are the finite element shape functions for a 6-node triangular element.

To allow a meaningful comparison of stresses in the spinal cord the principal stresses were calculated. The minimum and maximum principal stresses were calculated using

$$\sigma_{1,2} = \frac{\sigma_{xx} + \sigma_{yy}}{2} \pm \sqrt{\left(\frac{\sigma_{xx} - \sigma_{yy}}{2}\right)^2 + \tau^2} \tag{C.3}$$

where σ_1 is the maximum principal stress and σ_2 is the minimum principal stress. To generate the stress plots in Chapter 5, the element principal stresses σ_1 and σ_2 were averaged at the element nodes.

List of publications

Published conference papers

J. Venton, S. Bouyagoub, P. J. Harris, G. Phillips. Deriving spinal cord permeability and porosity using diffusion-weighted MRI data. In *Poromechanics VI: Proceedings of the Sixth Biot Conference on Poromechanics*, pages 1451–1457, Paris, France, 2017. American Society of Civil Engineers.

J. Venton, P. J. Harris, G. Phillips. Development of a Poroelastic Model of Spinal Cord Cavities. In *Integral Methods in Science and Engineering, Volume 2: Practical Applications*, pages 275–283, Padua, Italy, 2017. Springer International Publishing.

Conference posters

J. Venton, P. J. Harris, G. Phillips. A poroelastic model of the spinal cord to investigate syringomyelia. Poster session presented at *Sixth Biot Conference on Poromechanics*, 2017 July 9-13, Paris, France.

Talks

J. Venton, P. J. Harris, G. Phillips, C. Hardwidge. The mechanical role of oedema in cavity formation. Presented at *Syringomyelia-Chiari 2018 International Symposium*, July 17-20, Birmingham, UK.

J. Venton, P. J. Harris, G. Phillips. A poroelastic model of spinal cord cavity growth. Presented at *22nd Congress of the European Society of Biomechanics*, 2016 July 10-13, Lyon, France.